Order n° 2008-ISAL-0065 Year 2008

PhD. thesis

Semi-Analytical Modeling of the Transient Thermal-Elastic-Plastic Contact and its Application to Asperity Collision, Wear and Running-in of Surfaces

Presented at
L'institut national des sciences appliquées de Lyon

To obtain
The title of doctor

Doctoral formation: Mécanique, Energétique, Génie civil, Acoustique (MEGA)

Speciality: Mécanique, Génie mécanique, Génie civil

By
Vincent Boucly
(Engineer)
Defended on September 23rd, 2008 on examination Commission

Jury MM.

Rapporteur	H. MAITOURNAM	Professeur associé (LMS Polytechnique)
Rapporteur	C. GAUTHIER	Professeur (Institut Charles Sardon, CNRS)
Rapporteur	T. C. OVAERT	Professor (University of Notre Dame)
	A. CIMETIERE	Professeur (PhyMat CNRS)
	E. ROUHAUD	Maître de conférences (UTT)
	J. A. RUIZ SABARIEGO	Ingénieur (Hispano-Suiza)
	M. BRUNET	Professeur (CNRS) (INSA de Lyon)
	D. NELIAS	Professeur (CNRS) (INSA de Lyon)

Research laboratory: Laboratoire de Mécanique des Contacts et des Solides (LaMCoS) INSA Lyon

SIGLE	ECOLE DOCTORALE	NOM ET COORDONNEES DU RESPONSABLE
CHIMIE	**CHIMIE DE LYON** **http://sakura.cpe.fr/ED206** M. Jean Marc LANCELIN Insa : R. GOURDON	M. Jean Marc LANCELIN Université Claude Bernard Lyon 1 Bât CPE 43 bd du 11 novembre 1918 69622 VILLEURBANNE Cedex Tél : 04.72.43 13 95 Fax : lancelin@hikari.cpe.fr
E.E.A.	**ELECTRONIQUE, ELECTROTECHNIQUE, AUTOMATIQUE** **http://www.insa-lyon.fr/eea** M. Alain NICOLAS Insa : D. BARBIER ede2a@insa-lyon.fr Secrétariat : M. LABOUNE AM. 64.43 – Fax : 64.54	M. Alain NICOLAS Ecole Centrale de Lyon Bâtiment H9 36 avenue Guy de Collongue 69134 ECULLY Tél : 04.72.18 60 97 Fax : 04 78 43 37 17 eea@ec-lyon.fr Secrétariat : M.C. HAVGOUDOUKIAN
E2M2	**EVOLUTION, ECOSYSTEME, MICROBIOLOGIE, MODELISATION** **http://biomserv.univ-lyon1.fr/E2M2** M. Jean-Pierre FLANDROIS Insa : H. CHARLES	M. Jean-Pierre FLANDROIS CNRS UMR 5558 Université Claude Bernard Lyon 1 Bât G. Mendel 43 bd du 11 novembre 1918 69622 VILLEURBANNE Cédex Tél : 04.26 23 59 50 Fax 04 26 23 59 49 06 07 53 89 13 e2m2@biomserv.univ-lyon1.fr
EDIIS	**INFORMATIQUE ET INFORMATION POUR LA SOCIETE** http://ediis.univ-lyon1.fr M. Alain MILLE Secrétariat : I. BUISSON	M. Alain MILLE Université Claude Bernard Lyon 1 LIRIS - EDIIS Bâtiment Nautibus 43 bd du 11 novembre 1918 69622 VILLEURBANNE Cedex Tél : 04.72. 44 82 94 Fax 04 72 44 80 53 ediis@liris.cnrs.fr - alain.mille@liris.cnrs.fr
EDISS	**INTERDISCIPLINAIRE SCIENCES-SANTE** Sec : Safia Boudjema M. Didier REVEL Insa : M. LAGARDE	M. Didier REVEL Hôpital Cardiologique de Lyon Bâtiment Central 28 Avenue Doyen Lépine 69500 BRON Tél : 04.72.68 49 09 Fax :04 72 35 49 16 Didier.revel@creatis.uni-lyon1.fr
Matériaux	**MATERIAUX DE LYON** M. Jean Marc PELLETIER Secrétariat : C. BERNAVON 83.85	M. Jean Marc PELLETIER INSA de Lyon MATEIS Bâtiment Blaise Pascal 7 avenue Jean Capelle 69621 VILLEURBANNE Cédex Tél : 04.72.43 83 18 Fax 04 72 43 85 28 Jean-marc.Pelletier@insa-lyon.fr
Math IF	**MATHEMATIQUES ET INFORMATIQUE FONDAMENTALE** M. Pascal KOIRAN Insa : G. BAYADA	M.Pascal KOIRAN Ecole Normale Supérieure de Lyon 46 allée d'Italie 69364 LYON Cédex 07 Tél : 04.72.72 84 81 Fax : 04 72 72 89 69 Pascal.koiran@ens-lyon.fr Secrétariat : Fatine Latif - latif@math.univ-lyon1.fr
MEGA	**MECANIQUE, ENERGETIQUE, GENIE CIVIL, ACOUSTIQUE** M. Jean Louis GUYADER Secrétariat : M. LABOUNE PM : 71.70 –Fax : 87.12	M. Jean Louis GUYADER INSA de Lyon Laboratoire de Vibrations et Acoustique Bâtiment Antoine de Saint Exupéry 25 bis avenue Jean Capelle 69621 VILLEURBANNE Cedex Tél :04.72.18.71.70 Fax : 04 72 18 87 12 mega@lva.insa-lyon.fr
ScSo	**ScSo*** M. BRAVARD Jean Paul Insa : J.Y. TOUSSAINT	M. BRAVARD Jean Paul Université Lyon 2 86 rue Pasteur 69365 LYON Cedex 07 Tél : 04.78.69.72.76 Fax : 04.37.28.04.48 Jean-paul.bravard@univ-lyon2.fr

*ScSo : Histoire, Geographie, Aménagement, Urbanisme, Archéologie, Science politique, Sociologie, Anthropologie

Remerciements

Je tiens tout d'abord à remercier toute l'équipe du LaMCoS. L'ambiance de travail et les compétences de chacun ont rendu ces années très constructives et agréables.

Mes plus vifs remerciements s'adressent à Habibou Maitournam, Professeur associé au Département de Mécanique du LMS à l'Ecole Polytechnique, Christian Gauthier, Professeur à l'Institut Charles Sadron, CNRS de Saint-Etienne, et Timothy C. Ovaert, Professeur à l'University de Notre Dame, au sein du département « Aerospace and Mechanical Engineering » pour leur lourde tâche de rapporteur, en un temps exceptionnellement court.

Un grand merci à Michel Brunet pour avoir accepté d'être un de mes directeurs de thèse, et ses conseils sur la plasticité, ainsi que Alain Cimetière, et Emmanuelle Rouhaud pour leur participation au jury.

J'ai une infinie reconnaissance en mon superviseur industriel, Christophe Gallais, qui a su être très accessible et compréhensif, et qui a permis mon intégration au sein du service de recherche et développement d'Hispano-Suiza, certes de courte durée, mais enrichissante sur tous les points.

Les mots sont de toute évidence difficiles à trouver pour remercier mon directeur de thèse Daniel Nélias à qui je dois tellement. Je lui dirai simplement merci pour son implication dans ce travail, ses idées pertinentes et originales, son soutien, merci pour les inoubliables moments passés lors des conférences à l'autre bout du monde. Parmi eux, les moments de boulot, les discussions autour d'un verre de vin, les sushis, les blagues un peu lourdes, les voyages en avion accompagnés de rencontres bizarres et de bloody mary, etc. Merci pour sa compréhension dans les moments difficiles et de questionnements.
Merci également à Agniès pour les diners (et son fabuleux tiramisu), les parties de tarot, et les discussions qui nous ont permis de refaire le monde. Et merci à Sam et Alban pour les parties de foot !

Je remercie profondément mes amis et collègues qui ont été formidables avec moi. En particulier, je pense à Benji (tu te souviens quand on était gamin ?), Daniel avec sa trottinette motorisée et ses dvd gravés, Anita (qui me fera peut-être la bise quand je partirai ?), François dans son accoutrement jaune fluo et son humour dans lequel je me retrouve tellement, Emilien le beau gosse de service, Nahiene pour les souvenirs mémorables, et Tarek le sage.

J'aimerais ajouter un remerciement très particulier à Evelyne. J'imagine que sans elle, je n'aurais jamais pu terminer correctement cette thèse. Je la remercie pour ses attentions, merci de m'avoir remonté le moral, d'avoir été si présente, et surtout de m'avoir supporté. En espérant qu'elle restera longtemps si spéciale pour moi.

J'ai une pensée pour mes amis de toujours, Ludo (et son coiffeur), Mat (catapulte), Damien (feyz) et José (t'entends là ? vrouuummm). Leur présence m'a été indispensable.

Enfin j'aimerais dire un grand merci à ma famille pour son soutien de tous les moments. Jul et Amélie pour avoir toujours cru en moi, Mat et No pour m'avoir fait participer à leurs concerts, Jteb pour les nombreuses visites à Lyon, les bringues et les vacances vraiment mémorables.
Mes derniers mots vont vers mes parents, à qui je dois tout, ma réussite, mon bonheur, et mon futur. Ils ne m'ont jamais laissé tomber, ont toujours accepté mes choix quels qu'ils soient, et ont sacrifié une partie de leur vie pour que la mienne soit la meilleure possible. Je leur dédie ce mémoire.

Résumé

Le champ de contraintes au sein des composants de machines est un indicateur important de défaillance due au contact. Comme les contraintes thermiques provoquées par l'échauffement dû au frottement à l'interface ainsi que la plasticité sont significatifs pour les applications réelles, il est critique de prédire le champ de contraintes total. Dans ce travail, une analyse transitoire et tridimensionnelle est réalisée, en prenant en considération le comportement plastique au sein des corps en contact, ainsi que l'échauffement à l'interface. Un algorithme rapide et robuste est proposé pour la résolution du contact vertical, roulant et glissant. Cet algorithme est une alternative à la méthode des Eléments Finis car il donne des résultats précis et robustes en des temps de calcul plus courts, de plusieurs ordres de grandeur. Pour atteindre ce but, des solutions analytiques sont utilisées, appelées coefficients d'influence, et sont utilisées pour le calcul des déplacements, du champ de température, et des tenseurs des déformations et des contraintes. Dans cette formulation, des schémas numériques particuliers sont adoptés afin d'accélérer les temps de calculs. Le problème de contact, qui est une des procédures les plus couteuses, est obtenu en utilisant une méthode basée sur le principe de variation et accéléré au moyen de l'algorithme de convolution discrète et transformée de Fourier rapide ainsi que l'algorithme de gradient conjugué. Aussi, le return-mapping avec prédicteur élastique et correcteur plastique et un critère de von Mises est utilisé pour la boucle plastique. Le modèle est applicable à l'étude du contact roulant et glissant, tant que l'hypothèse des petites perturbations est respectée, et le frottement est reproduit par une loi de Coulomb, comme à l'habitude pour les contacts glissants. La première partie de ce travail décrit l'algorithme utilisé pour formuler le contact vertical, qui peut être traité en imposant soit une charge, soit un déplacement. La manière de traiter le roulement et le glissement de deux corps en contact consiste à résoudre le contact thermo-élasto-plastique à chaque pas de temps en mettant à jour les géométries ainsi que l'écrouissage le long de la direction de roulement. Des simulations sont présentées pour différents cas académiques allant du cas élastique au cas cas thermo-élasto-plastique. Des données expérimentales valident également la théorie et la procédure numérique. Aussi une analyse numérique du contact roulant entre un corps elliptique élastique et un massif élasto-plastique est présentée ainsi que l'influence de différentes lois d'écrouissages. L'application à la collision entre deux aspérités sphériques en glissement simple est développée. La manière de projeter les forces dans le repère global est soulignée, considérant la projection macroscopique due à l'angle entre le plan de contact et la direction de glissement, et la projection microscopique due au bourrelet induit par la déformation permanente des corps en déplacement relatif. Un coefficient de frottement apparent est introduit et les résultats sont présentés en termes d'efforts, de déplacements, et d'énergie dissipée dans le contact. Finalement un modèle pour la prédiction de l'usure et du rodage basé sur l'enlèvement de matière durant un chargement cyclique est proposé. Les résultats sont présentés dans un premier temps pour une surface lisse puis dans un second temps pour une surface rugueuse.

Abstract

The stress field within machine components is an important indicator for contact failures. Since both thermal stresses due to frictional heating and plasticity are significant in engineering application, it is critical to predict the total stress field. In this work, transient and three-dimensional analyses can be realised, taking into consideration plastic behaviour inside the bodies and frictional heating at the interface. A fast and robust algorithm for the resolution of vertical, or rolling and sliding contact is proposed. This algorithm is an alternative to the Finite Element Method, since it gives accurate and robust results in drastically shorter times, by several orders of magnitude. To achieve this, several analytical solutions are utilized, called influence coefficients and they are used for calculation of surface normal displacement, temperature, and strain and stress tensors. In this formulation, particular numerical schemes are adopted to accelerate computing times. The contact problem, which is one of the most time consuming procedures in the elastic-plastic algorithm, is obtained using a method based on the variational principle and accelerated by means of the Discrete Convolution Fast Fourier Transform (DC-FFT) and the single-loop Conjugate Gradient (CG) methods. Also, the return-mapping process with an elastic predictor / plastic corrector scheme and a Von Mises criterion is used for the plasticity loop. The model is applicable for rolling and/or sliding contact problem, as far as small equivalent plastic strain hypothesis is respected,

and a Coulomb's law is assumed for the friction, as commonly used for sliding contacts. The first part of this work describes the algorithm used to deal with the vertical contact, which can be either load-driven (ld) or displacement-driven (dd). The way to consider rolling and sliding motion of the contacting bodies consists of solving the thermal-elastic-plastic contact at each time step while upgrading the geometries as well as the hardening state along the moving directions. Simulations are presented for several academic examples ranging from elastic to thermo-elastic-plastic, and some experiments also validate the theoretical background and the numerical procedure. Also, numerical analysis of the rolling contact between an elastic ellipsoid and an elastic-plastic flat is presented as well as the influence of various hardening laws. An application to the tugging between two spherical asperities in simple sliding (dd-formulation) is made. The way to project the forces in the global reference is outlined, considering the macro-projection due to the angle between the plane of contact and the sliding direction, and the micro-projection due to the pile-up induced by the permanent deformation of the bodies due to their relative motion. An apparent friction coefficient is introduced and results are presented in terms of forces, displacements and energy loss in the contact. Finally a model for wear prediction based on the material removal during cyclic loading is then proposed. Results are presented first for initially smooth surfaces and second for rough surfaces.

Contents

PART 2
SEMI-ANALYTICAL MODELING OF THE VERTICAL THERMAL-ELASTIC-PLASTIC CONTACT 30

PART 3
ROLLING AND SLIDING CONTACT 114

PART 4
DEVELOPMENT OF A MODEL FOR TWO ELASTIC-PLASTIC ASPERITIES TUGGING 146

PART 5

Introduction

Thermomechanical phenomena due to frictional heating and plasticity due to heavy loading significantly influence the failure of components in contacts under relative motions (e.g., thermo-cracking of brakes and face sears, and scuffing in gears). A component is generally subjected to two types of loading, mechanical and thermal, on the surface. The former consists of pressure and shear tractions, and induced plasticity, and the latter is caused by the frictional heating and results in the thermoelastic stress. The knowledge of the thermoelastic and residual stress fields in a component is essential for failure prevention and life prediction because the total stress consists of the thermoelastic stress and the elastic-plastic stress. A fast and robust algorithm for the resolution of vertical, or rolling and sliding contact is proposed. This algorithm is an alternative to the Finite Element Method, since it gives accurate and robust results in drastically shorter times, by several orders of magnitude.

The first part presents a bibliographic background, and is followed by the most important part, which focuses on the main formulation of the vertical contact. The theory is conducted and an algorithm is proposed. The Semi-Analytical formulation is based on the use of analytical solutions which are used for the different calculations by mean of convolution products. Betti's reciprocal theorem is detailed in the case of consideration, and is used to calculate displacements and stress tensors, that are expressed in details. Then, the numerical procedure is explained. The contact problem, which is one of the most time consuming procedures in the thermal-elastic-plastic algorithm, is accelerated by means of the Discrete Convolution Fast Fourier Transform (DC-FFT) and the single-loop Conjugate Gradient (CG) methods. Concerning the plasticity loop the return-mapping process with an elastic predictor / plastic corrector scheme and a Von Mises criterion is explained. The contact problem can be described by applying either a load or a displacement.

The next part is focusing on the way to consider rolling and sliding. Basically the vertical contact is solved at each time step, then geometries and hardening state are updated.

Some experimental and numerical results are proposed in order to validate the formulation.

Afterwards, some applications of the code are developed. The first one is a model for asperity collision. The expression of the interference for each step increment is found, and the way to project the forces in the global reference is outlined, considering the macro-projection due to the angle between the plane of contact and the sliding direction, and the micro-projection due to the pile-up induced by the permanent deformation of the bodies due to their relative motion. An apparent friction coefficient is introduced and results are presented in terms of forces, displacements and energy loss in the contact. Finally a model for wear prediction based on the material removal during cyclic loading is then proposed. Results are presented first for initially smooth surfaces, which commonly yields to a wear volume, whereas for the second example with a rough surface, wear commonly stop after a certain amount of time, and then yields to running-in.

Part 1
Bibliographic Background

This part is an introduction to contact mechanics, and deals with elastic contacts (Hertzian and non-Hertzian contact), thermomechanical issues, plasticity, and rolling contacts.

1.1 Introduction to contact mechanics

The way to carry a load between two deformable bodies is a direct contact between them. Even when a load at the border of the bodies is applied using a fluid, magnetic forces, or gravitational, the force needed to maintain the balance will appear at the interface. The critical point of this direct contact is the stress localization that results, and this often yields to material damage. This is then not astonishing that solid mechanics plays an important role nowadays.
Depending on the curvature of the bodies in contact, one can define conforming or non-conforming contacts. In the case of a non-conforming contact, the contact zone is considered negligible compared to the radii of curvature and the behavior of the contacting bodies is similar to half-spaces. The resolution of the problem consists in finding the real area et the contact pressure distribution.
The origin of all the theory is the famous paper of Heinrich Hertz[Her82], which gave the solution of the elastic contact between two ellipsoidal bodies with flat surfaces, without friction. Even today, this is the basics for industries in the conception of dry, non-conforming, and elastic contacts, as it exists in gears and rolling bearings for instance.
Since 1882, this topic has been extensively developed, and one can observe two main types of studies. Mathematically, some work has been done for extending Hertz analysis to other geometries, for studying other material laws, and for developing existence and solution unity theorems. For engineers, some work has been done on specific cases, on order to better understand phenomena's that occur in real systems.
[Gla80] gives an detailed summary of types of geometries in contacts that had been treated until then, as well as an overview of Russian literature on this topic. [Joh85] gives an excellent global view of the current contact problems, in simplifying formulations for engineers.

1.2 Hertzian contact

Contacting bodies are considered semi-infinite, and non-conforming, at both micro and macro scales, and are loaded on a small part of their surface. These assumptions enabled Hertz to treat separately localized loads in the contact and general distributed stresses inside the bodies. For this simplification to be justified, contact dimensions need to be negligible compared to contacting bodies dimensions. Hertz also assumed that in-depth stresses, under the contact region, are lether than the yield limit, and no friction occurs at the interface. Under these assumptions, Hertz analytically calculated the pressure distribution that satisfies limit conditions at the border of the bodies, as well as inside and outside of the contact area.

In the general case, when two ellipsoids are brought into contact, the deformed surface shape is not known by advance, but Hertz prouved that the contact area is elliptic and that the pressure distribution is semi-elliptic. A particular case of his theory corresponds to the sphere – sphere contact, that yields to a circular contact area. Another particular case is the contact between two cylinders with parallel axis, and considered infinitely long. Such a contact is bi-dimensional, and both the size and the pressure distributions are constant along the axis. This type of contact is called linear contact.

Contact parameters for the three aforementioned cases are recalled hereafter:

1.2.1 Elliptical contact

• Equivalent radius of curvature:

$$R_{eq} = \frac{3}{2} \cdot \left[\frac{1}{R_{x_1}} + \frac{1}{R_{y_1}} + \frac{1}{R_{x_2}} + \frac{1}{R_{y_2}}\right]^{-1} \tag{1.1}$$

• Semi-axis along Ox:

$$a = a^* \cdot \left(\frac{\pi \cdot W \cdot R_{eq}}{E_{eq}}\right)^{\frac{1}{3}} = a^* \cdot \left(\frac{2 \cdot W \cdot R_{eq}}{E'}\right)^{\frac{1}{3}} \tag{1.2}$$

• Semi-axis along Oy:

$$b = b^* \cdot \left(\frac{\pi \cdot W \cdot R_{eq}}{E_{eq}}\right)^{\frac{1}{3}} = b^* \cdot \left(\frac{2 \cdot W \cdot R_{eq}}{E'}\right)^{\frac{1}{3}} \tag{1.3}$$

• Rigid body approach:

$$\delta = \delta^* \left[\left(\frac{W}{E_{eq}}\right)^2 \cdot \frac{\pi^2}{R_{eq}}\right]^{\frac{1}{3}} = \delta^* \left[\frac{4 \cdot W^2}{E'^2 \cdot R_{eq}}\right]^{\frac{1}{3}} \tag{1.4}$$

• Maxi Hertzian pressure:

$$p_0 = \frac{3}{2} \cdot \frac{W}{\pi \cdot a \cdot b} = \frac{3}{2 \cdot \pi \cdot a^* \cdot b^*} \left[\frac{W \cdot E'^2}{4 \cdot {R_{eq}}^2}\right] \tag{1.5}$$

• Pressure distribution:

$$p(x, y) = \frac{3}{2} \cdot \frac{W}{\pi \cdot a \cdot b} \cdot \left[1 - \left(\frac{x}{a}\right)^2 - \left(\frac{y}{b}\right)^2\right] \tag{1.6}$$

1.2.2 Spherical contact

• Equivalent radius of curvature:

$$R_{eq} = \left[\frac{1}{R_1} + \frac{1}{R_2}\right]^{-1} \tag{1.7}$$

• Contact circle radius:

$$a = \left(\frac{3 \cdot \pi \cdot W \cdot R_{eq}}{4 \cdot E_{eq}}\right)^{\frac{1}{3}} = \left(\frac{3 \cdot W \cdot R_{eq}}{2 \cdot E'}\right)^{\frac{1}{3}} \tag{1.8}$$

• Rigid body approach:

$$\delta = \left[\frac{9 \cdot \pi^2 \cdot W^2}{16 \cdot {E_{eq}}^2 \cdot R_{eq}}\right]^{\frac{1}{3}} = \left[\frac{9 \cdot W^2}{4 \cdot E'^2 \cdot R_{eq}}\right]^{\frac{1}{3}} \tag{1.9}$$

• Maxi Hertzian pressure:

$$p_0 = \frac{3}{2} \cdot \frac{W}{\pi \cdot a \cdot b} = \frac{3}{2 \cdot \pi \cdot a^* \cdot b^*} \left[\frac{W \cdot E'^2}{4 \cdot {R_{eq}}^2} \right] \tag{1.10}$$

• Pressure distribution:

$$p(x, y) = \frac{3}{2} \cdot \frac{W}{\pi \cdot a \cdot b} \cdot \left[1 - \left(\frac{x}{a} \right)^2 - \left(\frac{y}{b} \right)^2 \right] \tag{1.11}$$

1.2.3 Linear contact

• Equivalent radius of curvature:

$$R_{eq} = \left[\frac{1}{R_1} + \frac{1}{R_2} \right]^{-1} \tag{1.12}$$

• Semi-axis along Ox:

$$a = \left(\frac{4 \cdot W \cdot R_{eq}}{L \cdot E_{eq}} \right)^{\frac{1}{2}} = \left(\frac{8 \cdot W \cdot R_{eq}}{\pi \cdot L \cdot E'} \right)^{\frac{1}{2}} \tag{1.13}$$

• Maxi Hertzian pressure:

$$p_0 = \left[\frac{W \cdot E'}{2 \cdot \pi \cdot L \cdot R_{eq}} \right]^{\frac{1}{2}} \tag{1.14}$$

• Pressure distribution:

$$p(x, y) = p_0 \cdot \left[1 - \left(\frac{x}{a} \right)^2 \right]^{\frac{1}{2}} \tag{1.15}$$

1.2.4 Stresses

Stresses induced by the contact between two bodies in contact can be expressed analytically in function of the Hertzian pressure and the size of the contact area. For a linear contact the stress tensor components resulting of a normal and tangential loading have been determined by Smith and Liu [Smi53], see Fig.1.1.

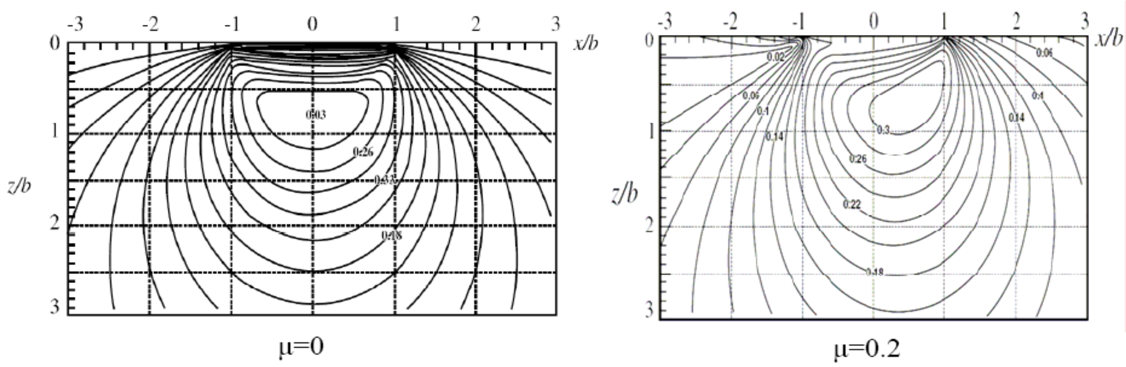

Fig.1.1 Effect of the friction on the surface on Tresca stress distribution normalized by the maximum Hertz pressure, in an elastic body, for a linear contact

For a circular contact, the maximum Tresca stress τ_{max} is 0.31 P_0, P_0 being the Hertzian pressure. It is reached at depth 0,48 a, a being the radius of the contact area. Stresses can be calculated following several different methods, as the ones described by Hills, Nowell, and Sackfield [Hil93]. Fig.1.2 shows isovalues of the maximum shear stress, τ_{max}/P_0, for a circular contact (Fig.1.2a) as well as the value of this tensor components at the center of the contact, along the depth (Fig.1.2b).

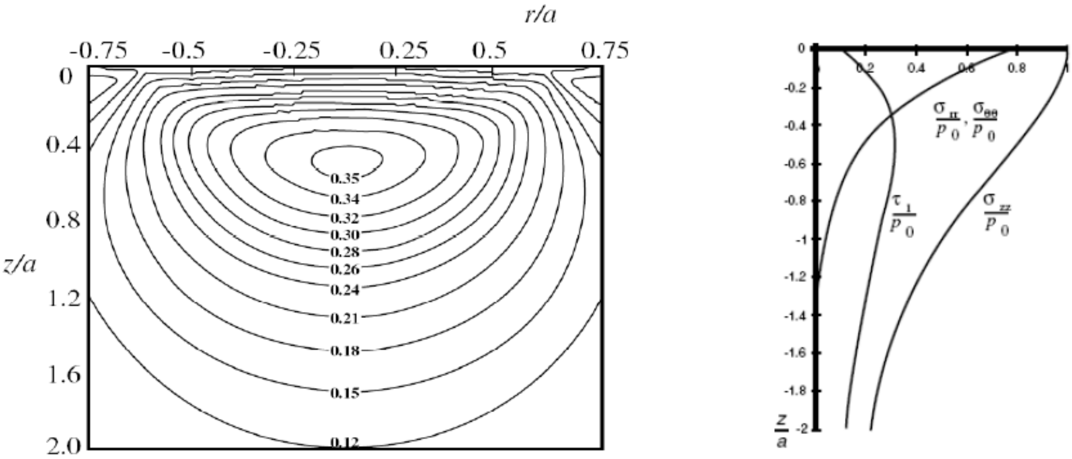

a) Tresca stress for $x = y = 0$.

b) Tensor components along symmetry axis

Fig.1.2 In-depth stresses normalized by the maximum Hertz pressure for a circular contact

When the geometry of the contact yields to an elliptical contact, it is more complicated to find explicit solutions for the internal stress field. Thomas and Hoersh [Tho30] examined the axis of symmetry problem. Later, Fessler and Ollerton [Fes57] determined analytically σ_{zz} and τ_{max}. A more general solution is given by Sackfield and Hills [Sac83b,Sac83a]. Fig.1.3 shows the depth where the maximum shear stress is found on the axis $x = y = 0$ in function of the eccentricity k (ratio between the two semi-axes of the contact ellipse).

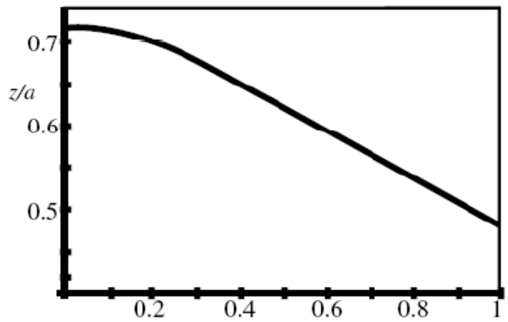

Fig.1.3 Contact ellipticity effect on the location in depth of the maximum shear stress

Progresses during the last century enabled to extend, analytically or numerically Hertz theory for the non-Hertzian cases (real surfaces, inelastic bodies, layered bodies, tangential loading, etc.), see for example the revue done by Johnson [Joh85].

1.3 Non-Hertzian contact

Lots of contact problems don't fit the assumptions listed in the previous section (Hertzian contact), i.e. a normal and frictionless contact between two semi-infinite bodies whose contacting surfaces are supposed to be paraboloids. Numerical methods are then usually required to solve these types of problems. These are problems where there is friction, frictional heating, complex geometries, non-linear material properties as plasticity, or when there is a lubricant (elasto-hydrodynamic theory). A nice revue of that type of problems is given by Barber and Ciavarella [Bar00], Nitta and Kato [Nit00], Adams and Nosonovsky [Ada00] and in Bushan's book [Bhu01].

1.4 Thermal analyses

Frictional heating of rough surfaces is inevitable in tribological contacts and is often responsible for failures such as scuffing, seizure, and cracking [Ken85]. The thermal information regarding contacts is necessary for studies of the interfacial activities in a tribological process [Lin73,Ken84,Tin89,Lu94]. Investigating the coupled thermomechanical behavior of asperities, while considering of thermoelastic distortion, helps explore the effective methods for improving tribological design and preventing failure. Liu et al. [Liu99] reviewed the recent advances in analyzing the contacts between rough surfaces. Due to the complexity of the interaction, rough-surfaces contact and frictional heating are usually treated separately by most researchers, and the related works may be grouped into three categories.

1.4.1 Isothermal contact between rough surfaces.

The majority of the three-dimensional contact simulation models that consider rough surfaces did not take into account frictional heating [Lub91,Pol99,Nog97,Hu99,Pol00a,Pol00b,Liu00b]. However, these models are very useful for determining the load gap or load-area relationship [Pol00a,Pol00b,Liu00b,Lee92]. Some of these models have been successfully applied to solve mixed lubrication problem [Jia99,Shi00,Hu00].

1.4.2 Thermoelastic stress analyses

Mow and Cheng [Mow67] investigated the thermal stresses caused by an arbitrarily distributed moving band heat source, using Fourier transform method and numerical integration. Mercier et al. [Mer78] presented a finite element stress analysis to this same problem. The temperature field, which was the input of the finite element program, was calculated through numerical integration. Tseng and Burton [Tse82] analyzed the thermal stresses in a plane stress problem. For a high-speed (10–15 m/s) moving heat source, Ju and Liu [Ju88] found that the thermal stress was dominant and investigated the influence of the Peclet number on the location of the maximum thermal stress. Kulkarni et al. [Kul91] presented an elasto-plastic finite element analysis with given mechanical and thermal loads. Goshima and Keer [Gos90] considered a halfspace with a surface-breaking crack exposed to a heat source induced by a Hertzian pressure distribution. Most of these analyses were based on two-dimensional models. Huang and Ju [Hua85] investigated the problem of thermomechanical cracking with a three-dimensional thermoelastic model and indicated that the two-dimensional theory might significantly underestimate the stresses, thus justifying the need for threedimensional models. The heat sources in these thermoelastic stress problems were specified beforehand, rather than through an interactive contact analysis.

1.4.3 Flash temperature analysis

Flash temperature has been studied as one of the major topics in tribology since Blok [Blo37] and Jaeger [Jae42]. Recent works on flash temperature aim at systematic analyses of the temperature for different tribological problems. Tian and Kennedy [Tia94] analyzed the surface temperature rise under different specified Peclet numbers and different given heat source shapes. Qiu and Cheng [Qiu98] investigated the temperature rise in a mixed lubricated contact, using a separate isothermal contact model to calculate the pressure distribution necessary for heat source determination. Gao et al. [Gao00] presented a transient flash temperature model for rough surfaces, using the fast Fourier transform (FFT) technique to solve the heat partition problem, while obtaining the pressure distribution separately. The studies of the contact problems between a single asperity and a halfspace can be found in literatures [Tin89,Hua85], most of which assumed a known pressure distribution, e.g., Hertzian pressure. Recently, Wang and Liu [Wan99,Liu00a] developed a two-dimensional thermomechanical model of contact between two infinitely large rough surfaces, while simultaneously considering the thermal phenomena (steady-state heat transfer and the thermoelastic behavior), the mechanical response (elastic-perfectly-plastic behavior), and the interaction (the contact constraints). Both thermal and mechanical variables were determined using interdependent relations. The work reported in [Liu01b] extends the twodimensional thermomechanical model for the contact of infinitely large surfaces to a three-dimensional thermomechanical model for non-conforming contacts.

1.5 Modeling plasticity

In the latest years, substantial progresses in the modeling of contact problems have been made, resulting in more realistic simulations to account for surface roughness and material hardening. The contact between rough surfaces was widely studied. Nevertheless, some restrictive assumptions are often made. Most analyses are purely elastic, even when the stress level is such that the yield stress is locally exceeded. A few papers deal with elastic-plastic contact analyses [Kog02,Jac05,Liu01b,Gal05,Kog03] but most of them, apart those based on FEM analysis [Kog02,Jac05,Kog03], use an elastic-perfectly plastic behavior that in fact corresponds to the implementation of a contact pressure threshold in the contact algorithm [Liu01b,Gal05]. Such an approach seems to give satisfactory results for the contact area, pressure distribution, surface separation, and then can be used for example to predict the leak flow of a fluid within the contact (i.e. for seals). However this approach does not give satisfactory results in terms of subsurface stress state since neither hardening nor residual strains and stresses can be reproduced. Therefore such approach should not be normally used for realistic fatigue life prediction.

Plasticity algorithms for the equivalent plastic deformation calculation are numerous. Among them Fotiu and Nemat-Nasser [Fot96] built a universal algorithm for the integration of the elastic-plastic constitutive equations. Isotropic and kinematic hardening, as well as thermal softening may be used in the formulation. This method is unconditionally stable and accurate. The return mapping algorithm with an elastic predictor / plastic corrector scheme that can be implemented in computational code. The formulation for the plasticity algorithm is based on an iterative scheme and divided in five steps.

1.6 Rolling contact

The rolling contact fatigue phenomenon is involved in many mechanical components such as rolling element bearings, gears, cams, or continuously variable transmissions. The fatigue life of the contacting surfaces is directly related to the stress state found at the surface and within the material in the vicinity of the contact. There exists a certain stress threshold below which the life of the contact is infinite, sometimes called the endurance limit. Lamagnère et al. [Lam98] has proposed an endurance limit concept based on the comparison between the maximum shear stress and the micro-yield stress. This implies an accurate knowledge of the stress field history and of the yield stress of the material. In some high demanding applications rolling element bearings or gears are designed so that the applied load stays below the endurance limit. A purely elastic approach is then sufficient. However it is almost impossible to guaranty that the yield stress will never be reached locally or accidentally all over the life of the component. The knowledge of the plastic strains and hardening state of the material is then of prime importance to evaluate the remaining life of the contacting surfaces. An attempt is made here to account for the contribution of the tangential loading on the stress and strain states found in an elastic-plastic sliding contact, in addition to purely normal effects.

An analytical relationship between the surface profile and contact pressure exists only for a limited number of ideal geometries (Hertz's theory). The hertzian pressure distribution is strongly modified by the presence of a geometrical defect such as a roughness, ridge, furrow, or a dent such as those produced by a debris when entrapped within the contact conjunction. High local pressure peaks appear around the dent producing high concentration of stress localized in the vicinity of the dent. Usually the yield stress is exceeded and plastic flow occurs, and should be added to the initial plasticity introduced during indentation [Nel05,Vin06].

Recently, Jacq et al. [Jac02] has proposed a semi-analytical elastic-plastic method to solve 3D contact problems, fast enough to study a vertical loading / unloading or a moving load for example to simulate the rolling of a body on a surface defect. In this model the contact pressure distribution is found modified from the purely elastic case mostly by plasticity induced change of the contacting surface conformity, which tends to limit the contact pressure to 2.8 or 3 times the yield stress, approximately, depending on the hardening law used and the contact geometry. Both subsurface strains

and stresses are also found strongly modified but this time due to a combination of 3 effects: (i) the occurrence of plastic strains, (ii) the material hardening, and (iii) the change of the contact pressure distribution. Based on the original algorithm the work of Jacq and co-workers has been improved in two ways. First by considering also thermal effect in the elastic-plastic algorithm [Bou05] to account for a surface heat source. Second by introducing the return-mapping algorithm with an elastic predictor and a plastic corrector scheme in the plasticity loop [Nel06]. Based on the same algorithm Wang and Keer [Wan05] have studied the effect of various hardening laws on the elastic-plastic response of the indented material.
The presence of small size surface defects in a larger contact area requires a fine mesh of the contact area (up to 106 surface grid points). To reduce the computing time significantly, the contact module, originally based on a multi-level technique in [Jac02], was replaced by a module based on a single-loop conjugate gradient method developed by Polonsky and Keer [Pol99]. A discussion on the efficiency of this method initially used to solve elastic rough contact problems is given by Allwood [All05]. This method was improved by the implementation of DC-FFT approaches as presented by Liu et al. [Liu00b] for the calculation of surface displacements and internal stress field.

Part 2
Semi-Analytical Modeling of the Vertical Thermal-Elastic-Plastic Contact

This part presents the vertical thermal-elastic-plastic contact. The formulation is based on the use of Betti's reciprocal theorem, and allows the calculation of displacements and stresses. Each term in the formulation is detailed for the numerical procedure. Then an algorithm is proposed, and numerical accelerating techniques are presented. Finally, some experimental and numerical results are shown in order to illustrate and validate the theory

2.1 Theory and Main Calculations

2.1.1 Hypotheses

The dimensions of the contact area are small with regard to the radii of curvature of the contacting bodies that can be considered as half-spaces. Small strains are assumed, which allows to limit the plastic analysis to the volume where yielding occurs, while superposing residual and thermal strains to the elastic part. Higher residual strains as those resulting from a Rockwell indentation could be calculated using a finite elements (FE) software and then introduced as initial state, as far as the over rolling of the surface does not produce large additional strains. The normal and tangential effects are treated separately and are uncoupled in the contact solver. It means that the tangential displacement of the surface points is not known, the boundary condition related to traction is expressed in terms of shear stress.

2.1.2 Energetic considerations

According to [Joh85] one can solve the problem of two nonconforming bodies in contact B_1 and B_2 using two different methods: the direct or Matrix Inversion method and the variational method. [Kal90] has proposed a variational principle in which the true contact area and contact pressure are those which minimize the total complementary energy (V*), subjected to the constraints that the contact pressure is everywhere positive and there is no interpenetration:

$$V^* = U_E^* + \int_{\Gamma_c} p \cdot (h - \omega) \cdot d\Gamma \tag{2.1}$$

where Γ_c is the surface on which p acts and U_E^* is the internal complementary energy of two stressed bodies, numerically equal for elastic materials with the elastic strain energy U_E, which can be expressed in terms of the surface pressure and the normal displacements of both bodies by:

$$U_E^* = U_E + \frac{1}{2}\int_{\Gamma_c} p \cdot (u_3^{B1} + u_3^{B2}) \cdot d\Gamma \tag{2.2}$$

Finally the problem is reduced to a set of equations (two equalities and two inequalities) that should be solved simultaneously (see next section).

2.1.3 Contact problem

As mentioned in the previous part, a dry contact problem can be described by a set of equations – two equalities and two inequalities – that must be solved simultaneously. These are the following:

• The load balance:

$$W = \int_{\Gamma_c} p(x_1, x_2) \cdot d\Gamma \tag{2.3}$$

where W is the total applied load, $p(x_1, x_2)$ the contact pressure at the point of coordinates (x_1, x_2), and Γ_c the part of the surface on which the contact pressure is not nil.

• The surface separation:

$$h(x_1, x_2) = h_i(x_1, x_2) + \omega + u_3{}^{(B_1+B_2)}(x_1, x_2) \tag{2.4}$$

where $h(x_1, x_2)$ is the total distance between the bodies in contact at the point of coordinates (x_1, x_2), $h_i(x_1, x_2)$ the initial distance between the bodies, ω the rigid body displacement, and $u_3{}^{(B_1+B_2)}(x_1, x_2)$ the surface normal displacement of the two bodies B_1 and B_2. The term $u_3{}^{(B_1+B_2)}(x_1, x_2)$ will be expressed in the next section thanks to the formulation of the Betti's Reciprocal Theorem.

• The contact conditions:

$$h(x_1, x_2) \geq 0 \quad \text{and} \quad p(x_1, x_2) \geq 0 \tag{2.5}$$

$$\text{If} \quad h(x_1, x_2) \geq 0 \quad \text{then} \quad p(x_1, x_2) \geq 0 \tag{2.6}$$

Indeed, $h(x_1, x_2)$ must be positive or nil, because the bodies cannot interpenetrate one another. Moreover, when the surface separation of the bodies is positive, there is no contact, and the contact pressure vanishes.

2.1.4 Betti's reciprocal theorem

By definition, the work done by the virtual force through the displacements produced by the real force is equal to the work done by the real force through the displacements produced by the virtual force, see Eq.(2.7).

$$\int_\Gamma u_i^* \cdot p_i \cdot d\Gamma = \int_\Gamma u_i \cdot p_i^* \cdot d\Gamma \tag{2.7}$$

This is the basis of the use of Betti's reciprocal theorem.
One wants to study an elastic body, of volume Ω and boundary Γ. In the entire development, one may consider two different states as follows:

• the state $(u, \varepsilon, \sigma, f_i, T)$ represents a state within which there are initial strains, ε^0;
• the state $(u^*, \varepsilon^*, \sigma^*, f_i^*)$ is a state of elastic deformation, for the moment undetermined.

Let us calculate the product $\sigma_{ij} \cdot \varepsilon_{ij}^*$:

$$\sigma_{ij} \cdot \varepsilon_{ij}^* = C_{ijkl} \cdot \left(\varepsilon_{kl} - \varepsilon_{kl}^t - \varepsilon_{kl}^0\right) \cdot \varepsilon_{ij}^* \tag{2.8}$$

where $C_{ijkl} = \lambda\delta_{ij}\delta_{kl} + \mu\left(\delta_{ik}\delta_{jl} + \delta_{il}\delta_{jk}\right)$, with δ the Kronecker's delta, λ and μ are Lamé constants (for the case of a homogeneous material), and ε^t the thermal strain tensor.

Due to the symmetries of the tensors:

$$\sigma_{ij} \cdot \varepsilon_{ij}^{*} = \left(\varepsilon_{kl} - \varepsilon_{kl}^{0}\right) \cdot \sigma_{kl}^{*} - C_{ijkl} \cdot \varepsilon_{kl}^{t} \cdot \varepsilon_{ij}^{*} \tag{2.9}$$

The integration of the left part in Eq.(2.9) gives:

$$\int_{\Omega} \sigma_{ij} \cdot \varepsilon_{ij}^{*} \cdot d\Omega = \int_{\Omega} \frac{\sigma_{ij}}{2} \cdot \left(u_{i,j}^{*} + u_{j,i}^{*}\right) \cdot d\Omega = \int_{\Omega} \sigma_{ij} \cdot u_{i,j}^{*} \cdot d\Omega \tag{2.10}$$

$$\int_{\Omega} \sigma_{ij} \cdot \varepsilon_{ij}^{*} \cdot d\Omega = \int_{\Omega} \left(\sigma_{ij} \cdot u_{i}^{*}\right)_{,j} \cdot d\Omega - \int_{\Omega} \sigma_{ij,j} \cdot u_{i}^{*} \cdot d\Omega \tag{2.11}$$

According to the equilibrium conditions, one has: $\sigma_{ij,j} + f_i = 0$, hence:

$$\int_{\Omega} \sigma_{ij} \cdot \varepsilon_{ij}^{*} \cdot d\Omega = \int_{\Omega} \left(\sigma_{ij} \cdot u_{i}^{*}\right)_{,j} \cdot d\Omega + \int_{\Omega} f_i \cdot u_{i}^{*} \cdot d\Omega \tag{2.12}$$

By using the Divergence Theorem of Gauss, one obtains:

$$\int_{\Omega} \sigma_{ij} \cdot \varepsilon_{ij}^{*} \cdot d\Omega = -\int_{\Gamma} \sigma_{ij} \cdot u_{i}^{*} \cdot n_j \cdot d\Gamma + \int_{\Omega} f_i \cdot u_{i}^{*} \cdot d\Omega \tag{2.13}$$

where n_j is the entering normal on the surface.

The integration of the right part in Eq.(2.9) gives:

$$\begin{aligned} &\int_{\Omega} \left[\left(\varepsilon_{kl} - \varepsilon_{kl}^{0}\right) \cdot \sigma_{kl}^{*} - C_{ijkl} \cdot \varepsilon_{kl}^{t} \cdot \varepsilon_{ij}^{*}\right] \cdot d\Omega \\ &= \underbrace{\int_{\Omega} \varepsilon_{kl} \cdot \sigma_{kl}^{*} \cdot d\Omega}_{1} - \underbrace{\int_{\Omega} \varepsilon_{kl}^{0} \cdot \sigma_{kl}^{*} \cdot d\Omega}_{2} - \underbrace{\int_{\Omega} C_{ijkl} \cdot \varepsilon_{kl}^{t} \cdot \varepsilon_{ij}^{*} \cdot d\Omega}_{3} \end{aligned} \tag{2.14}$$

Using once again the Divergence Theorem of Gauss, the first term becomes:

$$\int_{\Omega} \varepsilon_{ij} \cdot \sigma_{ij}^{*} \cdot d\Omega = -\int_{\Gamma} \sigma_{ij}^{*} \cdot u_i \cdot n_j \cdot d\Gamma + \int_{\Omega} f_i^{*} \cdot u_i \cdot d\Omega \tag{2.15}$$

Consider now that the initial strains are plastic strains only, which will be noted ε^p, then $tr(\varepsilon^p) = 0$, due to the incompressibility of the plastic zone.

One can easily show that the second term becomes:

$$-\int_{\Omega} \varepsilon_{ij}^{0} \cdot \sigma_{ij}^{*} \cdot d\Omega = -\int_{\Omega} \varepsilon_{ij}^{p} \cdot \sigma_{ij}^{*} \cdot d\Omega = -2\mu \int_{\Omega} \varepsilon_{ij}^{p} \cdot \varepsilon_{ij}^{*} \cdot d\Omega \qquad (2.16)$$

If one considers that the temperature variations induce elastic deformations, one has:

$$\varepsilon^t = \alpha \cdot T \cdot I \qquad i.e. \qquad \varepsilon_{ij}^t = \alpha \cdot T \cdot \delta_{ij} \qquad (2.17)$$

where I is the identity matrix and α the thermal expansion coefficient.

Then:

$$C_{ijkl} \cdot \varepsilon_{kl}^t = \alpha(3\lambda + 2\mu) \cdot T \cdot \delta_{ij} = m \cdot T \cdot \delta_{ij} \qquad (2.18)$$

With

$$m = \alpha(3\lambda + 2\mu) = \alpha \frac{E}{1 - 2\nu} \qquad (2.19)$$

and E is the Young's modulus.

Consequently the third term becomes:

$$-\int_{\Omega} C_{ijkl} \cdot \varepsilon_{kl}^t \cdot \varepsilon_{ij}^* \cdot d\Omega = -\int_{\Omega} m \cdot T \cdot \varepsilon_{kk}^* \cdot d\Omega \qquad (2.20)$$

Finally, the reciprocal theorem with initial strains and a given temperature field can be written as:

$$-\int_{\Gamma} \sigma_{ij} \cdot u_i^* \cdot n_j \cdot d\Gamma + \int_{\Omega} f_i \cdot u_i^* \cdot d\Omega$$

$$= -\int_{\Gamma} \sigma_{ij}^* \cdot u_i \cdot n_j \cdot d\Gamma + \int_{\Omega} f_i^* \cdot u_i \cdot d\Omega - 2\mu \int_{\Omega} \varepsilon_{ij}^p \cdot \varepsilon_{ij}^* \cdot d\Omega \qquad (2.21)$$

$$-\int_{\Omega} m \cdot T \cdot \varepsilon_{kk}^* \cdot d\Omega$$

Consider now that the body forces for the state $(u, \varepsilon, \sigma, f_i, T)$ are negligible. After having rearranged the remaining terms, Eq.(2.21) above becomes:

$$-\int_{\Gamma} \sigma_{ij}^* \cdot u_i \cdot n_j \cdot d\Gamma + \int_{\Omega} f_i^* \cdot u_i \cdot d\Omega$$

$$= -\int_{\Gamma} \sigma_{ij} \cdot u_i^* \cdot n_j \cdot d\Gamma + 2\mu \int_{\Omega} \varepsilon_{ij}^p \cdot \varepsilon_{ij}^* \cdot d\Omega + \int_{\Omega} m \cdot T \cdot \varepsilon_{kk}^* \cdot d\Omega \qquad (2.22)$$

2.1.4.1 Surface displacement calculation

The reciprocal theorem is now applied to the calculation of the surface displacements. From the expression of the reciprocal theorem Eq.(2.22), let us consider the state $(u^*, \varepsilon^*, \sigma^*, f_i^*)$ as the application of a unit normal force at point A of the contact area. The value of the pressure is thus $p^*(M) = \delta(M - A)$ at a point M of the surface, $\delta(\quad)$ being the Dirac delta function.

By using the relation $\sigma_{ij} \cdot n_j = -p_i$ (boundary condition), and considering that $f_i = 0$ (no body forces), one has:

$$-\int_{\Gamma} \sigma_{ij}^* \cdot u_i \cdot n_j \cdot d\Gamma + \int_{\Omega} f_i^* \cdot u_i \cdot d\Omega = \int_{\Gamma} u_i \cdot p_i^* \cdot d\Gamma = u_3(A) \qquad (2.23)$$

where the subscript 3 indicates a normal displacement (according to x_3).

Equation (2.22) becomes:

$$u_3(A) = \int\limits_{\Gamma_c} u_{3i}^{*}(M,A) \cdot p_i(M) \cdot d\Gamma + 2\mu \int\limits_{\Omega_p} \varepsilon_{ij}^{p}(M) \cdot \varepsilon_{3ij}^{*}(M,A) \cdot d\Omega + \int\limits_{\Omega} m \cdot T(M) \cdot \varepsilon_{3kk}^{*}(M,A) \cdot d\Omega \tag{2.24}$$

where Γ_c is the contact area, and Ω_p the plastic volume (the integrals vanish elsewhere). In the terms with a star (*), the first point (M) indicates the point of calculation (integration point), the second point (A) indicates the point of application of the unit force, the subscript (3) indicates the direction of the unit force, and the subscripts (i) and (j) indicate the components.

Hence:

$$u_3(A) = u^e(A) + u^r(A) + u^t(A) \tag{2.25}$$

The surface normal displacement of each body can then be expressed as a function of contact pressure, plastic strain and temperature field existing in the considered body. Lets now consider only one body in contact with a thermal-elastic-plastic behavior, the other one being purely elastic. The formulation could be extended to the case of two (thermal)-elastic-plastic bodies without major difficulties. It is noted that the elastic displacement is decomposed in two parts: the displacement due to normal pressure, and the one due to the surface shear stress.

To solve the contact problem, it is necessary to link the total surface displacement with the contact pressure. In Eq.(2.24), the displacement is related to the contact pressure (as in the elastic case), but also to the plastic strains and the temperature field. It is then necessary to express the plastic strains as function of contact pressure and body temperature.

For displacement calculation, the reader is referred to section 2.1.5.

2.1.4.2 Subsurface stress calculation

From the expression of the reciprocal theorem Eq.(2.22), let us particularize the state $(u^*, \varepsilon^*, \sigma^*, f_i^*)$ as the application of a unit force at a point B in the volume. One will note this state $(u^{**}, \varepsilon^{**}, \sigma^{**}, f_k^{**})$ in order to avoid any confusion with the state defined for the calculation of the surface displacements. The value of the body force is thus $f_k^{**}(M) = \delta(M - B)$ at a point M of the volume, in the direction k.

By using the previous condition, with $p_i^{**} = 0$ since there is no pressure on the surface, one obtains:

$$-\int_{\Gamma} \sigma_{ij}^{**} \cdot u_i \cdot n_j \cdot d\Gamma + \int_{\Omega} f_i^{**} \cdot u_i \cdot d\Omega = \int_{\Omega} f_k^{**} \cdot u_k \cdot d\Omega = u_k(B) \tag{2.26}$$

Equation (2.22) then becomes:

$$\begin{aligned} u_k(B) = \int_{\Gamma_c} u_{ki}^{**}(M,A) \cdot p_i(M) \cdot d\Gamma + 2\mu \int_{\Omega_p} \varepsilon_{ij}^{p}(M) \cdot \varepsilon_{kij}^{**}(M,A) \cdot d\Omega \\ + \int_{\Omega} m \cdot T(M) \cdot \varepsilon_{kii}^{**}(M,A) \cdot d\Omega \end{aligned} \tag{2.27}$$

Hence:

$$u_k(B) = u_k^e(B) + u_k^r(B) + u_k^t(B) \tag{2.28}$$

It is noted that the elastic displacement is decomposed in two parts: the displacement due to normal pressure, and the one due to the surface shear stress.
One uses the Hooke's law to find the expression of the stresses:

$$\begin{aligned} \sigma_{ij}(B) &= C_{ijkl} \cdot \left(\varepsilon_{kl}(B) - \varepsilon_{kl}^r(B) - \varepsilon_{kl}^t(B)\right) \\ &= C_{ijkl} \cdot \left(\frac{1}{2}\left(u_{k,l}(B) + u_{l,k}(B)\right) - \varepsilon_{kl}^r(B) - \varepsilon_{kl}^t(B)\right) \end{aligned} \tag{2.29}$$

Then:

$$
\begin{aligned}
\sigma_{ij}(B) = C_{ijkl} \cdot \Bigg[& \left(\frac{1}{2} \left(u^e_{k,l}(B) + u^e_{l,k}(B) \right) \right) \\
& + \left(\frac{1}{2} \left(u^r_{k,l}(B) + u^r_{l,k}(B) \right) - \varepsilon^r_{kl}(B) \right) \\
& + \left(\frac{1}{2} \left(u^t_{k,l}(B) + u^t_{l,k}(B) \right) - \varepsilon^t_{kl}(B) \right) \Bigg]
\end{aligned} \tag{2.30}
$$

Finally the stress tensor components are obtained by summing the contribution of elastic, residual (plastic) and thermally induced stresses, respectively:

$$\sigma_{ij}(B) = \sigma^e_{ij}(B) + \sigma^r_{ij}(B) + \sigma^t_{ij}(B) \tag{2.31}$$

For stress calculation, the reader is referred to section 2.1.6.

2.1.5 Elastic, thermal, residual displacements calculation

2.1.5.1 Surface elastic displacements

The numerical procedure requires one to discretise the domain in N_s elements of elementary surface Γ_{cn}. The term corresponding to the elastic displacement of the surface along the normal direction thus becomes:

$$
\begin{aligned}
u^e_3(A) &= \sum_{n=1}^{N_s} \int_{\Gamma_{\mathrm{cn}}} u^*_{3i}(M,A) \cdot p_i(M) \cdot d\Gamma \\
&= \sum_{n=1}^{N_s} \int_{\Gamma_{\mathrm{cn}}} u^*_{33}(M,A) \cdot p_3(M) \cdot d\Gamma + \sum_{n=1}^{N_s} \int_{\Gamma_{\mathrm{cn}}} u^*_{31}(M,A) \cdot p_1(M) \cdot d\Gamma
\end{aligned} \tag{2.32}
$$

With: $p_3 = p$ (pressure) and $p_1 = s$ (shear). Coordinates of point A are (x_1, x_2) and coordinates of point M are (x'_1, x'_2).

Normal displacements due to normal pressure (first term) and shear (second term) are both considered. Finally, since the pressure and the shear are considered to be constant within an elementary surface element, Eq.(2.32) becomes:

$$u_3^e(A) =$$

$$\sum_{n=1}^{N_s} p(n) \cdot \int_{\Gamma_{\mathrm{cn}}} u_{33}^*(M,A) \cdot d\Gamma(M) + \sum_{n=1}^{N_s} s(n) \cdot \int_{\Gamma_{\mathrm{cn}}} u_{31}^*(M,A) \cdot d\Gamma(M) \\ = \sum_{n=1}^{N_s} p(n) \cdot D^p(n) + \sum_{n=1}^{N_s} s(n) \cdot D^s(n) \tag{2.33}$$

Using the displacements produced by a unit force obtained by Johnson [Joh85]:

$$D^p(n) = \frac{1-\nu^2}{\pi E} \int_{\Gamma_{\mathrm{cn}}} \frac{1}{\sqrt{(x_1 - x_1')^2 + (x_2 - x_2')^2}} \cdot d\Gamma \tag{2.34}$$

and:

$$D^s(n) = \frac{1}{\pi G} \int_{\Gamma_{\mathrm{cn}}} \frac{(x_1 - x_1')}{(x_1 - x_1')^2 + (x_2 - x_2')^2} \cdot d\Gamma \tag{2.35}$$

The functions D^p and D^s are integrated on an elementary rectangle of center $\Re(r_1, r_2)$ and dimensions $2\Delta x_1 \cdot 2\Delta x_2$. One obtains:

$$D^p = \frac{1-\nu^2}{\pi E} [f(r_u^1, r_u^2) + f(r_l^1, r_l^2) - f(r_u^1, r_l^2) - f(r_l^1, r_u^2)] \tag{2.36}$$

and:

$$D^s = \frac{1}{\pi G} [h(r_u^1, r_u^2) + h(r_l^1, r_l^2) - h(r_u^1, r_l^2) - h(r_l^1, r_u^2)] \tag{2.37}$$

where:

$$\begin{aligned} r_{1u} &= r_1 + \Delta x_1 & \qquad r_{2u} &= r_2 + \Delta x_2 \\ r_{1l} &= r_1 - \Delta x_1 & \qquad r_{2l} &= r_2 - \Delta x_2 \end{aligned} \tag{2.38}$$

The functions f and h are defined as follows:

$$f(x,y) = x \cdot ln\left(y + \sqrt{x^2 + y^2}\right) + y \cdot ln\left(x + \sqrt{x^2 + y^2}\right) \tag{2.39}$$

and:

$$h(x,y) = \frac{y}{2} \cdot ln(x^2 + y^2) - y + x \cdot \tan^{-1}\frac{y}{x} \tag{2.40}$$

2.1.5.2 Surface thermal displacements

In a similar manner and due to the previous derivations - see Eq.(2.24) - , one finds:

$$u_3^t(A) = \int_{\Omega} m \cdot T(M) \cdot \varepsilon_{3kk}^*(M,A) \cdot d\Omega \tag{2.41}$$

Again, the numerical procedure requires one to discretise the domain in N_s elements of elementary surface Γ_{cn}.
The following derivations are detailed in the case of a stationary heat source (negligible Peclet number) and for the steady-state regime. The expression of the thermal displacement for more complicated cases will not be developed, but main formulas can be found in Appendix 1.
Using again the displacements produced by a unit force obtained by Johnson [Joh85], one finds from $\varepsilon_{3kk}^* = u_{3\mathrm{k,k}}^* = u_{31,1}^* + u_{32,2}^* + u_{33,3}^*$ that:

$$\varepsilon_{3kk}^* = \frac{(1-2\nu)}{2\pi\mu} \cdot \frac{z^2}{r^3} \tag{2.42}$$

Which leads to the expression of the thermal displacements:

$$u_3^t(x_1,x_2) = \int_0^{+\infty} \int_{-\infty}^{+\infty} \int_{-\infty}^{+\infty} m \cdot T(\xi_1,\xi_2,\xi_3) \cdot \frac{(1-2\nu)}{2\pi\mu} \cdot \frac{\xi_3^2}{\rho^3} \cdot d\xi_1 \cdot d\xi_2 \cdot d\xi_3 \tag{2.43}$$

With:

$$\rho = \sqrt{(x_1 - \xi_1)^2 + (x_2 - \xi_2)^2 + \xi_3^2} \tag{2.44}$$

After rearranging the constants, it yields:

$$u_3^t(x_1, x_2) = \frac{\alpha(1+\nu)}{\pi} \int_0^{+\infty} \int_{-\infty}^{+\infty} \int_{-\infty}^{+\infty} T(\xi_1, \xi_2, \xi_3) \cdot \\ \frac{\xi_3^2}{[(x_1 - \xi_1)^2 + (x_2 - \xi_2)^2 + \xi_3^2]^{3/2}} \cdot d\xi_1 \cdot d\xi_2 \cdot d\xi_3 \tag{2.45}$$

One can rewrite this expression while revealing a convolution product in two dimensions:

$$u_3^t(x_1, x_2) = \frac{\alpha(1+\nu)}{\pi} \int_0^{+\infty} (T ** G^U) \cdot d\xi_3 \tag{2.46}$$

with G^U the Green function expressed as follows:

$$G^U = \frac{z^2}{(x^2 + y^2 + z)^{3/2}} \tag{2.47}$$

In Eq.(2.46), the temperature field should be determined before calculating the integral with respect to ξ_3, and is expressed with a convolution product in two dimensions (for the stationary case):

$$T(\xi_1, \xi_2, \xi_3) = \int_{-\infty}^{+\infty} \int_{-\infty}^{+\infty} \frac{q(x_1', x_2') \cdot dx_1' \cdot dx_2'}{2\pi K \sqrt{(x_1 - x_1')^2 + (x_2 - x_2')^2 + x_3^2}} \tag{2.48}$$

Which can be written as:

$$T(\xi_1, \xi_2, \xi_3) = q ** G^T \tag{2.49}$$

with G^T the following Green function:

$$G^T = \frac{1}{2\pi K \sqrt{x^2 + y^2 + z^2}} \tag{2.50}$$

where $q = Q_f \cdot p$ is the heat flux (W/m^2) applied on the surface, causing the temperature rise within the body. Q_f (m/s) is called the heat factor, and is equal to $Q_f = \beta \cdot \mu_f \cdot V$, β being the heat partition coefficient (equal to 1 if one of the two bodies is adiabatic); μ_f is the friction coefficient, and V (m/s)

the sliding speed. The constant K $(W/m.K)$ is called the thermal conductivity.

The thermal displacements can thus be written with a double convolution product in two dimensions, and an integral with respect to ξ_3:

$$\begin{aligned} u_3^t(x_1, x_2) &= \frac{\alpha(1+\nu)}{\pi} \int_0^{+\infty} (q ** G^T ** G^U) \cdot d\xi_3 \\ &= \frac{\alpha(1+\nu)}{\pi} q ** \int_0^{+\infty} (G^T ** G^U) \cdot d\xi_3 \end{aligned} \tag{2.51}$$

The calculation of the convolution product requires a great analytical effort, because of the inherent singularity due to the Green functions. The result has been found analytically for example by [Lin73], for the steady state regime:

$$\int_0^{+\infty} (G^T ** G^U) \cdot d\xi_3 = \frac{1}{2K} \cdot \left(\ln\sqrt{x^2+y^2} - \ln r_0\right) \tag{2.52}$$

where $r_0 = \sqrt{x_1^2 + x_2^2}$ is the distance from a reference point to the origin.
Thus, the final formulation of the thermal displacement is as follows:

$$u_3^t(x_1, x_2) = \frac{d}{2\pi} \int_{-\infty}^{+\infty} \int_{-\infty}^{+\infty} q(x_1', x_2') \left(\ln\sqrt{(x_1 - x_1')^2 + (x_2 - x_2')^2} - \ln r_0\right) \cdot dx_1' \cdot dx_2' \tag{2.53}$$

Where:

$$d = \frac{\alpha(1+\nu)}{K} \tag{2.54}$$

is the constant of distortion (m/W).

The numerical procedure requires one to discretise the domain in N_s elements of elementary surface Γ_{cn}. The expression of the thermal displacement becomes:

$u_3^t(x_1, x_2) =$

$$\frac{d}{2\pi}\sum_{n=1}^{N_s}\int_{\Gamma_{\text{cn}}} q(x_1', x_2')\left(\ln\sqrt{(x_1 - x_1')^2 + (x_2 - x_2')^2} - \ln r_0\right)\cdot d\Gamma \tag{2.55}$$

One considers that the heat flux is constant within a surface element, which leads to:

$u_3^t(x_1, x_2) =$

$$\begin{aligned} &\frac{d}{2\pi}\sum_{n=1}^{N_s} q(n)\int_{\Gamma_{\text{cn}}}\left(\ln\sqrt{(x_1 - x_1')^2 + (x_2 - x_2')^2} - \ln r_0\right)\cdot d\Gamma \\ &= \sum_{n=1}^{N_s} q(n)\cdot D^t(n) \end{aligned} \tag{2.56}$$

with:

$$D^t(n) = \frac{d}{2\pi}\int_{\Gamma_{\text{cn}}}\left(\ln\sqrt{(x_1 - x_1')^2 + (x_2 - x_2')^2} - \ln r_0\right)\cdot d\Gamma \tag{2.57}$$

The functions D^t are integrated on an elementary rectangle of center $\Re(r_1, r_2)$ and dimensions $2\Delta x_1 \cdot 2\Delta x_2$. One obtains:

$$\begin{aligned} D^t = \frac{d}{2\pi}[&g(r_{1u}, r_{2u}) + g(r_{1l}, r_{2l}) - g(r_{1u}, r_{2l}) - g(r_{1l}, r_{2u}) - 4\cdot\Delta x_1 \\ &\cdot \Delta x_2 \cdot \ln r_0] \end{aligned} \tag{2.58}$$

with:

$$\begin{aligned} r_{1u} &= r_1 + \Delta x_1 \qquad & r_{2u} &= r_2 + \Delta x_2 \\ r_{1l} &= r_1 - \Delta x_1 \qquad & r_{2l} &= r_2 - \Delta x_2 \end{aligned} \tag{2.59}$$

And:

$$g(x, y) = \frac{1}{2}\left[xy\cdot\ln(x^2 + y^2) - 3xy + x^2\cdot\tan^{-1}\frac{y}{x} + y^2\cdot\tan^{-1}\frac{x}{y}\right] \tag{2.60}$$

2.1.5.3 Surface residual displacements

The calculation of the normal residual displacement of the contacting surfaces is needed to update $h_i(x_1, x_2)$ in Eq.(2.4), which will be described in section 2.2.1. It requires one to discretise the plastic zone Ω_p into N_v cuboids Ω_{cn}. The displacement along the normal axis u_3^r generated by those N_v elementary cuboids can be written from Eq.(2.24):

$$u_3^r(A) = 2\mu \sum_{n=1}^{N_v} \int_{\Omega_{\mathrm{cn}}} \varepsilon_{ij}^p(n) \cdot \varepsilon_{3ij}^*(M,A).d\Omega \tag{2.61}$$

Considering that the plastic strains are constant in the cuboids, it yields:

$$u_3^r(A) = 2\mu \sum_{n=1}^{N_v} \varepsilon_{ij}^p(n) \cdot \int_{\Omega_{\mathrm{cn}}} \varepsilon_{3ij}^* \cdot d\Omega = \sum_{n=1}^{N_v} \varepsilon_{ij}^p(n) \cdot D_{ij}^r(n) \tag{2.62}$$

with:

$$D_{ij}^r = \mu \iiint_{\Omega_{\mathrm{cn}}} \left(u_{3i,j}^* + u_{3j,i}^*\right) \cdot dx_1 dx_2 dx_3 \tag{2.63}$$

The calculation details of functions D_{ij}^r can be found in [Jac02] where the notation of D_{3ij} was used.
The functions D_{ij}^r are integrated on an elementary cuboid of center $\mathfrak{C}(c_1, c_2, c_3)$ and dimensions $2\Delta x_1 \cdot 2\Delta x_2 \cdot 2\Delta x_3$. One obtains:

$$\begin{aligned} D_{ij}^r = F_{ij}(c_{1u}, c_{2u}, c_{3u}) - F_{ij}(c_{1u}, c_{2u}, c_{3l}) - F_{ij}(c_{1u}, c_{2l}, c_{3u}) \\ - F_{ij}(c_{1l}, c_{2u}, c_{3u}) + F_{ij}(c_{1u}, c_{2l}, c_{3l}) + F_{ij}(c_{1l}, c_{2u}, c_{3l}) \\ + F_{ij}(c_{1l}, c_{2l}, c_{3u}) - F_{ij}(c_{1l}, c_{2l}, c_{3l}) \end{aligned} \tag{2.64}$$

with:

$$\begin{array}{lll} c_{1u} = c_1 + \Delta x_1 & c_{2u} = c_2 + \Delta x_2 & c_{3u} = c_3 + \Delta x_3 \\ c_{1l} = c_1 - \Delta x_1 & c_{2l} = c_2 - \Delta x_2 & c_{3l} = c_3 - \Delta x_3 \end{array} \tag{2.65}$$

and:

$$F_{11}(x,y,z) = \frac{1}{\pi}\left[-\nu x \ln(y+R) - (1-2\nu)\,\mathrm{z}\,\tan^{-1}\frac{y+z+R}{x}\right] \tag{2.66}$$

$$F_{22}(x,y,z) = \frac{1}{\pi}\left[-\nu y \ln(x+R) - (1-2\nu)\,\mathrm{z}\,\tan^{-1}\frac{x+z+R}{y}\right] \tag{2.67}$$

$$\begin{aligned} F_{33}(x,y,z) = \frac{1}{2\pi}\Bigg[2(1-\nu)\left(2\mathrm{z}\,\tan^{-1}\frac{x+y+R}{z} + x\ln(y+R)\right. \\ \left. + y\ln(x+R)\right) + \mathrm{z}\,\tan^{-1}\frac{xy}{R}\Bigg] \end{aligned} \tag{2.68}$$

$$F_{12}(x,y,z) = \frac{1}{\pi}\left[-2\nu R - (1-2\nu)\,\mathrm{z}\ln(z+R)\right] \tag{2.69}$$

$$F_{13}(x,y,z) = \frac{1}{\pi}\left[2\mathrm{x}\tan^{-1}\frac{y+z+R}{x} + y\ln(z+R)\right] \tag{2.70}$$

$$F_{23}(x,y,z) = \frac{1}{\pi}\left[2\mathrm{y}\tan^{-1}\frac{x+z+R}{y} + x\ln(z+R)\right] \tag{2.71}$$

with:

$$R = \sqrt{x^2+y^2+z^2} \tag{2.72}$$

2.1.6 Elastic, thermal, residual stress tensor calculation

2.1.6.1 Elastic stress tensor

The calculation of the elastic stress field due to the contact pressure is quite classical. The influence coefficients that give the stresses induced by a rectangular cell on the boundary surface of a half-space submitted to a uniform

pressure can be found for example in [Ver85]. They are quickly reminded hereafter.
From Eq.(2.30) the elastic stress tensor can be written:

$$\begin{aligned}\sigma_{ij}^{e}(B) &= C_{ijkl}\cdot\frac{1}{2}\left(u_{k,l}^{e}+u_{l,k}^{e}\right)\\ &= C_{ijkl}\cdot\frac{1}{2}\left(u_{k,l}^{pr}+u_{l,k}^{pr}\right)+C_{ijkl}\cdot\frac{1}{2}\left(u_{k,l}^{sh}+u_{l,k}^{sh}\right)=\sigma_{ij}^{pr}(B)+\sigma_{ij}^{sh}(B)\end{aligned} \tag{2.73}$$

The numerical procedure requires one to discretize the domain in N_s elements of elementary surface Γ_{cn}, for a constant depth. The term corresponding to the ij component of elastic stress tensor at depth z becomes:
Derivations give:

$$\sigma_{ij}^{pr}(B)=\sum_{n=1}^{N_s}\int_{\Gamma_{cn}} G(M,B)\cdot p(M)\cdot d\Gamma \tag{2.74}$$

And:

$$\sigma_{ij}^{sh}(B)=\sum_{n=1}^{N_s}\int_{\Gamma_{cn}} H(M,B)\cdot s(M)\cdot d\Gamma \tag{2.75}$$

Coordinates of point A are (x_1, x_2, x_3) and coordinates of point M are (x'_1, x'_2, x'_3).
Finally, since the pressure and the shear are considered to be constant within an elementary element, Eq.(2.74) and (2.75) become:

$$\sigma_{ij}^{pr}(B)=\sum_{n=1}^{N_s} p(n)\cdot\int_{\Gamma_{cn}} G(M,B)\cdot d\Gamma(M)=\sum_{n=1}^{N_s} p(n)\cdot C_{ij}^{p}(n) \tag{2.76}$$

And:

$$\begin{aligned}\sigma_{ij}^{sh}(B) &= \sum_{n=1}^{N_s} s(n)\cdot\int_{\Gamma_{cn}} H(M,B)\cdot d\Gamma(M)\\ &= \sum_{n=1}^{N_s} s(n)\cdot C_{ij}^{s}(n)=\sum_{n=1}^{N_s}\mu_f\cdot p(n)\cdot C_{ij}^{s}(n)\end{aligned} \tag{2.77}$$

The functions C_{ij}^p and C_{ij}^s are integrated on an elementary rectangle of center $\Re(r_1, r_2)$ and dimensions $2\Delta x_1 \cdot 2\Delta x_2$ at depth z. One obtains:

$$C_{ij}^p = \frac{1}{2\pi}\left[K_{ij}(r_{1u}, r_{2u}, z) + K_{ij}(r_{1u}, r_{2u}, z) - K_{ij}(r_{1u}, r_{2u}, z) \right. \\ \left. - K_{ij}(r_{1u}, r_{2u}, z)\right] \tag{2.78}$$

and:

$$C_{ij}^s = \frac{1}{2\pi}\left[L_{ij}(r_{1u}, r_{2u}, z) + L_{ij}(r_{1u}, r_{2u}, z) - L_{ij}(r_{1u}, r_{2u}, z) \right. \\ \left. - L_{ij}(r_{1u}, r_{2u}, z)\right] \tag{2.79}$$

where:

$$\begin{aligned} r_{1u} &= r_1 + \Delta x_1 \qquad & r_{2u} &= r_2 + \Delta x_2 \\ r_{1l} &= r_1 - \Delta x_1 \qquad & r_{2l} &= r_2 - \Delta x_2 \end{aligned} \tag{2.80}$$

The functions K_{ij} are defined as follows:

$$K_{11}(x, y, z) = 2(1 - 2\nu)\tan^{-1}\frac{x}{(R + y + z)} - 2\nu \cdot \tan^{-1}\frac{xy}{Rz} \\ - \frac{xz}{R(R + y)} \tag{2.81}$$

$$K_{22}(x, y, z) = 2(1 - 2\nu)\tan^{-1}\frac{y}{(R + x + z)} - 2\nu \cdot \tan^{-1}\frac{xy}{Rz} \\ - \frac{yz}{R(R + x)} \tag{2.82}$$

$$K_{33}(x, y, z) = -\tan^{-1}\frac{xy}{Rz} + \frac{xz}{R(R + y)} + \frac{yz}{R(R + x)} \tag{2.83}$$

$$K_{12}(x, y, z) = -(1 - 2\nu) \cdot \ln(z + R) - \frac{z}{R} \tag{2.84}$$

$$K_{13}(x, y, z) = -\frac{z^2}{R(R + y)} \tag{2.85}$$

$$K_{23}(x,y,z) = -\frac{z^2}{R(R+x)} \tag{2.86}$$

with:

$$R = \sqrt{x^2 + y^2 + z^2} \tag{2.87}$$

The functions L_{ij} are defined as follows:

$$L_{11}(x,y,z) = 2 \cdot \ln(y+R) + z \cdot (1-2\nu)\left(\frac{y}{R(R+z)} + \frac{z}{R(R+y)}\right) - 2\nu \cdot \frac{x^2}{R(R+y)} \tag{2.88}$$

$$L_{22}(x,y,z) = 2 \cdot \ln(y+R) - z \cdot (1-2\nu)\left(\frac{y}{R(R+z)}\right) - 2\nu \cdot \frac{y}{R} \tag{2.89}$$

$$L_{33}(x,y,z) = -\frac{z^2}{R(R+y)} \tag{2.90}$$

$$L_{12}(x,y,z) = \ln(x+R) - z \cdot (1-2\nu)\left(\frac{x}{R(R+z)}\right) - 2\nu \cdot \frac{x}{R} \tag{2.91}$$

$$L_{13}(x,y,z) = -\frac{xz}{R(R+y)} - \tan^{-1}\frac{xy}{Rz} \tag{2.92}$$

$$L_{23}(x,y,z) = -\frac{z}{R} \tag{2.93}$$

with:

$$R = \sqrt{x^2 + y^2 + z^2} \tag{2.94}$$

2.1.6.2 *Thermal Stress Tensor*

The calculation of the sub-surface thermal stress field is discussed in [Liu03], based on the work of [Seo79]. Main equations can be found in Appendix 1 for all the cases regarding the time of observation and the movement of the heat source. It is to be noted that the results are expressed in the frequency domain, for simplification reasons.

2.1.6.3 *Residual Stress Tensor*

The sub-surface residual stresses are calculated following the method proposed by Chiu [Chi77,Chi78], considering a cuboidal zone with uniform initial strains or eigenstrains and surrounded by an infinite elastic space [Chi77] or a half-space [Chi78]. The way to derivate the solution can be found in Appendix 2. The solution is calculated from the superposition of three solutions, which leads to:

$$\sigma_{ij}^{r}(M) = A_{ijkl}(M, C) \cdot \varepsilon_{kl}^{p}(C) \tag{2.95}$$

$M(x_1, x_2, x_3)$ is the point where residual stress tensor is calculated, and C is the location of cuboids of constant plastic strain. Calculations are identical to most of the previous ones, when considering constant value of plastic strain inside an elementary cuboid, allowing extracting it from the integral while discretizing the domain. Though the derivation is way more complicated since tensor A includes thirty six different terms, and depends on x_1, x_2, x_3 and the depth of the cuboid of constant plastic strain.

2.2 Numerical Resolution

2.2.1 General algorithm

The algorithm developed to solve the incremental thermo-elastic-plastic contact problem is presented Fig.2.1. A more schematic way to understand the algorithm is shown hereafter in Fig.2.2.
The initial state may include residual strains. As outlined in Fig.2.2 the thermo-elastic-plastic algorithm requires first a solver for the thermal-elastic contact problem (using the conjugate gradient method, see section 2.2.4.1) with any initial surface separation, in which the initial geometry may be modified to account for the permanent deformation of the surface due to residual strains. It requires in addition the knowledge of the normal displacement of the surface due to the temperature field created by the surface friction heating. In a more conventional manner it requires also the knowledge of the elastic displacements of the surface. Finally the stress field is computed considering the contribution of the residual strains, the contact pressure distribution and the temperature field. The plasticity model (See section 2.2.5) is then used to calculate the plastic strain increment considering also the thermal dilatation strains, enabling the calculation of the residual displacement increment. The residual surface displacement increment, which is a function of the plastic strain, is then calculated and compared to the one found during the previous step. This process is repeated until the residual displacement increment converges. Plastic strains, temperature, load, contact pressure, residual surface displacement and hardening parameters are then increased by their increment to define a new initial condition for the next loading step.

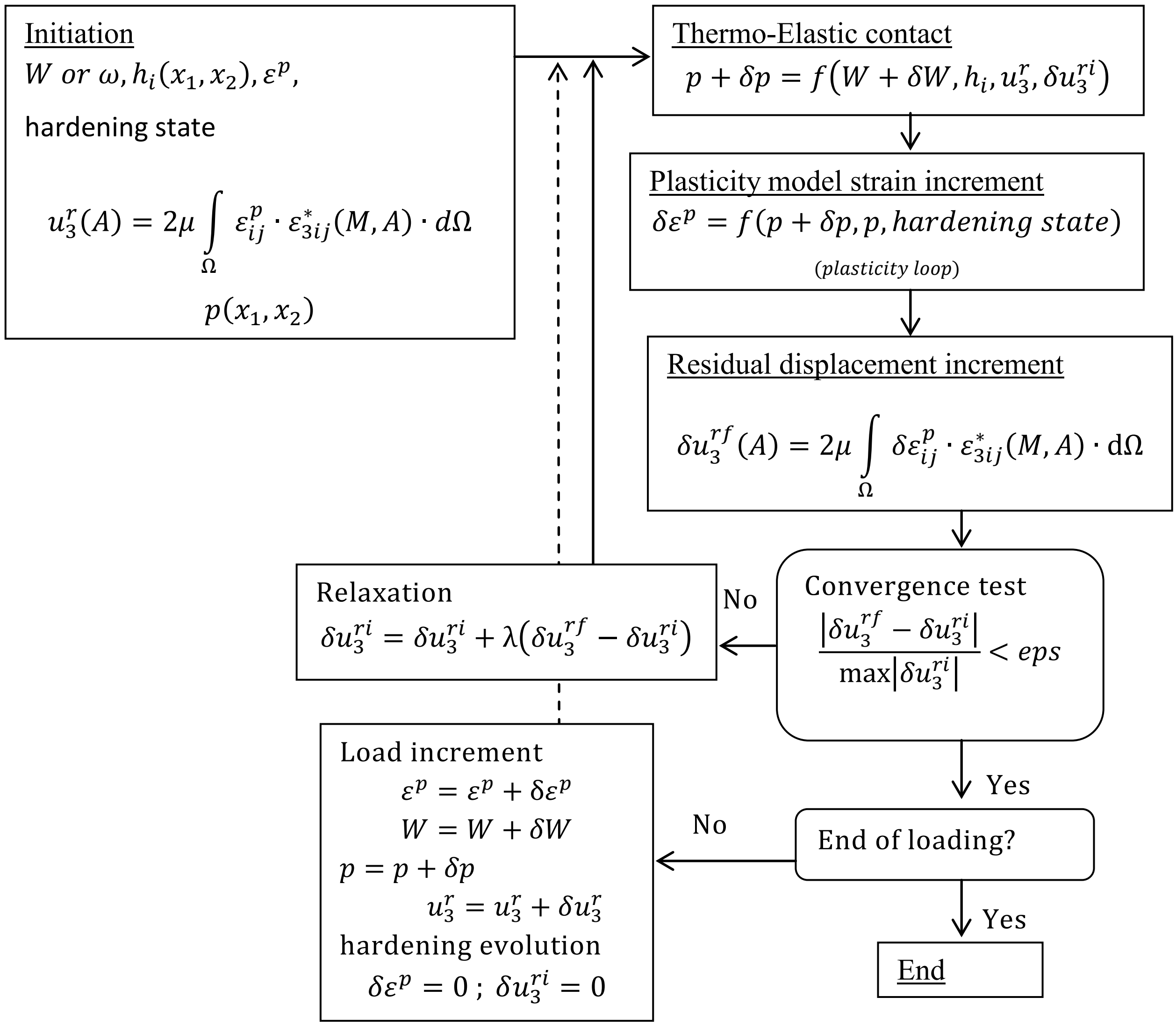

Fig.2.1 Thermo-elastic-plastic contact problem resolution algorithm

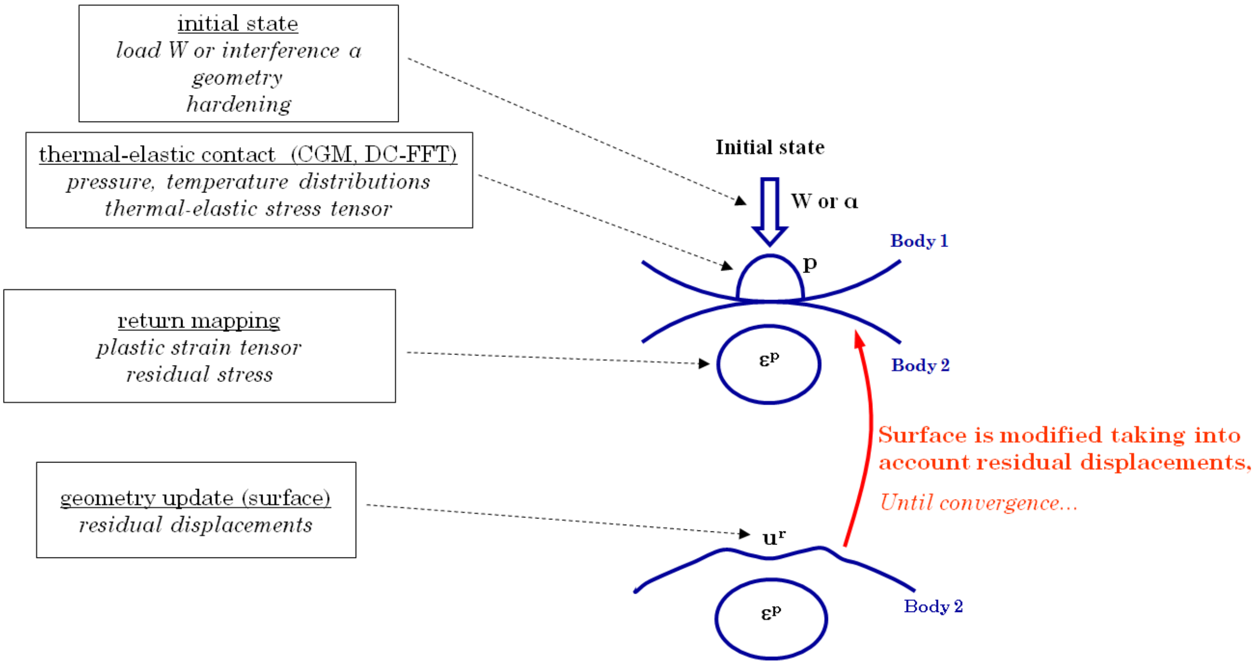

Fig.2.2 Schematic algorithm

2.2.2 Contact algorithm

As mentioned before, it is necessary to solve the thermo-elastic contact problem with an initial geometry modified to account for the surface residual displacements (incremental formulation). The solver combines the conjugate gradient method as proposed by Polonsky and Keer [Pol99] with the DC-FFT technique as used by Liu and Wang [Liu00b]. This algorithm solves simultaneously the load balance, Eq.(2.3), the surface separation, Eq.(2.4), as well as the contact conditions, Eqs.(2.5) and (2.6). The resulting surface geometry is given below:

$$h(x_1,x_2) = h_{imod}(x_1,x_2) + \omega + u_3^e(x_1,x_2) + u_3^t(x_1,x_2) \qquad (2.96)$$

Where h_{imod} takes into consideration the residual displacements, since they are added to the initial surface separation (see previous section).
Then, once the domain is discretized, the contact problem can be described by the following system of equations and inequalities (see sections 2.1.5.1 and 2.1.5.2 for the expressions of u_3^e and u_3^t):

$$\sum_{(k,l)\epsilon I_g} \left(D^p_{i-k,j-l} + \mu_f \cdot D^s_{i-k,j-l} + Q_f \cdot D^t_{i-k,j-l}\right) \cdot p_{kl} = h_{ij} + \omega, \qquad (i,j)\epsilon I_c \qquad (2.97)$$

$$p_{ij} > 0, \qquad (i,j)\epsilon I_c \qquad (2.98)$$

$$\sum_{(k,l)\epsilon I_g} \left(D^p_{i-k,j-l} + \mu_f \cdot D^s_{i-k,j-l} + Q_f \cdot D^t_{i-k,j-l}\right) \cdot p_{kl} \geq h_{ij} + \omega, \qquad (i,j) \notin I_c \qquad (2.99)$$

$$p_{ij} = 0, \qquad (i,j) \notin I_c \qquad (2.100)$$

$$a_x\, a_y \sum_{(i,j)\epsilon I_g} p_{ij} = P_0 \qquad (2.101)$$

where ω is the rigid body approach (interference) between the two solids, a_x and a_y are the grid spacings in x and y-directions respectively, P_0 is the total normal load, h_{ij} is the total separation between the two solids, I_c denotes the set of all grid nodes that are in contact, and I_g denotes the set of all grid nodes. In the case of the displacement-driven contact problem (see section 2.2.4.1) the load is unknown since a rigid body displacement is imposed, then Eq.(2.101) is not to be solved any longer. Since one equation has been removed, one unknown – the interference ω – should also be removed from the set of unknowns in the numerical procedure.

2.2.3 Algorithm improvement for two plastic bodies contact with identical material

The previous algorithm has to be improved to deal with two elastic-plastic bodies in contact. The only change in the previous model is in Eq.(2.96). Indeed, when the initial geometry is updated, it takes into account the change in both bodies geometry at the same time since h_{ij} is actually the surface separation. At the beginning of each new increment, the pressure is calculated, and this pressure repartition is applied on both counter surfaces. Then, the residual displacement calculated at the end of the increment is added to the initial geometry. If one of the bodies is elastic, then the residual displacement is basically added to the initial geometry, see Fig.2.3. Though, if the bodies are both elastic-plastic and have the same hardening behavior, then the surface separation in Eq.(2.96) becomes:

$$h_{ij} \leftarrow h_{ij} + 2 \cdot u_{ij}^r \tag{2.102}$$

because of the symmetry about the plane of contact.

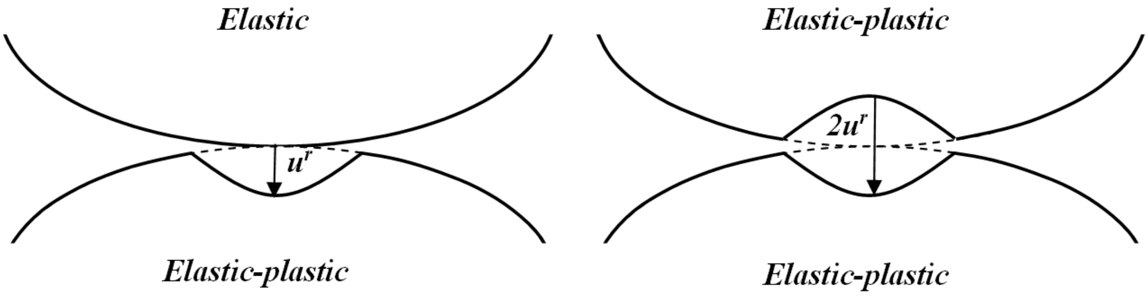

a) Elastic body against elastic-plastic body

b) Contact between two elastic-plastic bodies

Fig.2.3 Updating of the initial geometry with u^r at the beginning of a step

2.2.4 Solving the thermoelastic contact using CGM and DC-FFT

2.2.4.1 The Conjugate Gradient Method (CGM)

As the contact area I_c is unknown in advance, the procedure to solve the system of Eqs.(2.97) to (2.101) is iterative. Several iterative methods as Jacobi, Gauss-Seidel and CG are available to solve this system. Among them the CG method has important advantages:
A rigorous mathematical proof of the method convergence exists;
It offers a very high rate of convergence (super-linear);
It requires very modest storage capacity that is extremely advantageous when very large systems of equations are involved.
The CG is an iterative method which generates a sequence of approximations of the solution starting from an arbitrary initial approximation. The recurrence formula of the CG is:

$$p_{ite+1} = p_{ite} - \frac{r_{ite}^T \cdot r_{ite}}{d_{ite}^T \cdot K \cdot d_{ite}} \cdot d_{ite} \tag{2.103}$$

$$r_{ite+1} = r_{ite} - \frac{r_{ite}^T \cdot r_{ite}}{d_{ite}^T \cdot K \cdot d_{ite}} \cdot K \cdot d_{ite} \tag{2.104}$$

$$d_{ite+1} = -r_{ite+1} + \frac{r_{ite+1}^T \cdot r_{ite+1}}{r_{ite}^T \cdot r_{ite}} \cdot d_{ite} \tag{2.105}$$

where ite is the iteration inside the loop of the algorithm, r_{ite} (residue) and d_{ite} (direction) are vectors of N elements. p_0 is an arbitrary start vector (for example a uniform pressure) and $d_0 = r_0 = B - K \cdot p_0$, with $B = h - h_{imod} - \omega$ (see Eq.(2.96)).
K is called the kernel, and is equal to (see Eq. (2.97) or (2.99)):

$$K_{ij} = \left(D_{i,j}^p + \mu_f \cdot D_{i,j}^s + Q_f \cdot D_{i,j}^t\right) \tag{2.106}$$

This scheme, originally presented by Polonsky and Keer [Pol99] and then based on the conjugate gradient method (CGM) and a multi-level multi-summation method (MLMSM), was used to build the computer code. An important particularity of the iteration process is that the contact area is established in the course of the pressure iteration, so that, there is no need for further iteration with respect to the contact area. Another distinctive feature of the iteration scheme used is that the force balance equation is enforced during each iteration for the contact pressure, in the case of the load-driven formulation (when a load is imposed).
The most time-consuming works in the CGM are the multiplication operations between the influence coefficient matrix K by the pressure vector p and direction vector d. These multiplication operations require $O(N^2)$ operations and if N is large, these needs a large amount of computing time. To reduce the computing time, the Fast Fourier Transform (FFT) is used (see section 2.2.4.2) within each iteration of the CGM for the task of multiplying both pressure and direction vector by the influence coefficient matrix. The number of operations is reduced to $O(N \cdot \log N)$, where N is the number of grid points involved.

Hereafter the elastic contact algorithm used for both the ld- and the dd-formulation (load-driven and displacement-driven) are presented. For a

complete description of the algorithm for the ld-formulation and the assumptions, the reader may refer to [Pol99].
At first, an initial value of the pressure must be fixed and Eqs.(2.98) and (2.100) have to be verified. In order to verify Eqs.(2.98) and (2.100) it is required to choose non-negative values for the discrete pressure. For Eq.(2.101), for simplicity, each point of the surface is assigned a value of the pressure corresponding to the total load divided by the surface area, i.e. the number of grid points multiplied by the elementary surface area $dS = a_x \times a_y$. It is to be noticed, though, that the pressure distribution can be taken arbitrarily as long as it obeys Eq.(2.101).
For the displacement-driven formulation, the load is unknown, but could be estimated at the initial state by using the Hertz theory (see Part 1).

Two variables are introduced, δ and G_{old} that are initialized by setting $\delta = 0$ and $G_{old} = 1$.
The displacements u_{ij} are then computed and the iteration can start. The first step is the calculation of the gap g. For the displacement-driven formulation, the calculation of the gap g gives:

$$g_{ij} = -u_{ij} - h_{ij} - \omega, \qquad (i,j) \in I_g \tag{2.107}$$

For the ld-formulation the interference ω is unknown then:

$$g_{ij} = -u_{ij} - h_{ij}, \qquad (i,j) \in I_g \tag{2.108}$$

And in that case a correction needs to be made:

$$\bar{g} = {N_c}^{-1} \sum_{(i,j)\in I_c} g_{ij}\,; \tag{2.109}$$

$$g_{ij} \leftarrow g_{ij} - \bar{g}, \qquad (i,j) \in I_g \tag{2.110}$$

Where N_c is the number of points in the contact region, i.e. where the pressure is positive.
The inverted arrow notation used in Eq.(2.110) i.e. $A \leftarrow B$ means that to the quantity A is assigned the value of B.

Once g_{ij} is calculated, G is computed as follows:

$$G = \sum_{(i,j)\in I_c} {g_{ij}}^2 \tag{2.111}$$

G and G_{old} are used for the calculation of the new conjugate direction d_{ij}:

$$d_{ij} \leftarrow g_{ij} + \delta \left(\frac{G}{G_{old}}\right) d_{ij}, \qquad (i,j) \in I_c \tag{2.112}$$

$$d_{ij} = 0, \qquad (i,j) \notin I_c \tag{2.113}$$

and the value of G is stored in G_{old}:

$$G_{old} = G \tag{2.114}$$

In order to calculate the length of the step that will be made in the direction d_{ij}, r_{ij} is calculated as follow:

$$r_{ij} = \sum_{(k,l)\in I_g} K_{i-k,j-l} \cdot d_{kl}, \qquad (i,j) \in I_g \tag{2.115}$$

Since Eq.(2.115) is a convolution product, the calculation of r_{ij} is done using the DC-FFT method (see section 2.2.4.2), the same way as the displacements are calculated, then in the case of the ld formulation (this is not the case for the dd formulation), a correction needs to be made in order to be consistent with Eqs.(2.109) and (2.110):

$$\bar{r} = {N_c}^{-1} \sum_{(i,j)\in I_c} r_{ij}\,; \tag{2.116}$$

$$r_{ij} \leftarrow r_{ij} - \bar{r}, \qquad (i,j) \in I_g \tag{2.117}$$

The length of the step τ can now be calculated:

$$\tau = \frac{\sum_{(i,j)\in I_c} g_{ij}\, d_{ij}}{\sum_{(i,j)\in I_c} r_{ij}\, d_{ij}} \tag{2.118}$$

Before updating the pressure, the current pressure value is stored for the error calculation:

$$p_{ij}^{old} = p_{ij}, \qquad (i,j) \in I_g \tag{2.119}$$

The new pressure distribution is then calculated using the previous calculated step and direction:

$$p_{ij} \leftarrow p_{ij} - \tau\, d_{ij}, \qquad (i,j) \in I_c \tag{2.120}$$

After this step, Eqs.(2.98) and (2.100) must be verified. Then, for all the grid nodes where the pressure is found negative, a nil value is enforced:

$$if \quad p_{ij} < 0 \quad then \quad p_{ij} = 0 \tag{2.121}$$

Denoting I_{ol} the set of nodes where there is no contact and where the surfaces overlap, i.e.

$$I_{ol} = \{(i,j) \in I_g \ : \ p_{ij} = 0, \ \ g_{ij} < 0\} \tag{2.122}$$

then δ set equal to unity if $I_{ol} = \emptyset$. Otherwise, δ is set to zero and the pressures are corrected where the surfaces overlap:

$$p_{ij} \leftarrow p_{ij} - \tau \, g_{ij}, \qquad (i,j) \in I_{ol} \tag{2.123}$$

The current load needs now to be calculated:

$$P = a_x \, a_y \sum_{(i,j)\epsilon I_g} p_{ij} \tag{2.124}$$

In the case of the ld-formulation, Eq.(2.101) needs to be verified. Then, since the real load P_0 is usually different from the calculated load P, a correction needs to be made:

$$p_{ij} \leftarrow (P/P_0\,) \, p_{ij}, \qquad (i,j) \in I_g \tag{2.125}$$

Finally the error is computed as follow:

$$\varepsilon = a_x \, a_y \, P^{-1} \sum_{(i,j)\in I_g} \left| p_{ij} - p_{ij}^{old} \right| \tag{2.126}$$

and a new iteration is performed, unless convergence is reached, i.e. $\varepsilon \leq \varepsilon_0$, with ε_0 the prescribed error.

2.2.4.2 The Discrete-Convolution and Fast Fourier Transform (DC-FFT) method

In the Semi-Analytical formulation, displacements (see Eqs.(2.33), (2.56), (2.62)) and stresses (see Eqs.(2.76), (2.77), (2.95)) are calculated from influence coefficients that actually correspond to the Green functions in their discretized form, and either pressure or plastic strains. It can be written using double summation with indices, or in the matrix form:

$$u_{ij} = \sum_{N_x} \sum_{N_y} K_{i-k,j-l} \cdot p_{kl} \qquad or \qquad \boldsymbol{u} = \boldsymbol{A} \cdot \boldsymbol{p} \tag{2.127}$$

The size of the matrix is usually huge. If the size of the calculation zone is N, the number of operations for one double summation is $O(N^2)$, then computing times can be very long. Some numerical methods have been proposed in order to accelerate this calculation. These enable to reduce the number operation. [Bra90] used the multilevel multi summation to solve this problem, and [Ju96] proposed the FFT (Fast Fourier transform) technique. These double summations are identical to a discrete convolution product. An advantage of the FFT is that they are extensively used and a lot of routines can be found in the literature. One of the problems induced by FFT is that it is needed to increase the calculation zone, which has to be at least equal to five [Ju96] or eight times [Pol00b] the contact zone. Fortunately, [Liu00b] introduced a methodology to get rid of this inconvenient, showing that only two times the contact zone is taken to obtain accurate results, when enough care is made.
Let us introduce a one-dimensional convolution product:

$$u(x) = \int_{-\infty}^{+\infty} K(x - x') \cdot p(x') \cdot dx' = K(x) * p(x) \tag{2.128}$$

Denoting $\widetilde{K}(\omega)$ the Fourier transform of function $K(x)$, we can define:

$$\widetilde{K}(\omega) = \int_{-\infty}^{+\infty} K(x) \exp(-i\omega x)\, dx \tag{2.129}$$

The convolution theorem is obtained in applying the Fourier transform to the convolution product in Eq.(2.128):

$$\tilde{u}(\omega) = \widetilde{K}(\omega) \cdot \tilde{p}(\omega) \tag{2.130}$$

Then a simple multiplication is made in the frequency domain. Afterwards, the inverse Fourier transform yields to the result in the spatial domain:

$$u(x) = \frac{1}{2\pi} \int_{-\infty}^{+\infty} \tilde{u}(\omega) \exp(i\omega x)\, dx \tag{2.131}$$

The contact problem being solved in the discretized domain, the discrete Fourier transform Eq.(2.132) and its inverse Eq.(2.133) are introduced:

$$\widetilde{K}_s = \sum_{r=0}^{N-1} K_r \exp\left(-\frac{2\pi i r s}{N}\right), \qquad s = 0, \cdots, N-1 \tag{2.132}$$

$$K_j = \frac{1}{N}\sum_{r=0}^{N-1} \widetilde{K}_r \exp\left(\frac{2\pi i r j}{N}\right), \qquad j = 0, \cdots, N-1 \tag{2.133}$$

N being the number of calculation points.

The discrete convolution is then:

$$u_j = \sum_{r=0}^{N-1} K_{j-r}\, p_r\,, \qquad j = 0, \cdots, N-1 \tag{2.134}$$

and is expressed from a set of data of length L_0. Implicitly, the discrete convolution is realized over an infinite length, introducing a periodicity equals to L_0 of both samples to be convoluted. This is called the circular convolution, and can be expressed as:

$$u_j = \boldsymbol{K} \otimes \boldsymbol{p} = \sum_{r=0}^{N-1} K_{j-r+NH(r-j)}\, p_r\,, \qquad j = 0, \cdots, N-1 \tag{2.135}$$

using the Heaviside function:

$$H(x)\begin{cases} = 0, & if\ x < 0 \\ = 1, & if\ x \geq 0 \end{cases} \tag{2.136}$$

The number of terms of $\boldsymbol{K}$ and $\boldsymbol{p}$ is the same, $j\ \epsilon\ [0, \cdots, N-1]$. The Heaviside function is active when $j - r < 0$ which avoids negative indices for K and means to replace the index by $j - r + N$. There is then a circular summation, and it induces a periodicity in the sample. It is then possible to introduce the convolution product in the discretized form, which is related to the circular convolution product:

$$\tilde{u}_s = \widetilde{K}_s \cdot \tilde{p}_s, \qquad s = 0, \cdots, N-1 \tag{2.137}$$

[Coo65] developed a fast algorithm for Fourier transform calculation that they called FFT (Fast Fourier Transform), reducing the number of operations from to $\mathcal{O}(N^2)$ to $\mathcal{O}(N \cdot \log N)$, by taking a number of point equal to a power of 2. Later, [Sin69] improved the algorithm in order to use any number of points. In our computing code, we use Singleton's routine.

Special care needs to be made while using the convolution theorem (Eq.(2.137)) in the discretized form.
First, zero padding [Pre92] has to be done, adding zeros to the pressure while increasing the calculation zone to two times the contact zone (where the pressure needs to be calculated), see Fig.2.4.

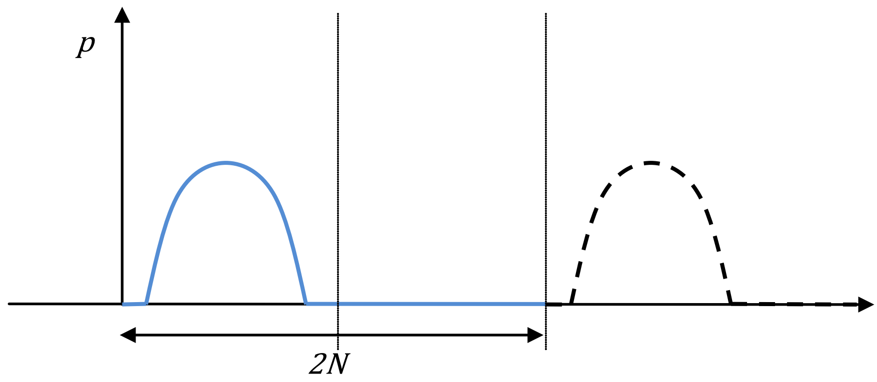

Fig.2.4 Pressure repartition – periodicity and zero padding

Then, while manipulating the influence coefficients, wrap-around order is necessary. Basically, these are calculated from 0 to N-1, then the coefficient with index N is set equal to 0 (zero-padding), then coefficients N+1 to 2N-1 are obtained from coefficient 0 to N-1 arranged in inverse order (see Fig.2.5 for the Green function corresponding to the displacement due to pressure, found in Eq.(2.34) without the integral) and sometimes in opposite sign if they are represented by an odd function (see Fig.2.6 for the Green function corresponding to the displacement due to shear, found in Eq.(2.35) without the integral).

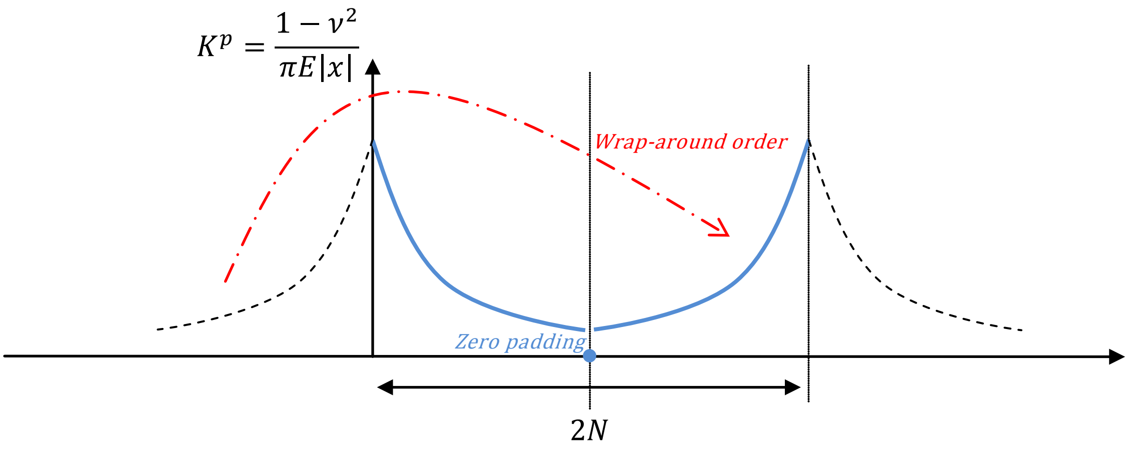

Fig.2.5 Green function for displacement due to normal pressure – wrap-around order and zero padding

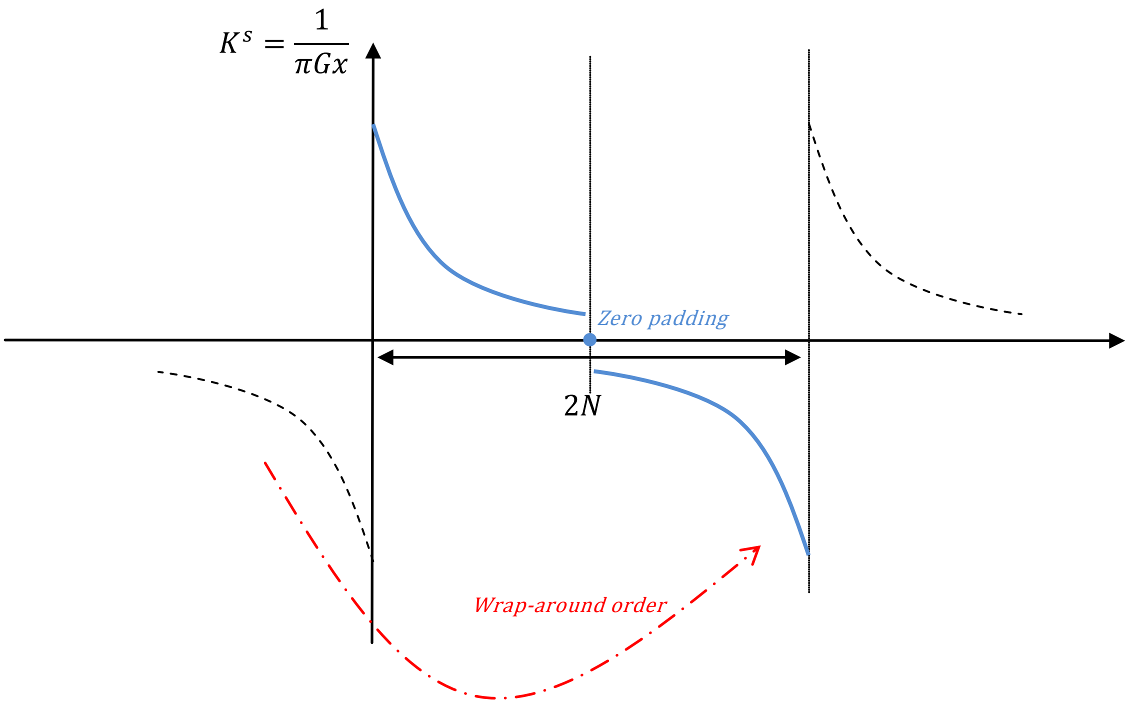

Fig.2.6 Green function for displacement due to shear – wrap-around order and zero padding

Here is the method to compute a convolution product, see [Liu00b]:

1) Compute the influence coefficients from 0 to N-1 (contact zone). In two-dimensional situations, the influence coefficients correspond to the integrated Green functions in the discretized domain, see for example Eqs.(2.36), (2.37), (2.58), (2.64) for the displacements.
2) Extend them to twice the contact zone with a zero for the coefficient numbered N (zero padding) and wrap-around order from N+1 to 2N
3) Apply FFT to obtain $\widetilde{K}_s$
4) Extend the pressure size to twice the contact zone, adding zeros (zero padding)
5) Apply FFT to obtain $\tilde{p}_s$
6) Multiply each terms $\widetilde{K}_s$ and $\tilde{p}_s$ to obtain $\tilde{u}_s$ (Eq.(2.137))
7) Apply the IFFT (inverse FFT) to $\tilde{u}_s$ and only keep the terms from 0 to N-1, to obtain $u_j$over the contact zone

2.2.5 Plasticity loop

The plasticity loop for the equivalent plastic deformation calculation was improved for convergence and accuracy needs. The proposed method is based on the work of Fotiu and Nemat-Nasser [Fot96] who built a universal algorithm for the integration of the elastic-plastic constitutive equations. Isotropic and kinematic hardening, as well as thermal softening may be used in the formulation. This method is unconditionally stable and accurate. The return mapping algorithm with an elastic predictor / plastic corrector scheme that was implemented in the code is briefly presented hereafter. The constitutive equations of plasticity are presented here.

Assuming a plastic deformation rate expressed as:

$$\dot{\varepsilon}^p = \dot{\gamma}\,\mu \tag{2.138}$$

where μ is a normalized tensor,

$$\mu = \frac{3\,\sigma'}{2\,\sigma_e} \quad , \quad \mu : \mu = \frac{3}{2} \tag{2.139}$$

with σ' the deviatoric part of the corresponding tensor.
The effective plastic strain rate $\dot{\gamma}$ is given by:

$$\dot{\gamma} = \sqrt{\frac{2}{3}\dot{\varepsilon}^p : \dot{\varepsilon}^p} \tag{2.140}$$

which gives after integration the equivalent plastic strain γ:

$$\gamma = \int_0^t \dot{\gamma} \cdot dt \tag{2.141}$$

The effective stress σ_e is defined as:

$$\sigma_e = \sqrt{\frac{3}{2}\sigma' : \sigma'} \tag{2.142}$$

The effective total strain rate which is defined as:

$$\dot{e} = \sqrt{\frac{2}{3}\dot{\varepsilon}' : \dot{\varepsilon}'} \tag{2.143}$$

Thanks to equation (2.143), the deviatoric part of the total strain rate tensor can be written as:

$$\dot{\varepsilon}' = \dot{e}\,\eta \quad , \quad \eta : \eta = \frac{3}{2} \tag{2.144}$$

The flow rule can be expressed with the following relation:

$$f = \sigma_e - g(\gamma) = 0 \tag{2.145}$$

where f is the yield function, and $g(\gamma)$ the elastic static limit.
The Kuhn-Tucker relations give the loading/unloading conditions:

$$f \leq 0 \quad , \quad \dot{\gamma} \geq 0 \quad , \quad f\dot{\gamma} = 0 \tag{2.146}$$

and should be satisfied at each time increment.

Assuming that, in the elastic regime, the material behavior is isotropic, it yields:

$$\sigma' = 2G\,(\varepsilon' - \varepsilon^p) \tag{2.147}$$

with G the elastic shear modulus (G corresponds to the Lamé constant μ, but is noted G to avoid any confusion with the normalized tensor μ used before in Eq.(2.139)).

Introducing Eq.(2.147) in the effective stress rate expression leads to:

$$\dot{\sigma}_e = \dot{\sigma}' : \mu = 2G\,\dot{\varepsilon}' : \mu - 3G\,\dot{\gamma} \tag{2.148}$$

If we consider that μ and η are co-linear, then it gives:

$$\Delta\sigma_e = 3G\,\dot{e}\,\Delta t - 3G\,\Delta\gamma \tag{2.149}$$

The formulation for the plasticity algorithm is based on an iterative scheme and divided in five steps:

(1) Compute a first "trial" state, assuming $\Delta\varepsilon'$ to be a purely elastic deformation. Subscripts a and b correspond to the initial and final states, respectively. The elastic predictor $\sigma'^{(1)}$ is then determined, which gives:

$$\sigma_e^{(1)} = \sqrt{\frac{3}{2}\sigma'^{(1)} : \sigma'^{(1)}} \quad , \quad \mu^{(1)} = \frac{3\,\sigma'^{(1)}}{2\,\sigma_e^{(1)}} \tag{2.150}$$

$$\gamma^{(1)} = \gamma_a \quad , \quad \dot{\gamma}^{(1)} = \dot{\gamma}_a \quad , \quad g^{(1)} = g_a \tag{2.151}$$

(2) Compute:

$$f^{(n)} = \sigma_e^{(n)} - g^{(n)} \neq 0 \tag{2.152}$$

(3) Linearize $f^{(n)}$ along the plastic corrector direction:

$$f_L^{(n)} = f^{(n)} + f_{,\sigma_e}^{(n)} \cdot \Delta\sigma_e^{(n)} + f_{,\gamma}^{(n)} \cdot \Delta\gamma^{(n)} = 0 \tag{2.153}$$

$$f_{,\sigma_e}^{(n)} = 1, \quad f_{,\gamma}^{(n)} = -g_{,\gamma}^{(n)} \tag{2.154}$$

and use the plastic corrector increment:

$$\Delta\sigma_e^{(n)} = -3G \cdot \Delta\gamma^{(n)} \tag{2.155}$$

to obtain:

$$\Delta\gamma^{(n)} = \frac{f^{(n)}}{3G + g_{,\gamma}^{(n)}} \tag{2.156}$$

(4) Compute the new stress and strain components:

$$\sigma_e^{(n+1)} = \sigma_e^{(n)} - 3G \cdot \Delta\gamma^{(n)} \tag{2.157}$$

$$\gamma^{(n+1)} = \gamma^{(n)} + \Delta\gamma^{(n)} \tag{2.158}$$

(5) Compute:

$$g^{(n+1)} = g\left(\gamma^{(n+1)}\right) \tag{2.159}$$

and check if:

$$\left|f^{(n+1)}\right| = \left|\sigma_e^{(n+1)} - g^{(n+1)}\right| < tol \tag{2.160}$$

where tol is the imposed tolerance.
if no: go back to (3), and repeat steps (3) – (5)
if yes:

$$(\sigma_e)_b = \sigma_e^{(n+1)} \quad , \quad \gamma_b = \gamma^{(n+1)} \quad , \quad \Delta\varepsilon^p = \Delta\gamma \cdot \mu_b \tag{2.161}$$

Comparatively to a previously used algorithm, formerly based on the Prandtl-Reuss model [Jac02], no more plasticity loop is needed, the computation of the plastic strains being reduced to a few number of iterations (typically 1 to 4 iterations for the return-mapping procedure using the Newton-Raphson scheme, step 3) resulting in a drastic reduction of the CPU time (at least by one order of magnitude) while improving the quality of the solution.

2.3 Results and Validation

2.3.1 Vertical elastic-plastic contact

In this section, the vertical elastic-plastic contact is studied. First an experimental validation is presented for a nano-indentation test. Then some comparisons with the KE-model are made. The dd-formulation (displacement-driven) as well as the EP_EP model (contact between two Elastic-Plastic bodies) are also validated through a comparison with a Finite Element simulation of a vertical loading. Then the effect of frictional heating and tangential loading is studied for a simple case.

2.3.1.1 Experimental validation

In Jacq's PhD thesis [Jac01] a nitrated material has been studied, in order to test its fatigue life capacity during rolling contact with the presence of a surface defect (indent). The aim of the following experiment is to obtain the hardening law of a layered material. For this purpose, nano-indentation tests are conducted, see [Jac03]. The experimental bench is shown in Fig.2.7. The indenter is made of diamond (see Fig.2.8), which is considered to behave elastically in the comparative simulation. Its Young's modulus is taken to be equal to 1140 MPa, and Poisson ration is 0.07. The indenter is a Berkovitch type, and radius tip is 105 µm. The reasons for the choices of materials and type of indenter can be found in [Jac01]. For the sample, Young's modulus is taken to be 210 MPa, Poisson ration is 0.3 and the Swift law is chosen for the hardening law, see Eq.(2.162), which has the advantage of well describing layered material, in choosing appropriate values of parameter B.

$$g(\gamma) = B(C + 10^{-6} \cdot \gamma)^n \tag{2.162}$$

With $g(\gamma)$ the static yield limit in MPa, γ the equivalent plastic strain, defined in Eq.(2.163), and B (MPa), C, and n three material parameters.

$$\gamma = \sqrt{\frac{2}{3}\varepsilon^p : \varepsilon^p} \tag{2.163}$$

For the considered material, $B = 1240$ MPa, $C = 30$, and $n = 0.085$. These values are taken according to El Ghazal [ElG99].

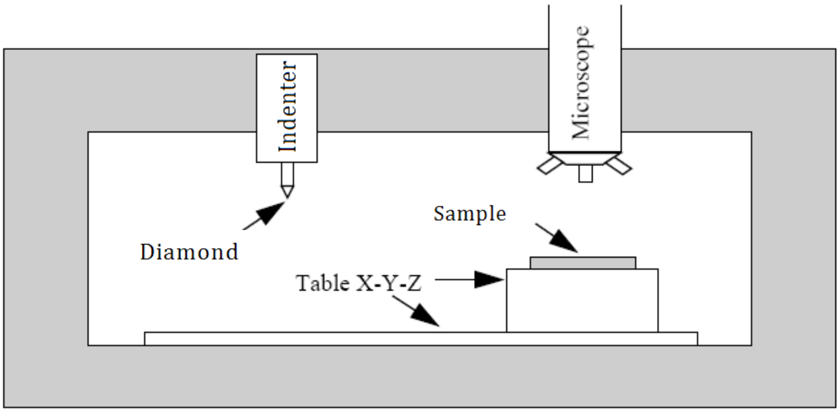

Fig.2.7 Nano-indentation experimental bench

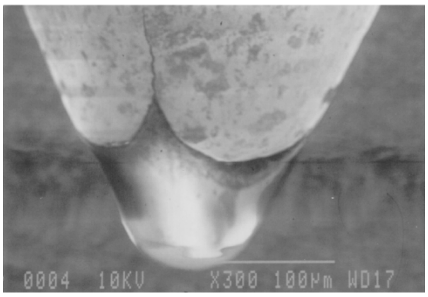

Fig.2.8 Berkovitch-type tip, made of diamond

As a result of the nano-indentation test, permanent print versus the load has been plot, and compared to the numerical simulation using the developed code.

Curves are plot in Fig.2.9, and show very good agreement between the experiment and the simulation.

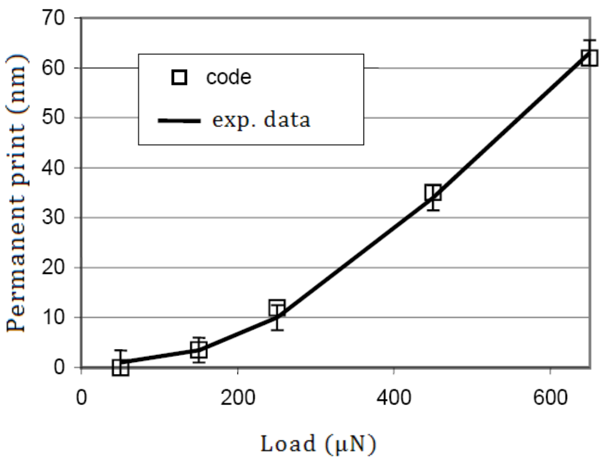

Fig.2.9 Permanent print versus the load during a nano-indentation test – comparison between experimental data and numerical simulation

2.3.1.2 Comparison with KE model (frictionless vertical contact)

The normal contact between an elastic perfectly plastic sphere and a rigid flat was recently studied by Kogut and Etsion [Kog02] and by Jackson et al. [Jac05] by FEM. Their finite element model is axisymmetric (plane strains) and the plasticity model used means that no strain hardening is considered. The first authors focused their investigation on the loaded state, whereas the second authors investigated residual stress state found after unloading. In their axisymmetric simulations no friction between the contacting bodies was considered. The effect of a tangential loading was also studied by Kogut and Etsion [Kog03] and is presented in a third paper.
A comparison is made here with the results published in [Kog02] for frictionless contact. It concerns the evolution of the plastic region in the elastic-plastic body which corresponds to the sphere in [Kog02] and to the half-space in the present analysis.
Fig.2.10 presents the evolution of the plastic zone size for increasing dimensionless interference values up to $\omega/\omega_c = 11$, where ω is the interference (or rigid body displacement) and ω_c the critical interference.

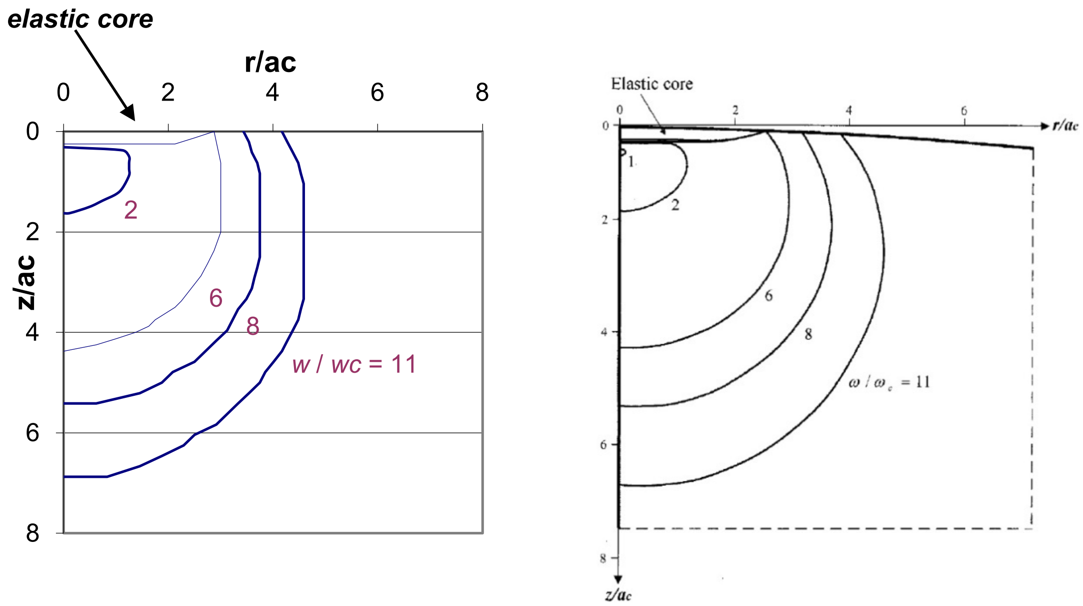

Fig.2.10 Plastic zone evolution for $2 < \omega/\omega_c < 11$ (from [Kog02] for the right hand side)

The critical interference marks the transition between the elastic and elastic-plastic deformation regimes and its expression is:

$$\omega_c = \left(\frac{\pi K H}{2E}\right)^2 R \tag{2.164}$$

with H the sphere hardness, related to the yield stress S_y by $H = 2.8 \cdot S_y$, K the hardness coefficient related to Poisson coefficient ν of the sphere by $K = 0.454 + 0.41\nu$, and E the equivalent Young's modulus. The radius of the plastic zone normalized by the critical contact area radius a_c – corresponding to the limit between elastic and elastic-plastic behaviors – is reported on the x-axis. The depth of the plastic zone also normalized by the critical radius a_c is reported on the y-axis. A comparison with the results obtained by a FEM analysis (on the right hand side of Fig.2.10) shows a fairly good agreement. The elastic core found at the surface of the sphere by the FEM analysis when $\omega/\omega_c = 2$ is also observed with the present model. This elastic core, which remains locked between the plastic region and the sphere surface, is also found to gradually shrink when the interference increases above $\omega/\omega_c = 6$ as discussed by Kogut and Etsion.

A similar comparison is given Fig.2.11 for $12 \leq \omega/\omega_c \leq 110$. A fairly good agreement is found again, despite a small discrepancy at high interference.

This difference may be attributed to the fact that the present semi-analytical approach is limited to small strains, typically a few percent, in order to keep valid the superimposition of the final elastic and plastic contributions. Fig.2.12 presents the evolution of the maximum equivalent plastic strain (see Eq.(2.163)) with the dimensionless interference, and shows that for $\omega/\omega_c = 28$, the equivalent plastic strain exceeds 5%, value beyond which we consider that the small strains assumption cannot hold anymore.

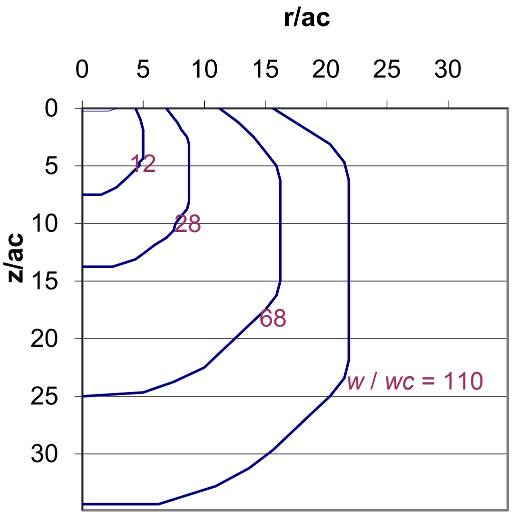

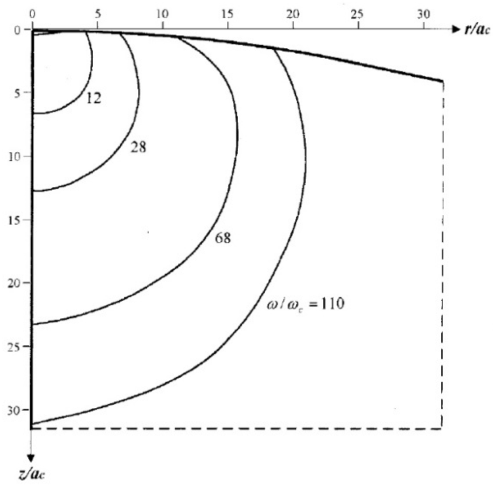

Fig.2.11 Plastic zone evolution for $12 \leq \omega/\omega_c \leq 110$ (from [Kog02] for the right hand side)

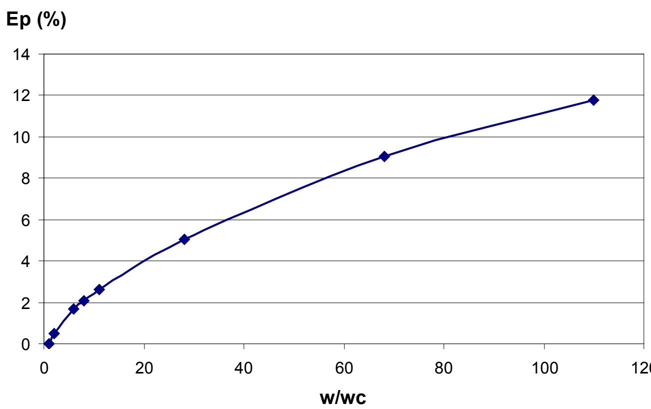

Fig.2.12 Equivalent plastic strain versus ω/ω_c for $\omega/\omega_c \leq 110$

In general, a contact surface transmits tangential traction due to friction in addition to normal pressure. That results in i) an increase of the total loading and ii) the move toward the surface of the point where the maximum of the equivalent stress is found. As discussed by Kogut and Etsion for frictionless contact the plastic zone reaches the surface when the interference ratio $\omega/\omega_c = 6$. Adding a uniformly distributed tangential traction on the surface of the half-infinite body decreases the interference ratio at which the plastic zone reaches the surface, see Fig.2.13, typically below 1 for high friction coefficient. This is not surprising since the critical interference ratio is defined here for frictionless contact, whereas the presence of tangential loading results in a decrease of the critical load (or interference) at the onset of yielding.

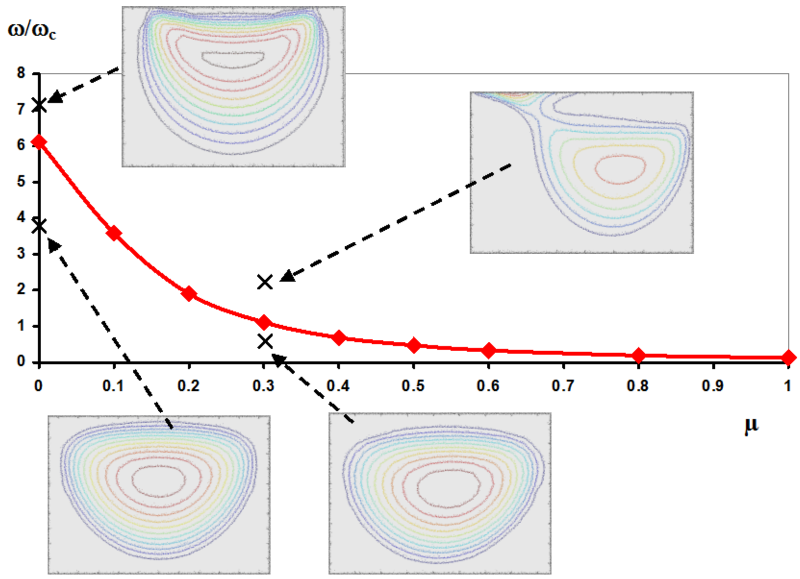

Fig.2.13 Interference ratio ω/ω_c versus friction coefficient μ_f when the plastic zone reaches the surface. The windows indicate the equivalent plastic strain after unloading for different normal load (interference ratio) and friction coefficient.

2.3.1.3 Validation of the dd-algorithm

In the case of the contact between an elastic-plastic body and a rigid punch (nano-indentation test), the load-driven formulation has been validated with the Finite Element software Abaqus in [Jac02], and also experimentally, see section (1.3.1.1). For this simulation, the elastic-plastic body is a flat made of a bearing steel used in aeronautic applications. The elastic properties of this steel are identical to the ones in section (1.3.1.1) i.e. $E = 210$ GPa for the Young modulus, and ν =0.3 for Poisson ratio. The Swift law is again used to describe the hardening behavior, see Eq.(2.162) and the chosen parameters are , $B = 1240$ MPa, $C = 30$, and $n = 0.085$.
For the rigid punch, a sphere with radius 105 μm is chosen (nano-indenter tip). The load is progressively applied until 0.650 N and then the two bodies are unloaded until no contact occurs anymore.
Fig.2.14 and Fig.2.15 present a comparison between the load-driven and the displacement-driven formulations.

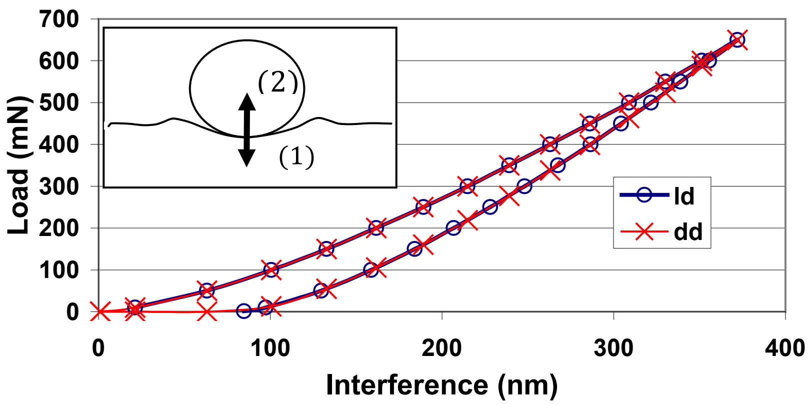

Fig.2.14 Load (mN) vs. interference during the loading / unloading phases. Max load 0.650 N / Max interference 372 nm

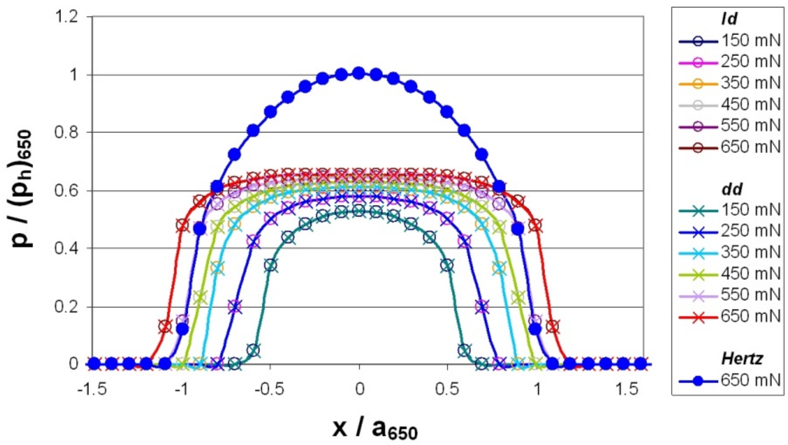

Fig.2.15 Pressure distribution during the loading phase, in the plane y=0. Maximum load 0.650 N

Fig.2.14 gives the evolution of the load versus the interference during loading and unloading. It is observed here the influence of both plasticity and conformity change due to permanent deformation of the surface, since the curves are really different for the loading and the unloading phases. Plasticity is a phenomenon that depends on the loading history.
The pressure distribution in the plane y=0 (longitudinal plane) for an increasing load is given in Fig.2.15. The pressure distribution is found flattened compared to the Hertz solution. This is due mostly to hardening of the elastic-plastic material which tends to increase the contact area. There is also a little influence of the geometry change due to permanent deformation of the surface.
As it can be seen, a very good agreement is found, for a comparable time computation with for the mesh-size, $dx = 0.6\mu m$, $dy = 1.2\mu m$, $dz = 0.3\mu m$ i.e. $31\ x\ 17\ x\ 44\ =\ 23{,}188$ points in the plastic zone and with a total of 26 time-step increments for loading / unloading (about 25 minutes for the whole loading / unloading process on a 1.8 GHz Pentium M personal computer).

This paragraph deals with the contact between two elastic-plastic bodies. The current assumptions are that the two bodies have the same initial geometry with identical elastic properties and hardening behavior. In order to validate this extension of the algorithm, a comparison with a Finite Element simulation is made through the normal contact between two spheres.
A simple example is proposed which corresponds to the simulation of the normal contact between two spheres of radius 15 mm. The spheres are made of AISI 52100 bearing steel, with elastic properties $E = 210$ GPa for the Young modulus, and $\nu = 0.3$ for the Poisson ratio. The hardening law is again described by a Swift law, as in Eq.(2.162), with parameters $B = 945$ MPa, $C = 20$, and $n = 0.121$.
In order to compare the results for the loaded case, Fig.2.16 shows the pressure repartition at the end of the loading with a normal load of 11,179 N corresponding to a hertzian pressure of 8 GPa. The pressure p is normalized by the hertzian pressure P_h, and the abscissa x by the hertzian contact radius a. The axisymmetric FE model consists of 40,247 elements (type CAX4R) with 81,128 dof. Two EP (Elastic-Plastic) situations are presented, the first one with only one inelastic body (E_EP), the second one when both bodies are inelastic (EP_EP, with the same hardening law). As it can be seen, a very good agreement is observed between the results provided by Abaqus and the ones from the Semi-Analytical Code (SAC).

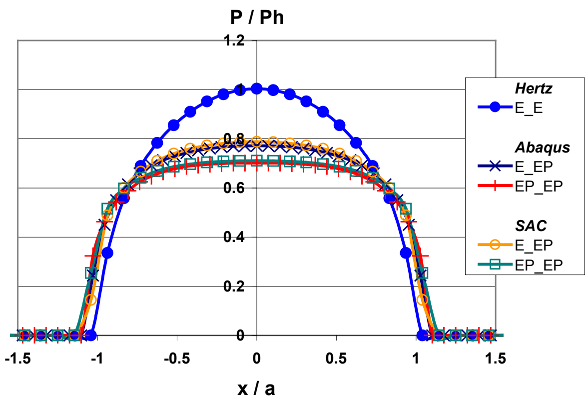

Fig.2.16 Pressure distribution at the end of loading in the plane y=0. Load 11,179N, i.e. P_h=8GPa and hertzian contact radius a=817µm.

In order to compare the results for the unloaded case, Fig.2.17 shows this time the evolution of the hydrostatic pressure when the load is removed, as defined in Eq.(2.165) versus the depth, in the same conditions as before, i.e. at the end of the loading and with the same hardening law. Again, the hydrostatic pressure is normalized by the hertzian pressure P_h, and the depth z by the hertzian contact radius a.

$$P_{hydro} = \frac{1}{3}\mathrm{tr}(\sigma) \tag{2.165}$$

with σ is the stress tensor, and tr( ) is the trace.

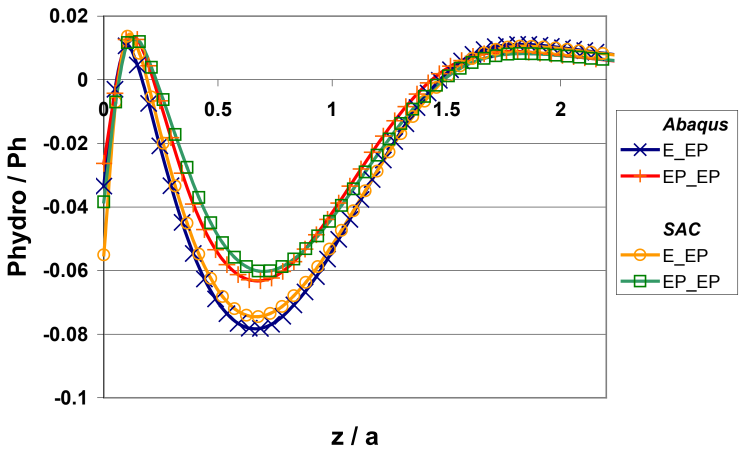

Fig.2.17 Hydrostatic pressure at the end of loading at the center of the contact. Load 11,179N, i.e. P_h=8GPa and Hertzian contact radius a=817µm.

As it can be seen again, a very good agreement is observed between the results provided by Abaqus and the ones from the Semi-Analytical Code (SAC). One may observe two regions where the residual stress state is compressive: at the Hertzian depth and at the surface, whereas two tensile regions are found: one between the surface and the Hertzian depth, but very close to the surface, and one far below the Hertzian depth.
One may also observe that the maximum compressive value is found at depth z/a=0.68, i.e. deeper than the Hertzian depth (z/a=0.48).
Almost no variation difference is found in the tensile zones, whereas an important difference in the compressive zone at the Hertzian depth is found,

the minimum value being smaller when one of the bodies is considered as elastic. For more results concerning the hydrostatic pressure, and the influence of the friction coefficient on its evolution, the reader can refer to [Nel07].
Fig.2.18 gives the maximum contact pressure and the corresponding maximum equivalent plastic strain versus the normal load at the center of the contact. The dash line indicates the plasticity threshold in term of equivalent plastic strain (see Eq.(2.163)) commonly used to define the yield stress, i.e. $\gamma = 0.2$ %, that will be used later to define the critical load at the onset of yielding. To find the aforementioned critical value, a polynomial interpolation is used:

$$P \quad (x) = \sum_{j=1}^{n} P_j^L(x) \tag{2.166}$$

where x is equal to 0.2%, and where P_j^L are the Lagrange polynoms expressed as follows:

$$P_j^L(x) = y_j \prod_{\substack{k=1 \\ k \neq j}}^{n} \frac{x - x_k}{x_j - x_k} \tag{2.167}$$

where x_j are the values of the equivalent plastic strains, and y_j the values of the loads.

One obtains then for the critical loads, $L_c = 1649$ N for the case of the contact between an elastic and an elastic-plastic bodies, and $L_c = 1743$ N for the case of the contact between two elastic-plastic bodies. The latter value will be used in what follows to present now the same results in a dimensionless form, see Fig.2.19, the maximum contact pressure P_{max} being normalized by the Hertz pressure P_h and the normal load L by the critical load L_c=1743 N. An increasing difference between the two curves with increasing load can be seen. As in Fig.2.18 one may also observed a pronounced reduction of the maximum contact pressure when considering two EP bodies compared to a purely elastic one against an EP one, up to 11% at the highest load (see Fig.2.20). Another interesting trend in Fig.2.19 is the discrepancy between the EP response compared to the Hertz solution, at the critical load, i.e. L/L_c=1. Whereas the analysis remains within the classical assumption of elastic behavior, since the plastic strain γ does not exceed 0.2%, it appears that the real contact pressure is 5% lower than the Hertz solution when considering two EP bodies. Note that the difference between the E_EP and the

EP_EP solutions is given in Fig.2.20 in term of percentage as defined by Eq.(2.168).

$$C(\%) = \frac{\left|P_{\max}^{E\_EP} - P_{\max}^{EP\_EP}\right|}{P_{\max}^{EP\_EP}} \cdot 100 \tag{2.168}$$

From Fig.2.20 it can be concluded that for $L/L_c < 1$, i.e. 4.5GPa for the hertzian pressure, the error made is less than 3%, if only one body behaves inelastically compared to two identical EP bodies in contact. It should be also noticed that, if two different elastic-plastic hardening laws are considered for the bodies in contact, the difference between the E_EP and EP_EP solutions will be lowered, making more appropriate the simplification of considering the harder material as purely elastic.

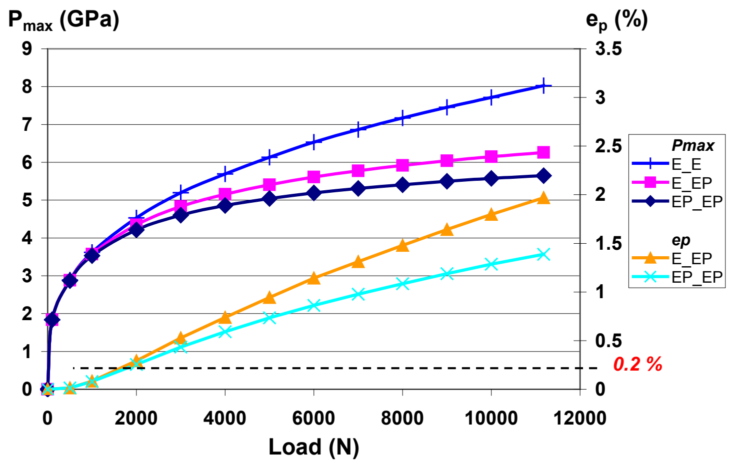

Fig.2.18 Maximum contact pressure P_{max} (GPa) and equivalent plastic strain γ (%) vs. the normal load (N).

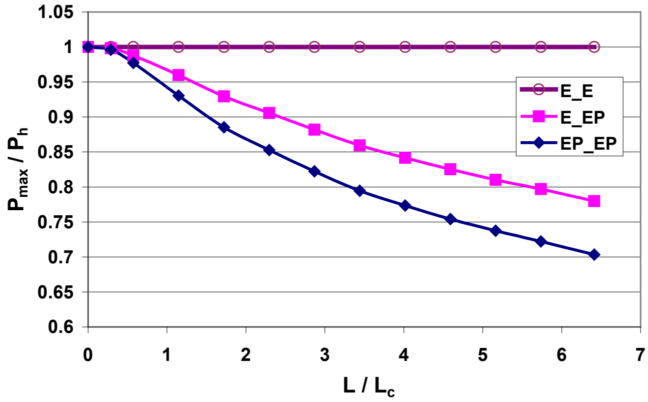

Fig.2.19 Dimensionless contact pressure vs. dimensionless load found at the center of the contact.

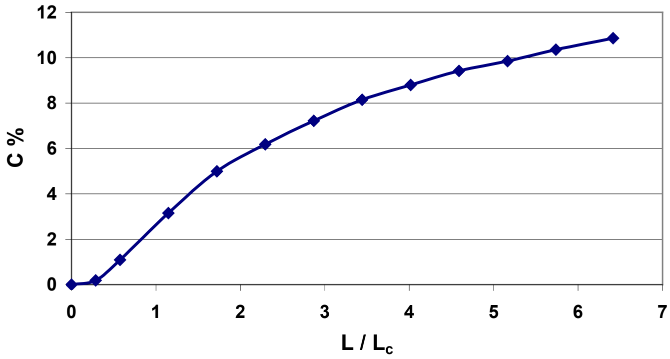

Fig.2.20 Difference between the maximum contact pressures obtained assuming an E_EP and EP_EP behavior vs. the dimensionless load L/L_c

2.3.2 Thermal-elastic-plastic contact

2.3.2.1 Validation of the thermal-elastic contact

The thermo-elastic and the elastic-plastic analyses have been validated independently in two papers [Jac02] and [Liu01b]. The surface temperature as well as the surface normal thermo-elastic displacement due to the heat source have been computed and successfully compared [Liu01b] either to the numerical solution of Tian and Kennedy [Tia94] or to the analytical thermo-elastic solutions of Johnson [Joh85] and Barber [Bar72], in the case of a uniformly distributed circular heat source and in the case of a ring heat source (uniformly distributed along the circumference). The rigid body displacement, as well as the residual stress and strain tensors found in a nano-indentation simulation have been found in agreement with the elastic-plastic solution obtained with the Abaqus Finite Element software [Jac02].

2.3.2.2 Thermal-elastic-plastic contact – some simulations

Some results are presented here for a circular point contact. Simulations have been performed for several academic examples with elastic, elastic-plastic, thermo-elastic and thermo-elastic-plastic models. They allow illustrating the effect of plasticity and temperature induced by friction on the contact pressure distribution and on the subsurface stress state at the end of loading and after unloading.
The reference problem chosen is identical to the previous section, and then corresponds to the contact between two spheres of radii 15 mm with one purely elastic and the other elastic-plastic. The elastic properties are E = 210 GPa, and ν= 0.3 for Young's modulus and Poisson ratio, respectively.
The hardening law is again described by the Swift's law, Eq.(2.162), whose parameters are $B = 945$ MPa, $C = 20$, and $n = 0.121$. These parameters correspond to the reference AISI 52100 bearing steel.

The thermal properties are $K = 50.2$ W/m.K for the thermal conductivity, α = 11.7 μm/m.K for the thermal expansion coefficient, and $\beta = 1$ for the heat partition coefficient assuming that one body is adiabatic. The friction coefficient is here chosen small ($\mu_f = 0.001$) and thus considered negligible hence simplifying the analysis of results. For some considerations about the effects of a tangential loading in the elastic-plastic analysis of a contact between two smooth surfaces or a smooth against a dented one the reader can refer to [Ant04]. The sliding speed of the adiabatic body is high resulting in a heat factor Q_f ranging from 0 to 0.5 m/s (Q_f is the product of the friction coefficient by the sliding speed). The present analysis is limited to a stationary elastic-plastic body in the steady-state regime for the thermal analysis.

It should be noted that, in the present analysis, the hardening law and material properties are assumed independent of the temperature. The application of this model to a real engineering problem requires the identification of the hardening law, which may be a function of the temperature.

In the following simulations the normal load W is gradually increased up to the maximum load. Results are presented after the last load increment or after unloading for the residual stresses.

Fig.2.21 shows a comparison of the pressure distribution found with the thermo-elastic, elastic-plastic and thermo-elastic-plastic analyses versus the conventional Hertz solution in two different situations: Fig.2.21(a) corresponds to a normal load of 1500 N and a heat factor Q_f of 0.20 m/s, Fig.2.21(b) to $W = 7500$ N and $Q_f = 0.05$ m/s. The increase of the maximum pressure in the thermo-elastic-plastic result is explained by the thermal displacement of the surface points which modifies the local conformity, resulting in a smaller contact radius [Liu01b]. The subsurface stress state is subsequently affected as discussed later.

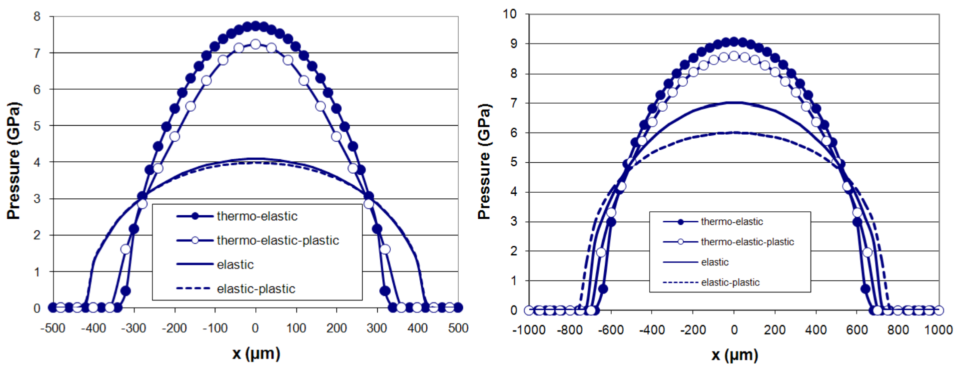

a) $W = 1500$ N, $Q_f = 0.20$ m/s b) $W = 7500$ N, $Q_f = 0.05$ m/s

Fig.2.21 Comparison between the pressure distribution with elastic, elastic-plastic, thermo-elastic, and thermo-elastic-plastic analyses

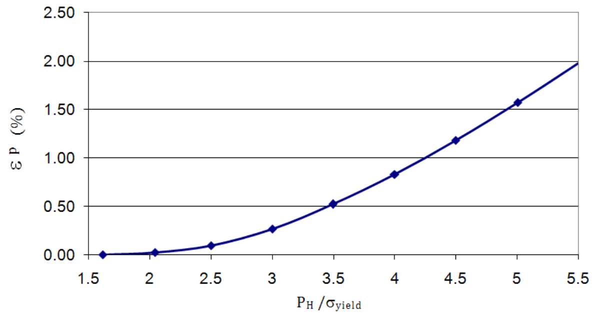

Fig.2.22 Magnitude of the equivalent plastic strain versus the equivalent Hertz contact pressure normalized by the yield stress

Fig.2.22 presents the result of an elastic-plastic analysis for an equivalent Hertz contact pressure up to 8 GPa. The equivalent Hertz contact pressure is the maximum contact pressure predicted by the elastic analysis. The maximum of the equivalent plastic strain, γ, which is found at the hertzian depth when the normal load exceeds the elastic limit, is given versus the equivalent Hertz contact pressure normalized by the micro-yield stress. The yield stress considered is the micro-yield value, 1477 MPa from Eq.(2.169) corresponding to a proof strain of 20 x 10^{-6} (see Eq.(2.163)) used to define the endurance limit of high strength steels for rolling contact fatigue applications [Lam98].

$$\sigma^y = B(C+20)^n = 945 \times 40^{0.121} = 1477\ MPa \tag{2.169}$$

The equivalent plastic strain, γ, reaches 2% at $P_H\,/\sigma^y = 5.5$ i.e. for a hertzian pressure $P_{Hertz} = 8.12$ GPa. It illustrates the fact that, whereas the model is limited to small plastic strains, it could be applied to a wide range of contact engineering situations.

Fig.2.23 presents the evolution of the critical Hertzian pressure (the maximum Hertzian pressure corresponding to the load at the onset of yielding) normalized by the micro-yield stress as a function of the heat factor. First, an increase of nearly 38% of the critical Hertz pressure is found when the heat factor is increased from 0 to 0.075 m/s. This interesting trend is explained by the effect of the dilatation thermal strains that have maximum at the surface creating high thermal stresses acting opposite to the compressive stresses due to the contact load. Second, a further increase of the heat factor above 0.075 m/s produces a linear decrease of the critical Hertz pressure, until Q_f reaches 0.152 m/s. A changing in the slope is noticed after a transition corresponding to a heat factor of 0.152 m/s. To complete the discussion, Fig.2.24 and Fig.2.25 report the location – in terms of depth

[Fig.2.24] and radius [Fig.2.25] – where the von Mises stress is found maximum under the load that corresponds to the onset of yielding as for Fig.2.23. In the left part of the curves in Fig.2.24 and Fig.2.25, i.e. for Q_f up to 0.075 m/s, the equivalent stress is found maximum in the center of the contact [Fig.2.25] at a depth moving from the Hertzian depth for $Q_f = 0$ m/s to a deeper zone when the heat factor increases [Fig.2.24]. After a transition zone found at $Q_f = 0.075$ m/s the point where the maximum von Mises stress is found sharply moves closer to the surface [Fig.2.24]. Meantime the corresponding radial location of this point is moving from the center to the edge of the contact [Fig.2.25]. After a second transition zone found at $Q_f = 0.152$ m/s, the maximum von Mises point stress reaches the surface (right part of the curve in Fig.2.24, i.e. for Q_f higher than 0.152 m/s) in the center of the contact [Fig.2.25]. Similar trends considering maximum von Mises stress are observed by Liu and Wang [Liu03] (Figs. 12 and 13) with a given Hertzian pressure and shear distribution. Unlike results presented in [Liu03], Fig.2.23, Fig.2.24 and Fig.2.25 reveal the effects of the heat factor on the magnitude of the critical Hertz pressure and on the radial location of the point where the von Mises stress is found maximum.

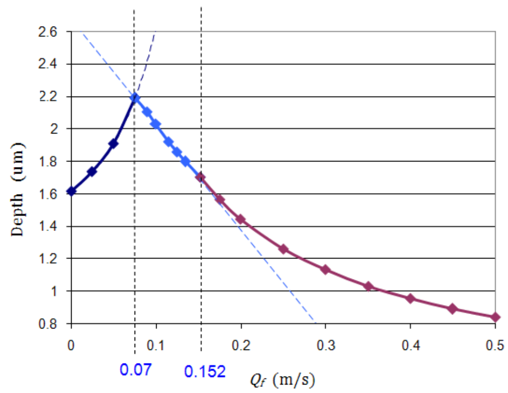

Fig.2.23 Evolution of the critical contact pressure (elastic limit pressure) versus the heat factor.

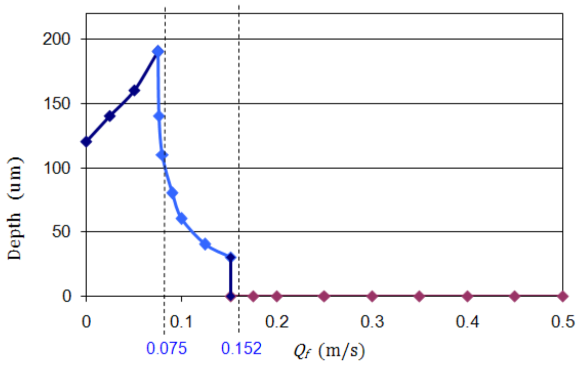

Fig.2.24 Depth of the point where the von Mises stress is found maximum versus the heat factor, at the onset of yielding as presented in Fig.2.23

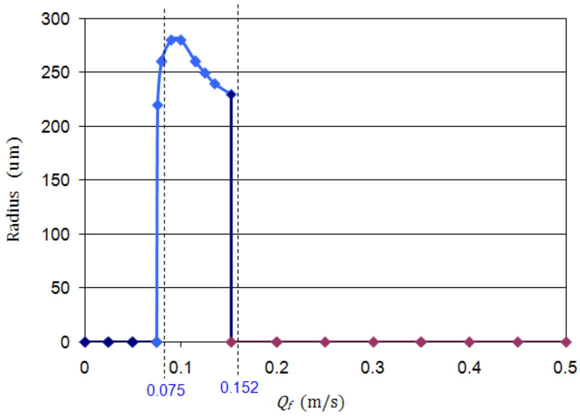

Fig.2.25 Radial position of the point where the von Mises stress is found maximum versus the heat factor, at the onset of yielding as presented in Fig.2.23

The sub-surface stress field is now studied when the applied load equals 1500 N, with four different types of analysis: elastic (Hertz), elastic-plastic, thermo-elastic and thermo-elastic-plastic, and with Q_f = 0.05 m/s, 0.12 m/s, and 0.20 m/s. The maximum von Mises stress and the depth where this stress is found are given in Table 2.1 when no frictional heating is considered, and in Table 2.2 otherwise.
The contact load at the transition between the elastic and the elastic-plastic behavior, and corresponding to the curves given in Fig.2.23, Fig.2.24 and

Fig.2.25, is also indicated, as well as the equivalent plastic strain γ (Eq.(2.163)).

	Elastic (Hertz)	Elastic-Plastic $Q_f = 0$ m/s
max von Mises stress (MPa)	2537.9	2349.1
depth (μm)	200	200
Elastic/plastic limit load (N)	-	298
γ	-	0.18%

Table 2.1 Maximum von Mises stress and its location for analyses without frictional heating ($W = 1500$ N)

	Thermo-Elastic		
	$Q_f = 0.05$ m/s	$Q_f = 0.12$ m/s	$Q_f = 0.20$ m/s
max von Mises stress (MPa)	1971.4	3501.6	7343.3
depth (μm)	240	0	0
Elastic/plastic limit load (N)	-	-	-
γ	-	-	-
	Thermo-Elastic-Plastic		
	$Q_f = 0.05$ m/s	$Q_f = 0.12$ m/s	$Q_f = 0.20$ m/s
max von Mises stress (MPa)	1939	2654.4	3186.9
depth (μm)	240	40	40
Elastic/plastic limit load (N)	491	468	212
γ	0.034%	0.51%	2.3%

Table 2.2 Maximum von Mises stress and its location for analyses with frictional heating ($W = 1500$ N)

The evolution of the pressure distribution with the heat factor is presented in Fig.2.26. One can see an obvious increase of the maximum contact pressure, associated to a decrease of the contact area since the contact load should remain identical. As discussed previously the plot with symbol '+' corresponds to the elastic or Hertz solution since the maximum contact pressure in this example is below the elastic limit as defined in Fig.2.23.

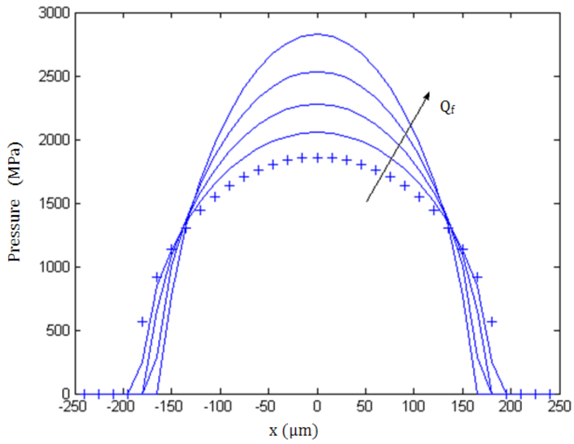

Fig.2.26 Thermo-elastic-plastic analysis: Evolution of the pressure distribution with the heat factor ($Q_f = 0$, 0.075, 0.15, 0.225, and 0.3 m/s). Plot with '+' symbol denotes the Hertz solution ($Q_f = 0$ m/s). Load: 140 N.

A cross-section view of the von Mises stress field in the plane $y = 0$ at the end of vertical loading of magnitude 1500 N is presented in Fig.2.27 to Fig.2.34. The results are plotted for the elastic solution in Fig.2.27, for the elastic-plastic analysis in Fig.2.28, for the thermo-elastic analysis with Q_f= 0.05 m/s, 0.12 m/s, and 0.20 m/s in Fig.2.29 to Fig.2.31, respectively, and for the thermo-elastic-plastic analysis with Q_f= 0.05 m/s, 0.12 m/s, and 0.20 m/s in Fig.2.32 to Fig.2.34, respectively. A classical result is that plasticity tends to attenuate the stress level, without really changing the depth at which the maximum is found, as shown by comparing Fig.2.27 and Fig.2.28. More interesting is the competition between the contact stresses and stresses induced by frictional heating, see Fig.2.29 to Fig.2.31 and Fig.2.32 to Fig.2.34. The thermo-elastic-plastic solution with a moderate heat factor (Q_f= 0.05 m/s) exhibits a zone near the contacting surface

where the stress level is lowered by thermal effects, Fig.2.29 and Fig.2.32. This zone acts also in pushing the Hertzian zone to a deeper distance from the surface, which contribute to reduce the stress level at this depth. At higher frictional heating (see Fig.2.30 and Fig.2.33 where Q_f= 0.12 m/s, and Fig.2.31 and Fig.2.34 where Q_f= 0.20 m/s) traction stresses due to thermal dilatation strains are so high that when added to the compressive contact stresses the total stress is found lower at the hertzian depth than elsewhere. At the extreme for higher heat coefficient the maximum stress is found at the surface, see Fig.2.24.
The previous discussion was focused on the stress state found under loading. A key point in a rolling contact fatigue analysis is to evaluate the residual stress state after unloading. Compressive residual stresses will close micro-cracks when present, and act to slow down their propagation. On the contrary a zone where tensile residual stresses are found will favor the coalescence of micro-cracks and their propagation. Besides the residual strains are at the origin of a permanent deformation of the initial surface. The knowledge of this permanent print on the contacting surface is also of interest since it modifies the contact conformity that contributes to lower the subsurface stress level. The maximum von Mises residual stress and its location are summarized in Table 2.3 for the same simulations as the ones presented Table 2.1 and Table 2.2. One can see the strong effect of the frictional heating on the magnitude of the maximum residual stress found after unloading. The thermal stresses are here at the origin of residual stress of magnitude 4.2 GPa for the case with Q_f= 0.20 m/s. This maximum is also found on the surface of the contacting bodies. It explains the occurrence of a shallow white etching area just below the surface in some applications operating with very high-sliding speeds [Nel97].

	Elastic-Plastic	Thermo-Elastic-Plastic		
	$Q_f = 0$ m/s	$Q_f = 0.05$ m/s	$Q_f = 0.12$ m/s	$Q_f = 0.20$ m/s
max residual stress (MPa)	135.5	25.7	877.3	4219.6
Depth (μm)	220	240	0	0

Table 2.3 Maximum von Mises residual stress and its location for several cases after unloading ($W = 1500$ N)

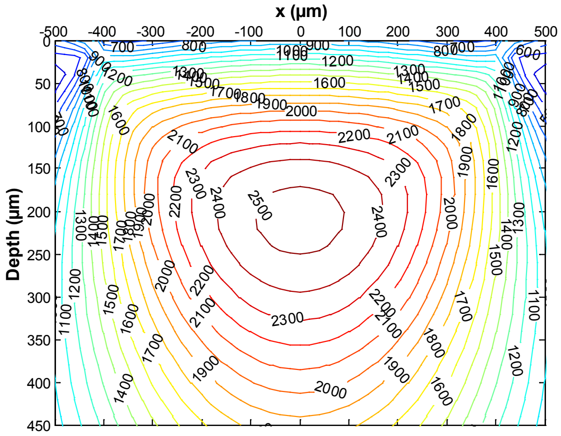

Fig.2.27 Von Mises Stress (MPa) for the elastic case (plane $y = 0$)

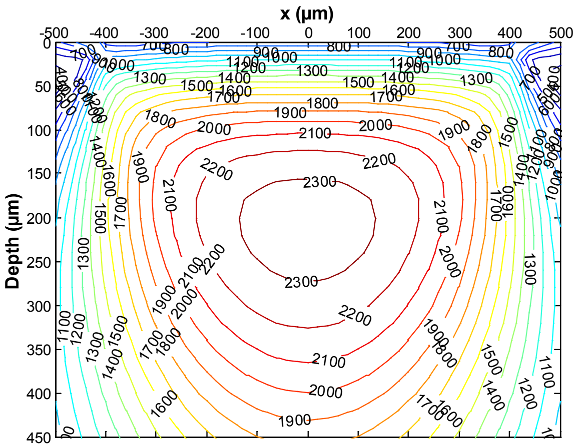

Fig.2.28 Von Mises Stress (MPa) for the elastic-plastic case (plane $y = 0$)

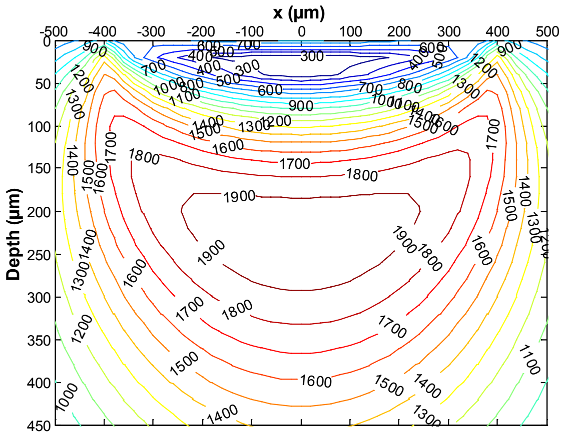

Fig.2.29 Von Mises Stress (MPa) for the thermo-elastic case with $Q_f = 0.05$ m/s (plane $y = 0$)

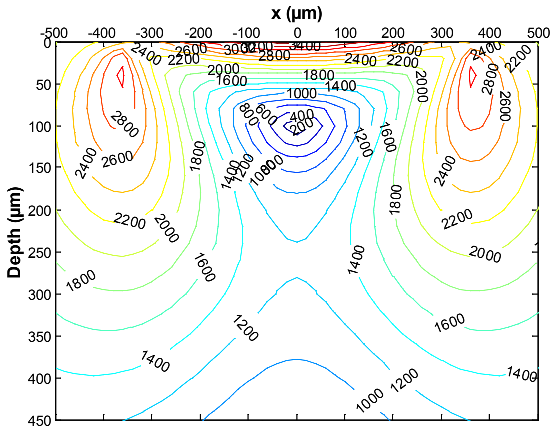

Fig.2.30 Von Mises Stress (MPa) for the thermo-elastic case with $Q_f = 0.12$ m/s (plane $y = 0$)

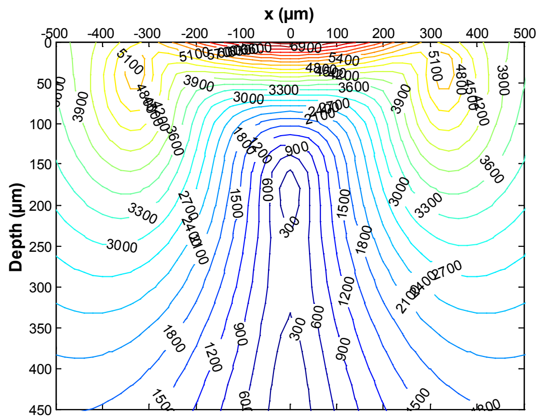

Fig.2.31 Von Mises Stress (MPa) for the thermo-elastic case with $Q_f = 0.20$ m/s (plane $y = 0$)

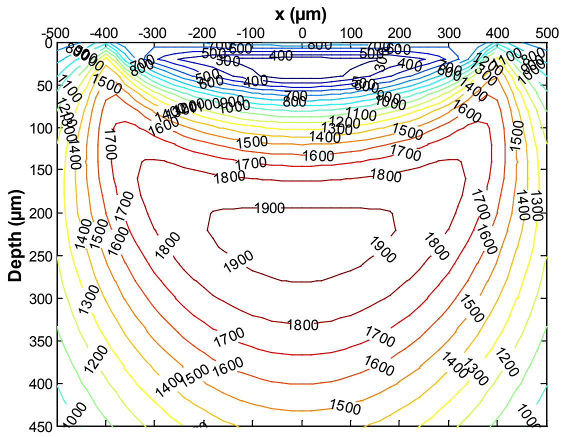

Fig.2.32 Von Mises Stress (MPa) for the thermo-elastic-plastic case with $Q_f = 0.05$ m/s (plane $y = 0$)

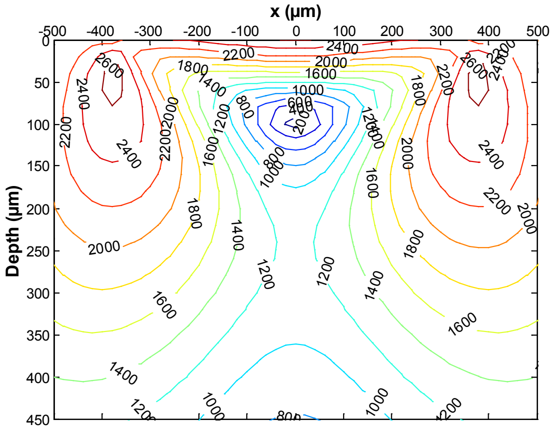

Fig.2.33 Von Mises Stress (MPa) for the thermo-elastic-plastic case with $Q_f = 0.12$ m/s (plane $y = 0$)

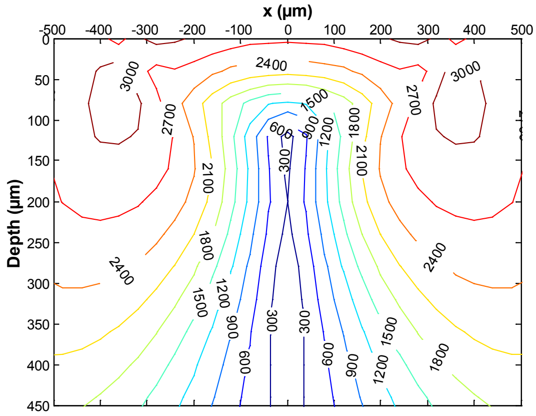

Fig.2.34 Von Mises Stress (MPa) for the thermo-elastic-plastic case with $Q_f = 0.20$ m/s (plane $y = 0$)

2.3.3 *Frictional elastic-plastic contact*

The aim of this section is first to validate the model when there is friction through comparison with FEM results in case of normal and tangential loading, and second to discuss the effect of surface traction on stress and strain fields. For convenience all results will be presented for a circular point contact between a sphere of radius 10 mm and a half-space. The sphere will be first assumed rigid when comparing SAM and FEM numerical results. The sphere will behave elastically when investigating the effect of surface traction on stress and strain states. The elastic properties are $E = 210$ GPa and $\nu = 0.3$ for Young's modulus and Poisson ratio, respectively. The half-space properties are those of M50 steel. The corresponding hardening law is described by the Swift's law, Eq.(2.162), whose parameters are $B = 1280$ MPa, $C = 4$, and $n = 0.095$ [Nel05].
Some results will be presented normalized by the micro-yield stress, σ^y (as in Eq.(2.170)), defined as the stress corresponding to a proof strain of 20×10^{-6} (see Eq.(2.163)). Eq.(2.170) gives a micro-yield stress of 1731 MPa for M50 steel, in contrast to the more conventional yield stress of 2636 MPa corresponding to a proof strain of 2×10^{-3} for the same steel (see Eq.(2.171)).

$$\sigma^y = B(C + 20)^n = 1280 \times 24^{0.095} = 1731\ MPa \tag{2.170}$$

$$\sigma^y = B(C + 2000)^n = 1280 \times 2004^{0.095} = 2636\ MPa \tag{2.171}$$

2.3.3.1 *Validation by comparison with FEM results*

To validate the results supplied by the code, a comparison with the commercial finite element code ABAQUS is made. For simplicity the upper surface is here modeled as a rigid sphere. The 3D FE model includes 113,035 C3D8 bricks (linear elements with 8 nodes) with a refined mesh in the contact zone (more than 300 elements in contact). The meshed volume is extended to 20 times the Hertz contact radius a in each direction ($-20a$ to $20a$ along x and y, 0 to $20a$ along z), assumed to be sufficient for contact analysis by FEM [Ste00]. Boundary conditions are zero displacements for

$x = \pm 20a$, $y = \pm 20a$, $z = 20a$. The normal load is imposed by a vertical displacement of the upper surface of the rigid sphere, up to a load of 800 N corresponding to a Hertz pressure of 4.35 GPa and a contact radius of 296 µm for an elastic analysis.

Fig.2.35 to Fig.2.40 present a comparison between SAM and FEM results when the loaded half-space behaves elastically. A very good agreement is found for the pressure distribution (Fig.3.35 to Fig.2.37) and the stress profile (Fig.2.38 to Fig.2.40). Results exhibit an asymmetric pressure distribution when increasing surface traction, with a shift of the maximum contact pressure in the direction of the traction force. The von Mises stress profile along the geometrical axis of symmetry is shown in Fig.2.38 to Fig.2.40. The difference between SAM and FEM numerical results is attributed to the boundary conditions in the FE model, which do not correspond exactly to an infinite half-space. Finally, the results also confirm a classical result which is that the maximum stress is found at the surface when the friction coefficient exceeds 0.3[Joh85].

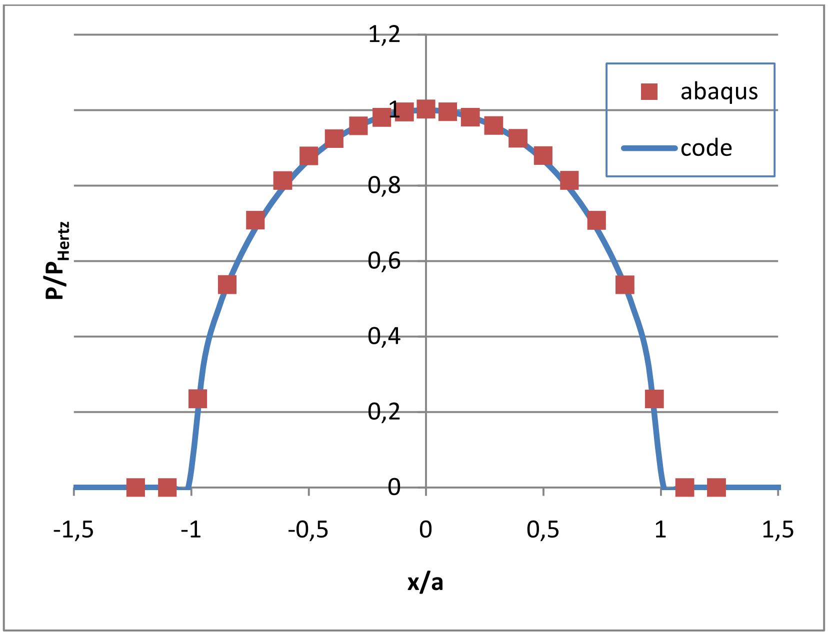

Fig.2.35 Comparison of numerical results, SAM vs. FEM, elastic solution, contact pressure distribution, for friction coefficients $\mu_f = 0$

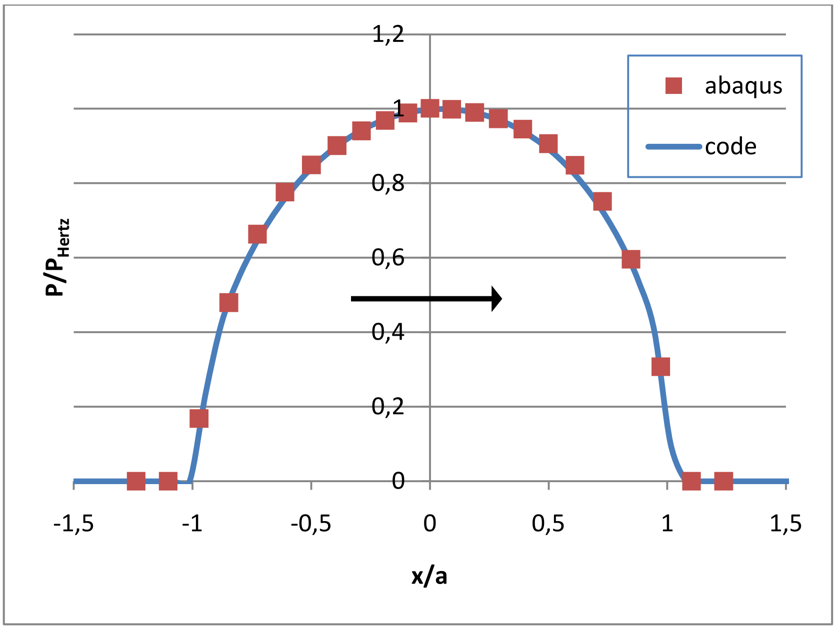

Fig.2.36 Comparison of numerical results, SAM vs. FEM, elastic solution, contact pressure distribution, for friction coefficients $\mu_f = 0.2$

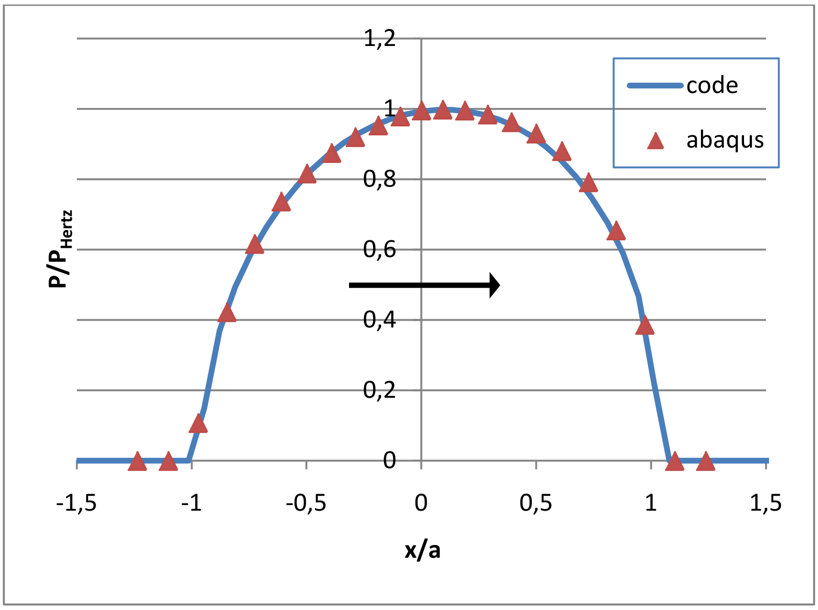

Fig.2.37 Comparison of numerical results, SAM vs. FEM, elastic solution, contact pressure distribution, for friction coefficients $\mu_f = 0.4$

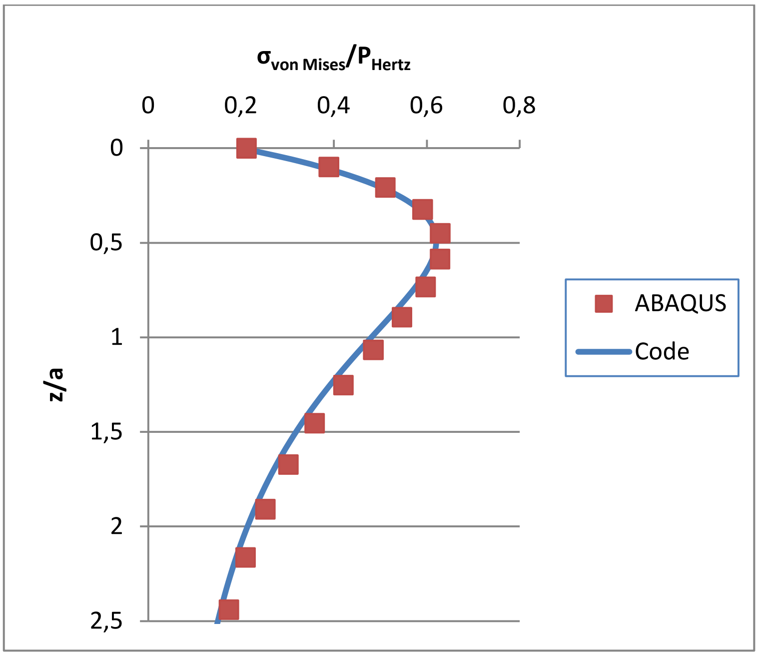

Fig.2.38 Comparison of numerical results, SAM vs. FEM, elastic solution, Von Mises stress under load (profile at x=y=0) for friction coefficients $\mu_f = 0$

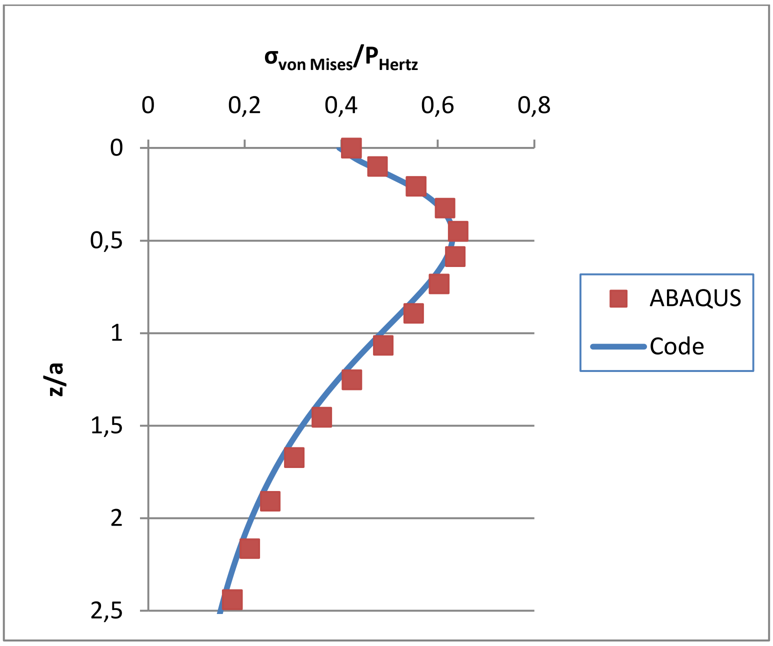

Fig.2.39 Comparison of numerical results, SAM vs. FEM, elastic solution, Von Mises stress under load (profile at x=y=0) for friction coefficients $\mu_f = 0.2$

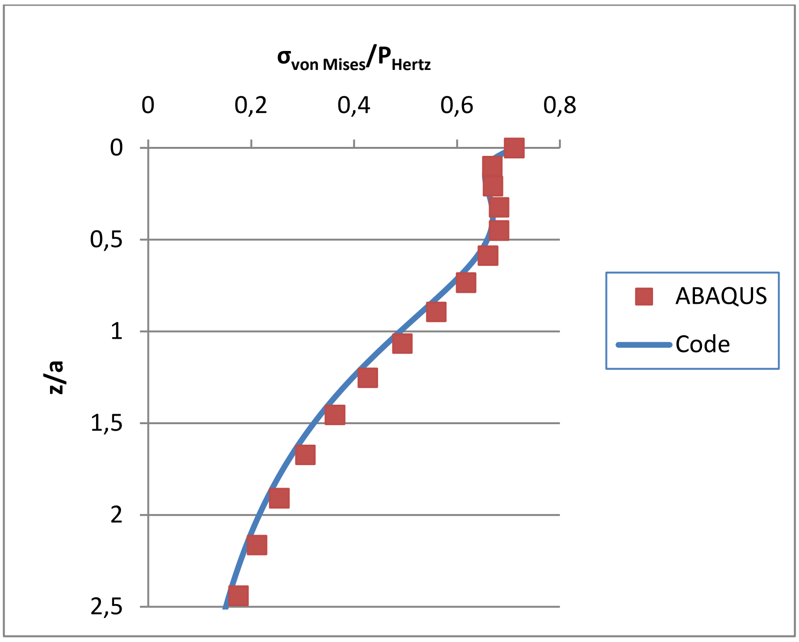

Fig.2.40 Comparison of numerical results, SAM vs. FEM, elastic solution, Von Mises stress under load (profile at x=y=0) for friction coefficients $\mu_f = 0.4$

The effects of plasticity are presented in Fig.2.41 to Fig.2.49, where the half-space behaves now as an elastic-plastic media, the load being still transmitted through an elastic sphere. Again SAM and FEM results are globally in good agreement, with some slight differences that have the same origins as for the elastic simulations. The pressure distribution (Fig.2.41 to Fig.2.43) is affected by the hardening of the material, the maximum contact pressure being lowered. At the same time the contact area tends to increase, keeping the integral of the contact pressure constant. The pressure distribution is no more found symmetric while increasing the friction coefficient (Fig.2.42 and Fig.2.43). The von Mises stress found under loading and the equivalent plastic strain are given in Fig.2.44 to Fig.2.46 and Fig.2.47 to Fig.2.49, respectively, along depth at the center of the contact.
Despite some differences, the fairly good agreement between FEM and SAM numerical results found in Fig.2.35 to Fig.2.49 validates the elastic-plastic contact solver. It should be recalled the advantage of the SAM approach in term of computing time, with less than one minute CPU time for all results presented here, compared with approximately one day of CPU time on the same personal computer for equivalent FEM analysis.

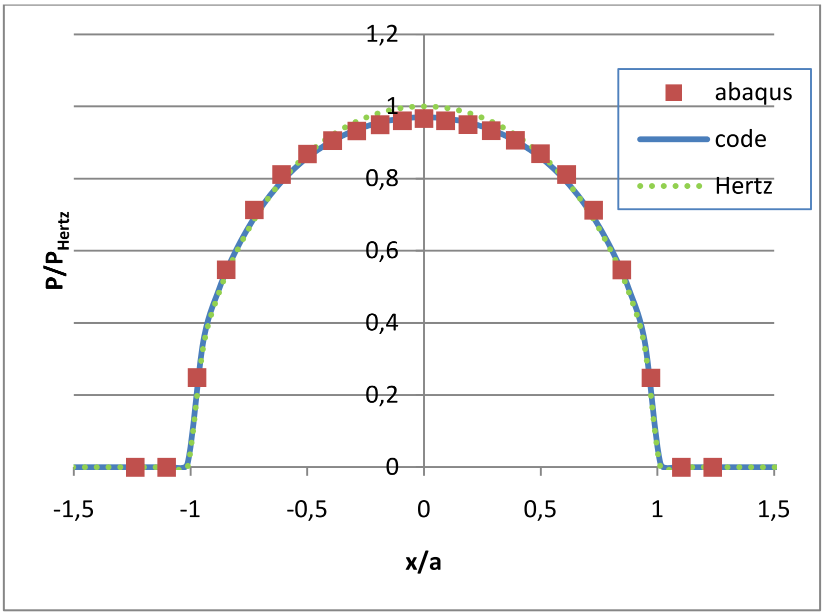

Fig.2.41 Comparison of numerical results, SAM vs. FEM, elastic-plastic solution, contact pressure distribution for friction coefficients $\mu_f = 0$

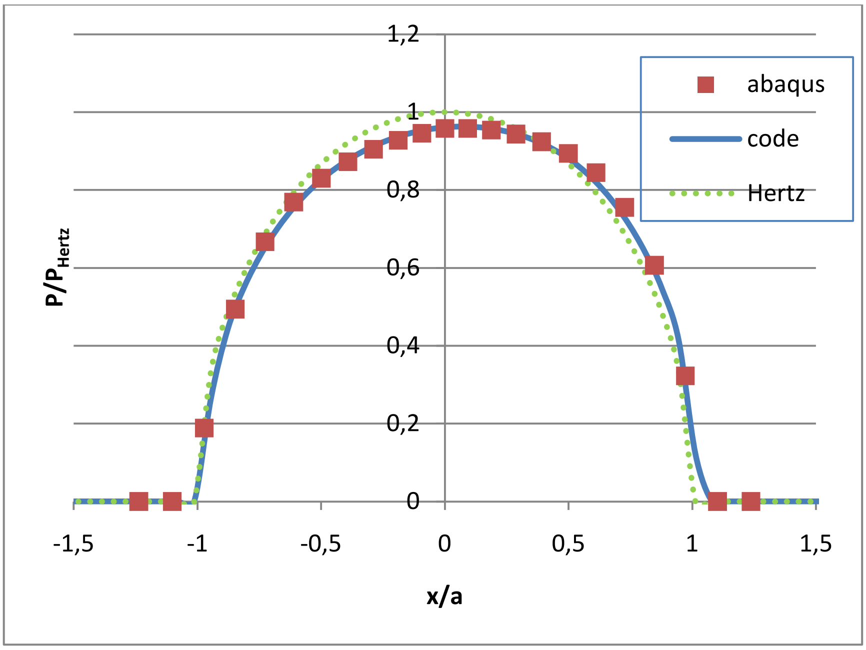

Fig.2.42 Comparison of numerical results, SAM vs. FEM, elastic-plastic solution, contact pressure distribution for friction coefficients $\mu_f = 0.2$

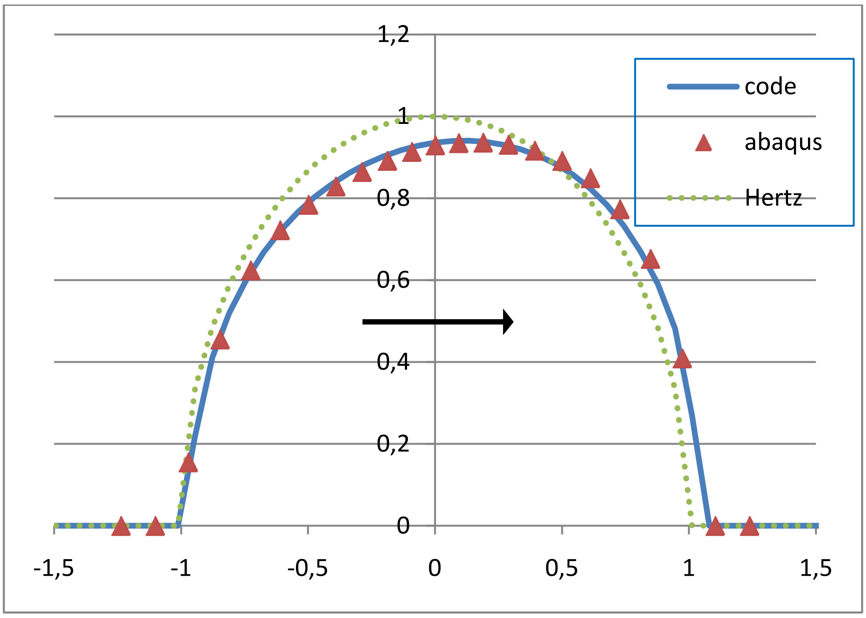

Fig.2.43 Comparison of numerical results, SAM vs. FEM, elastic-plastic solution, contact pressure distribution for friction coefficients $\mu_f = 0.4$

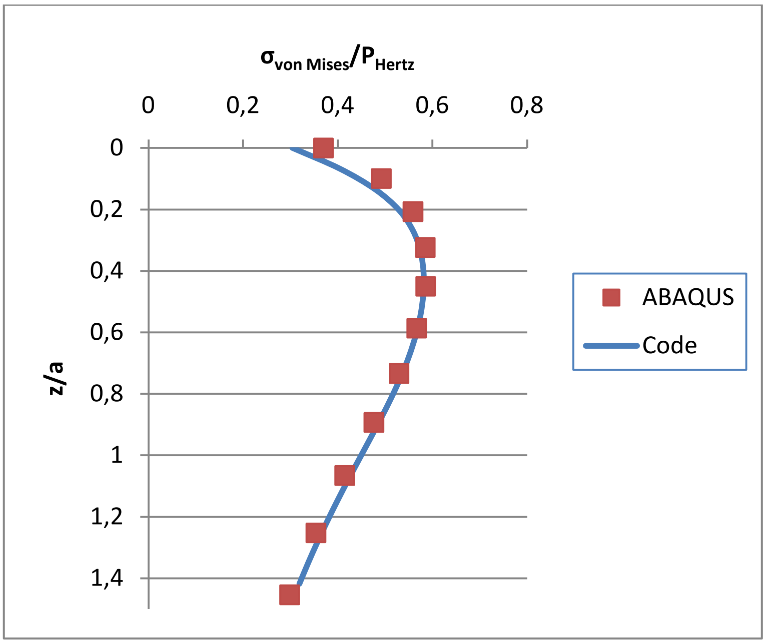

Fig.2.44 Comparison of numerical results, SAM vs. FEM, elastic-plastic solution, Von Mises stress under load (profile at x=y=0) for friction coefficients $\mu_f = 0$

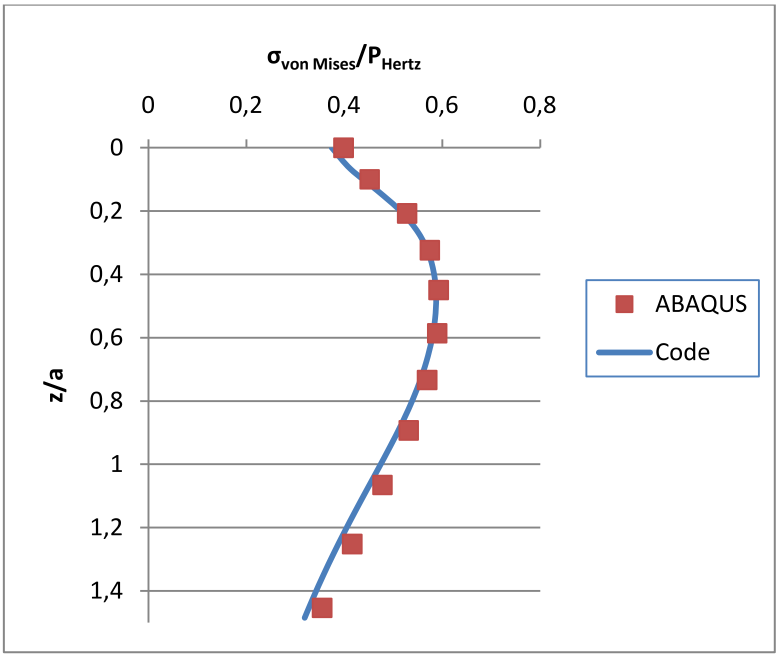

Fig.2.45 Comparison of numerical results, SAM vs. FEM, elastic-plastic solution, Von Mises stress under load (profile at x=y=0) for friction coefficients $\mu_f = 0.2$

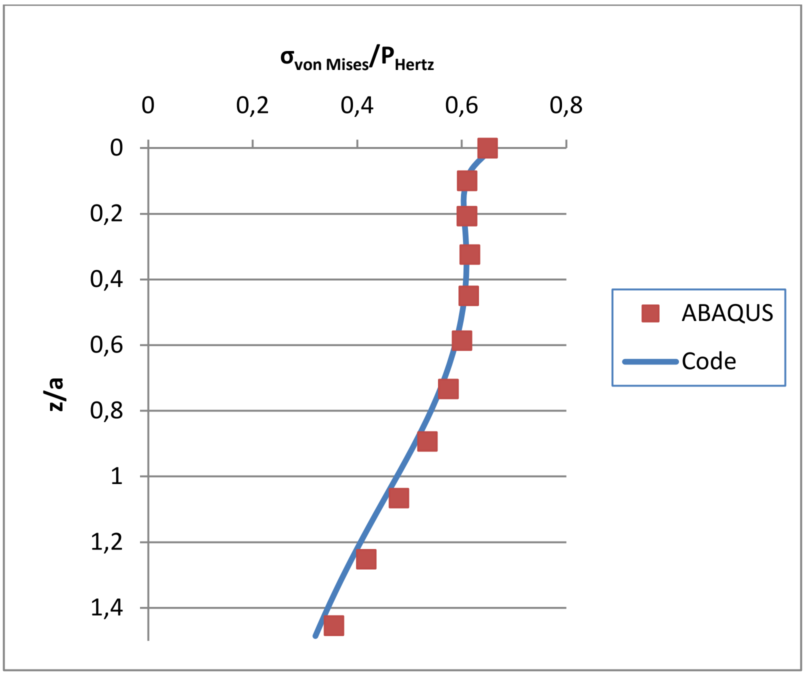

Fig.2.46 Comparison of numerical results, SAM vs. FEM, elastic-plastic solution, Von Mises stress under load (profile at x=y=0) for friction coefficients $\mu_f = 0.4$

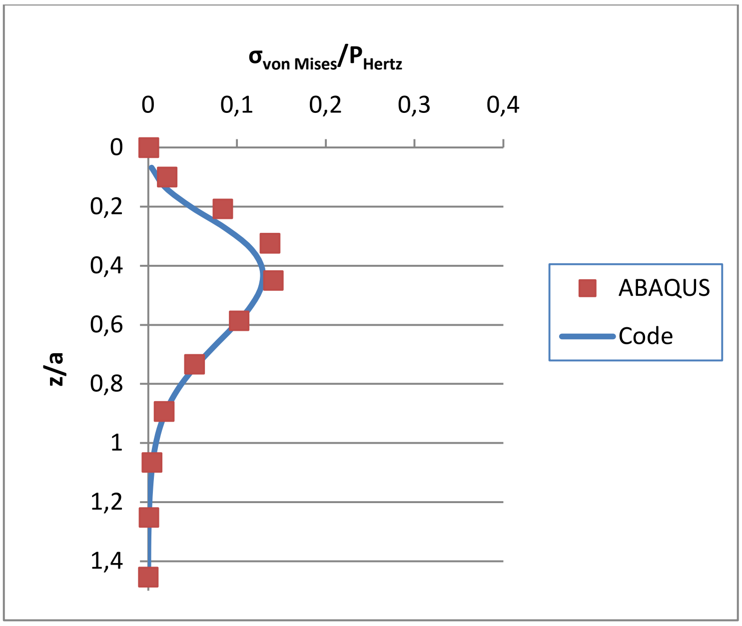

Fig.2.47 Comparison of numerical results, SAM vs. FEM, elastic-plastic solution, equivalent plastic strain (profile at x=y=0) for friction coefficients $\mu_f = 0$

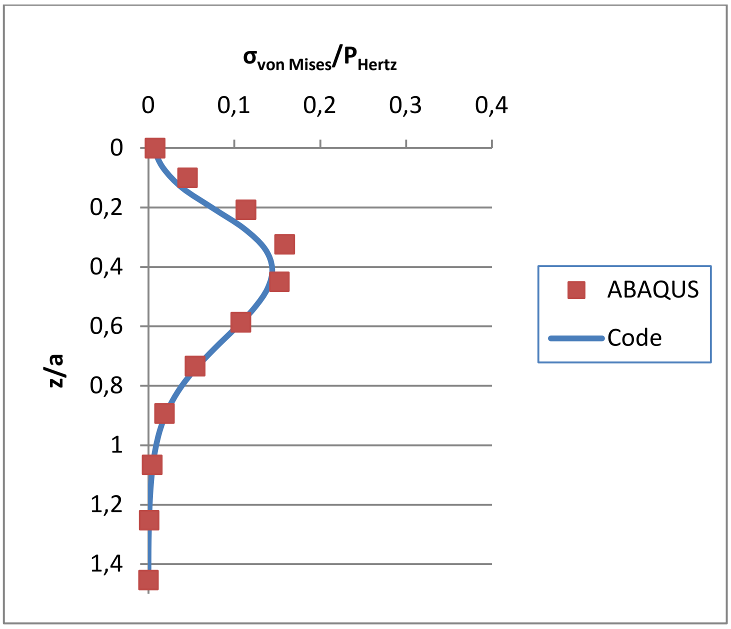

Fig.2.48 Comparison of numerical results, SAM vs. FEM, elastic-plastic solution, equivalent plastic strain (profile at x=y=0) for friction coefficients $\mu_f = 0.2$

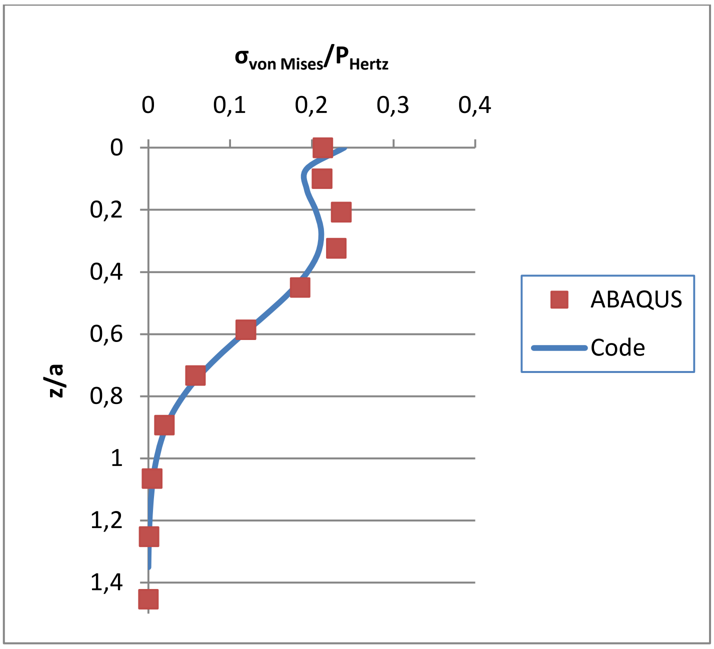

Fig.2.49 Comparison of numerical results, SAM vs. FEM, elastic-plastic solution, equivalent plastic strain (profile at x=y=0) for friction coefficients $\mu_f = 0.4$

Numerical simulations are now performed to investigate the effect of normal and tangential loading on the contact pressure distribution as well as on sub-surface stress and strain fields found under load or after unloading (residual). From this point the sphere will be modeled as an elastic body and it radius is 20 mm, still loaded against an elastic-plastic half-space. The friction coefficient will range from 0 to 0.5, and the normal load from 1 000 to 5 000 N, the latter corresponding to a Hertz (elastic) contact pressure of 5.05 GPa and a normalized interference, ω/ω_{c0}, of 3.2. The critical interference, ω_{c0}, and the critical load, W_{c0}, are the normal deflection and the corresponding normal load at the onset of yielding, as introduced by [Cha87]. Most results are presented for the maximum normal load, i.e. 5 000 N.
It should be noted that the critical interference and load, ω_{c0} and W_{c0}, respectively, are usually defined for pure normal loading [Cha87]. Considering now the effect of a tangential loading superimposed to the normal load, one may easily plot the ratios ω_c/ω_{c0} and W_c/W_{c0}, where ω_c and W_c are the value found for a contact with friction. It is found in Fig.2.50 very important effect of the friction coefficient on these critical values.

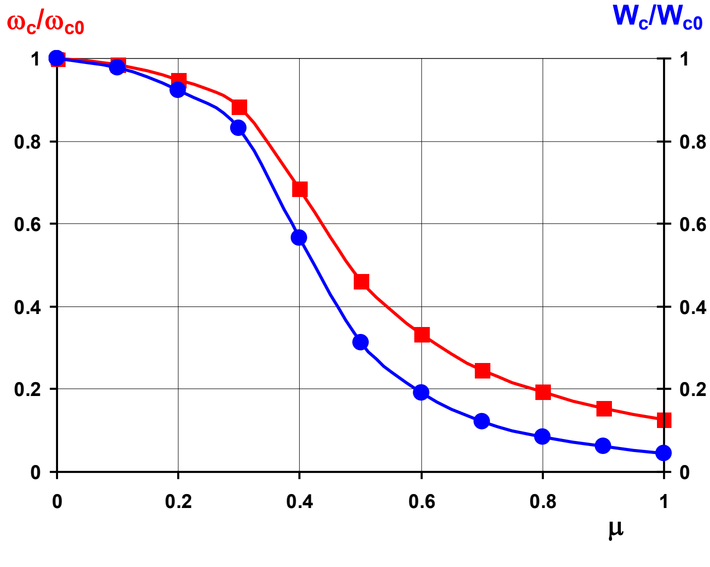

Fig.2.50 Influence of the friction coefficient on the critical load (circle symbols) and interference (square symbols) at the onset of yielding, normalized by the values for frictionless contact

The maximum of the equivalent plastic strain versus the Hertz pressure, normalized by the micro-yield stress, is presented in Fig.2.51 for different friction coefficients μ_f. The corresponding contact pressure distributions at the normal load of 5 000 N are presented Fig.2.52.

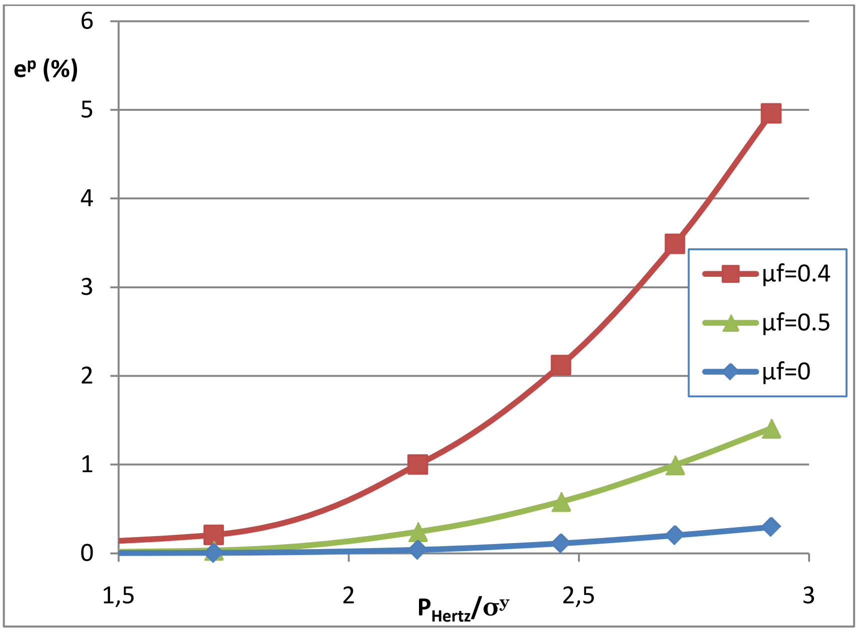

Fig.2.51 Maximum of the equivalent plastic strain versus the corresponding Hertzian contact pressure normalized by the micro-yield stress for various friction coefficients

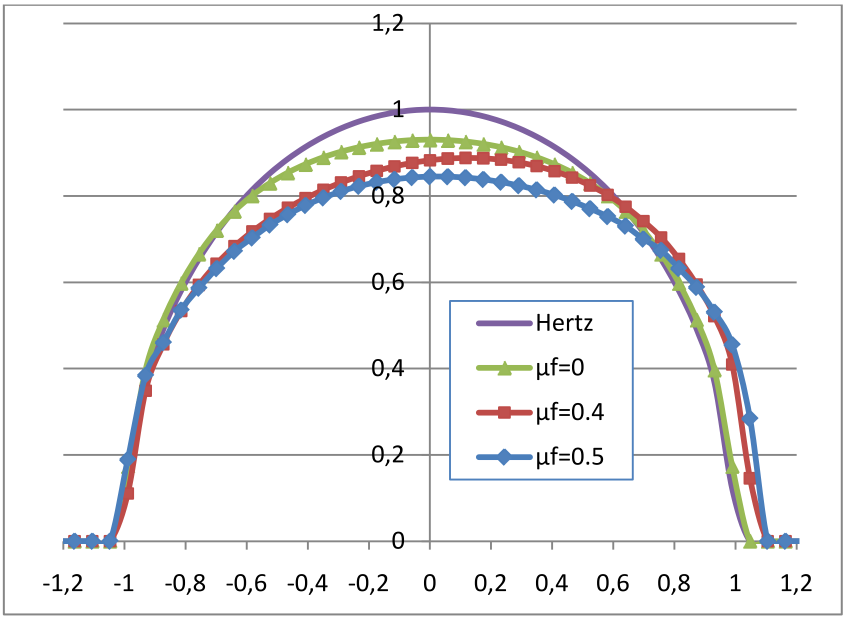

Fig.2.52 Pressure distribution for various friction coefficients. Normal load 5 000 N

It should be noticed that for $\mu_f = 0.4$ and 0.5, the maximum of the plastic strain is found at the surface of the half-space whereas it is found at the Hertzian depth for frictionless contact. Another interesting result is the magnitude of the plastic strain which reaches 5.34 % for $\mu_f = 0.5$ and a normal load of 5 000 N, remaining acceptable in regard to the assumption of small strains. Finally the marked effect of the friction coefficient should be noted, which increases drastically the maximum of the plastic strain from 0.34 % for frictionless contact at 5 000 N up to 5.34 % at $\mu_f = 0.5$.

The von Mises stress profile at the center of the contact is shown Fig.2.53 and Fig.2.54 for friction coefficient ranging from 0 to 0.5, first under load with a normal load of 5 000 N (Fig.2.53), second after unloading (Fig.2.54).

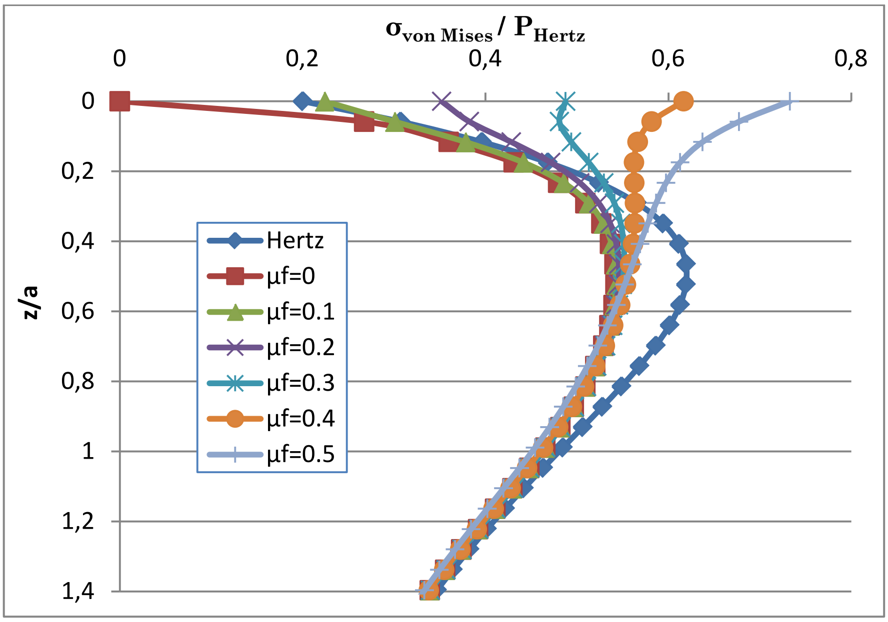

Fig.2.53 Von Mises stress profile at $x = y = 0$ under load. Normal load 5 000 N

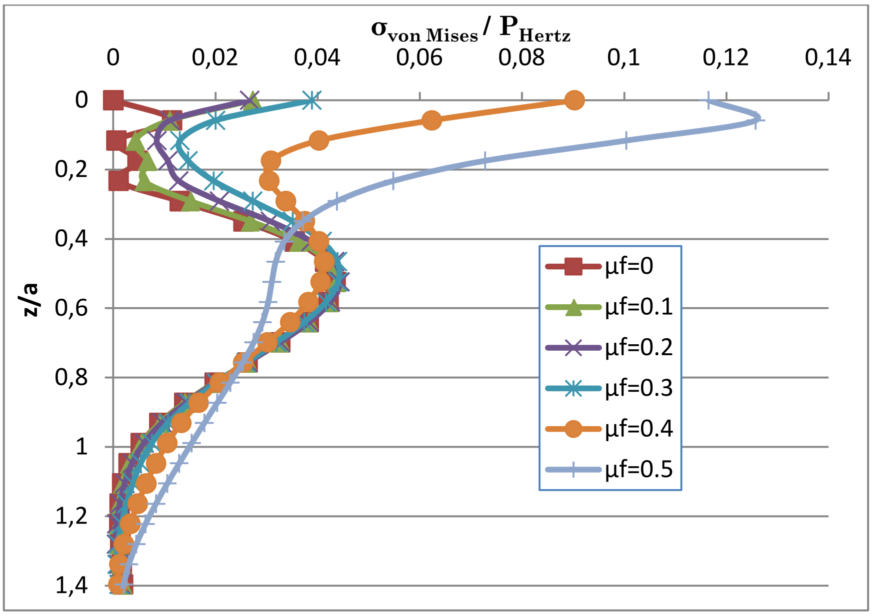

Fig.2.54 Von Mises stress profile at $x = y = 0$ after unloading (residual). Normal load 5 000 N

Three contributions of the plasticity are associated with the decrease of the maximum von Mises stress observed at the Hertzian depth in Fig.2.53: first a change of the surface conformity due to sub-surface residual strain, second the modification of the pressure distribution, and third the hardening of the material. Outside the plastic zone the stress profile follows the elastic solution (visible in Fig.2.53 for frictionless contact).

The location of the point where the maximum stress is found is presented Fig.2.55.

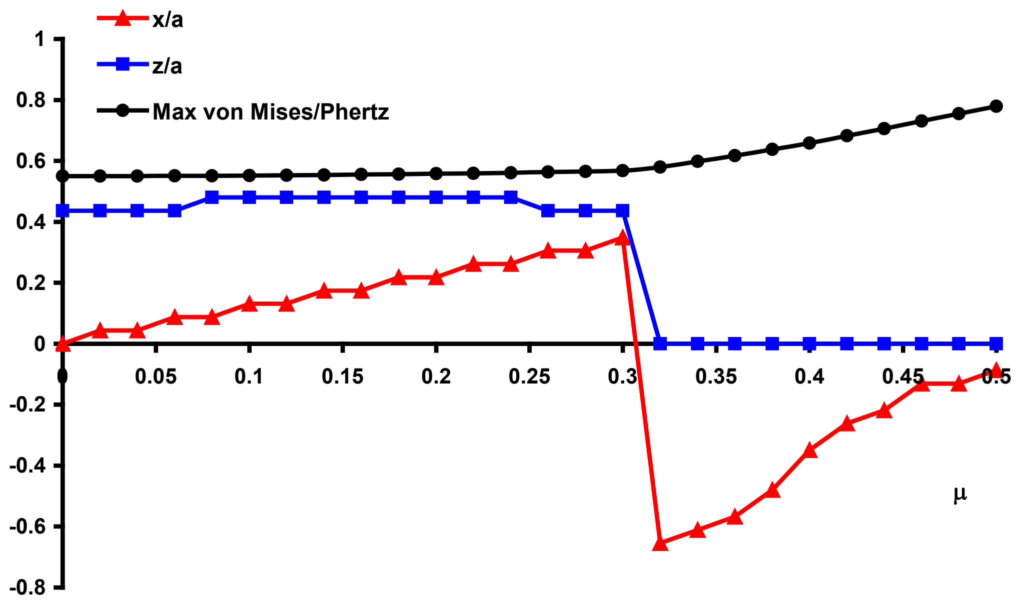

Fig.2.55 Value and location of the maximum von Mises stress (under load) versus the friction coefficient

Once again the maximum stress is found at the surface of the half-space when the friction coefficient exceeds 0.32, see Fig.2.55. In addition Fig.2.55 indicates that this point moves away from the contact center along the traction direction, see curve x/a versus μ, up to the critical value of 0.32 for which the maximum reaches the surface but in the opposite direction. The discontinuity in the plots of x/a and z/a versus the friction coefficient is explained by the fact that two local maxima are competing, one in the Hertzian region located slightly ahead of the contact center (i.e. $x > 0$, see left part of the curve), one closer to the surface and at the trailing edge of the contact. The maximum found near or at the surface is mostly related to the tangential load, whereas the maximum found in the Hertzian region is mostly related to the normal load. Further increase of the friction coefficient will finally move back that point to the contact center. More interesting is the residual stress profile found after unloading (Fig.2.54). One may observe two zones where residual stress is present, one at the Hertzian depth, another one at the surface of the contact including for frictionless contact. The same trend was previously observed by [Jac05] and [Kad06] for frictionless hemispherical contacts. The magnitude of the residual stress found at the surface increases with the friction coefficient to become higher than the one found at the Hertzian depth when the friction coefficient exceeds 0.3. In contrast it should be noticed a pronounced decrease of the maximum residual stress found at the Hertzian depth when the friction coefficient becomes higher than 0.4. It can be seen in Fig.2.54, that jagged lines are found for the lowest coefficients of friction. It is explained for two reasons. First the residual stress level is very low. Second the mesh is probably not fine enough to capture the very high gradient found at this location, as shown with a map view in Fig.2.56.

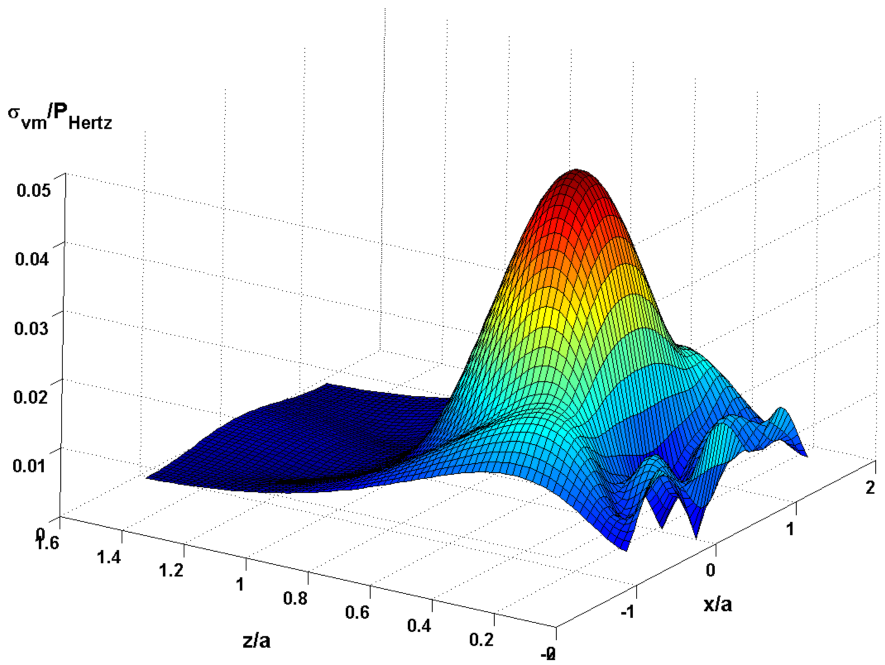

Fig.2.56 Residual Von Mises stress profile in the plane $y = 0$. Normal load 5 000 N, frictionless contact

A profile of the equivalent plastic strain is given in Fig.2.57 at the vertical of the contact center.

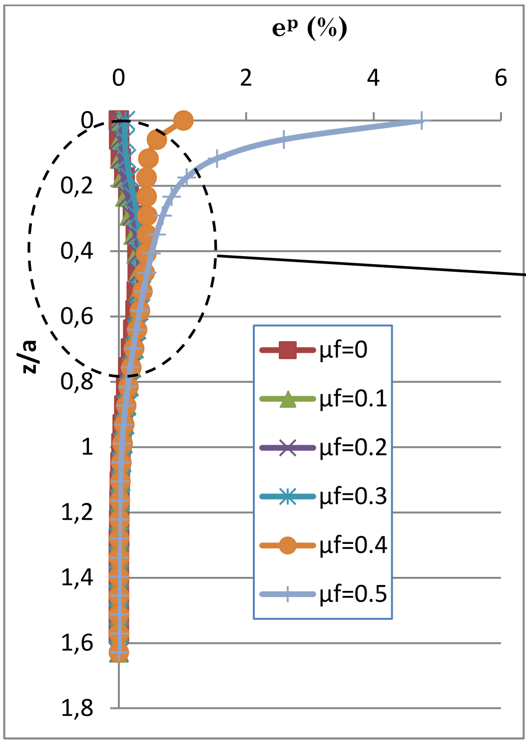

a) Regular view

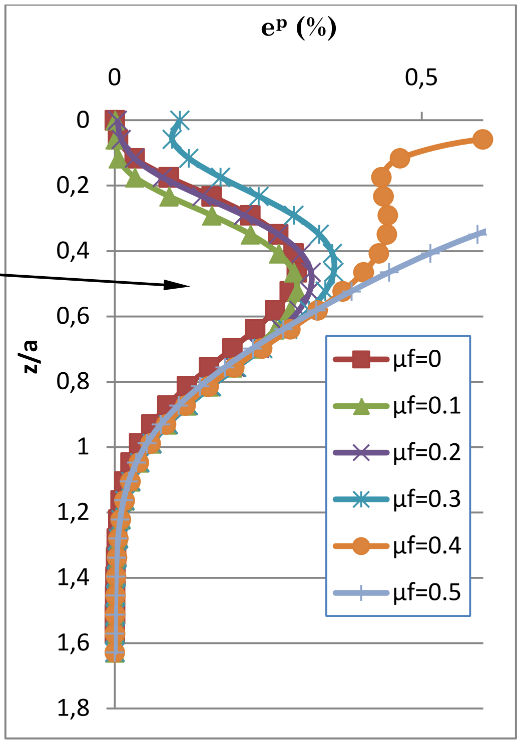

b) Zoom

Fig.2.57 Equivalent plastic strain profile versus depth at $x = y = 0$

One may observe that the plastic zone reaches the surface of the elastic-plastic body for a friction coefficient of approximately 0.2. Other simulations have shown that this critical friction coefficient is dependent of the normal load (or plasticity level), decreasing from 0.3 to 0 when the normal load increases from the value corresponding to first yielding. This result is of prime importance for wear or running-in modeling when the material removal is based on a strain threshold criterion (see Part 5).
When residual stresses are present it is sometime important to know if it corresponds to tensile or compressive zones. Typically for rolling contact fatigue applications it is well known that compressive residual stress will close the crack faces whereas tensile residual stress will favor the crack initiation and later its propagation. An interesting stress quantity for that identification is the hydrostatic pressure P_{hydro} after unloading, defined in

Eq.(2.165), where positive value means tensile zone and negative one compressive zone.

Fig.2.58 presents the residual hydrostatic pressure profile along depth at the contact center for frictionless contact and for various normal loads ranging from 1 000 to 5 000 N.

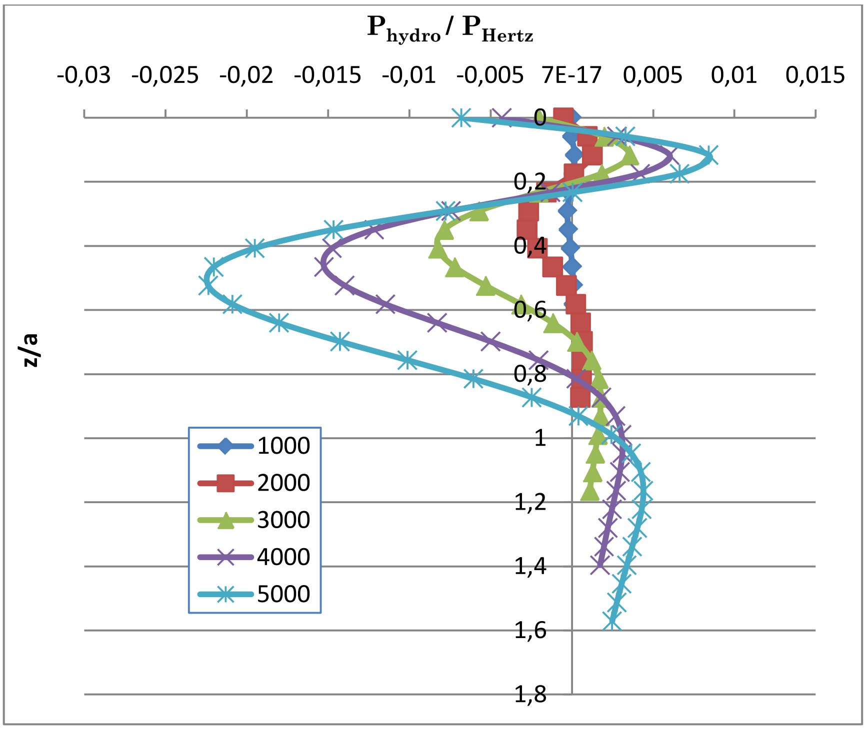

Fig.2.58 Hydrostatic pressure after unloading (residual), profile at $x = y = 0$, frictionless contact, for various normal load ranging from 1 000 to 5 000 N

An interesting result is the succession of compressive and tensile zones, compressive at the surface and at the Hertzian depth, tensile between the surface and the Hertzian depth and tensile below the Hertzian depth. This is coherent with the observation of Kogut and Etsion[Kog02] in term of plastic strains for axisymmetric contact. The amplitude of the variation of the hydrostatic pressure increases with the normal load. The tensile zone found between the surface and the Hertzian depth, sometimes called the "quiescent zone" for rough contact [Tal78], may explain why cracks initiated at the surface or at the Hertzian depth may propagate towards the Hertzian depth or towards the surface, respectively [Nel99]. In a similar manner Fig.2.59 presents the effect of surface traction on the same hydrostatic pressure profile after unloading for the highest normal load of 5 000 N.

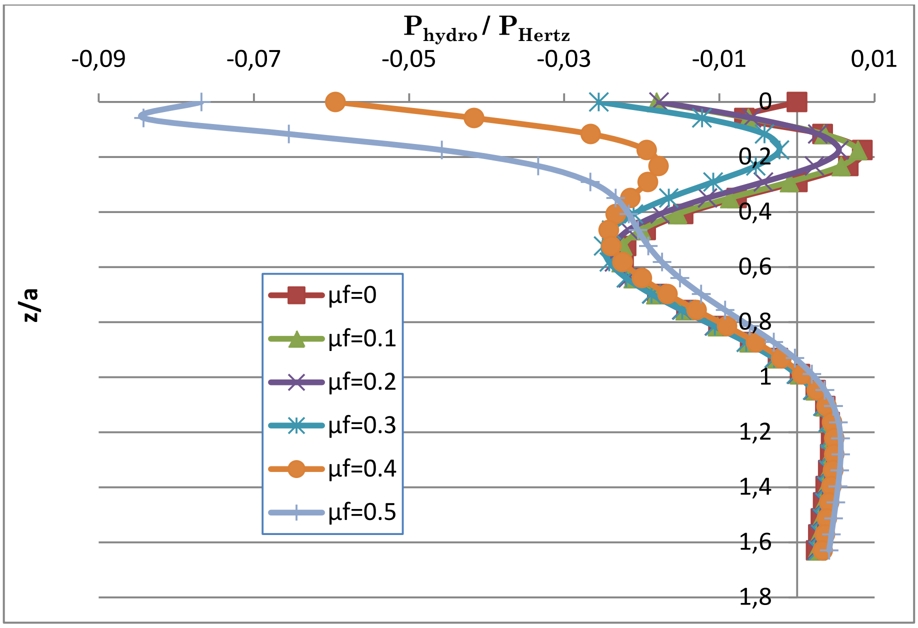

Fig.2.59 Hydrostatic pressure after unloading (residual), profile at $x = y = 0$, normal load of 5 000 N, for various friction coefficient ranging from 0 to 0.5

Similar comments as those given for Fig.2.53 and Fig.2.54 could be made about the two local maxima found at the surface and at the hertzian depth. It should be also noticed the effect of the friction coefficient on the stress state in the "quiescent zone", which becomes in compression above a critical friction coefficient found here between 0.2 and 0.3.

Part 3
Rolling and sliding contact

This part focuses on the way to consider rolling and sliding. The vertical contact is the first step for solving a transient case. Then hardening state and geometries are updated considering induced residual stresses and permanent print on the surface. Afterwards, some experimental and numerical results are presented, and influence of cycling, ellipticity ratio, hardening law and shear traction on the surface is studied

3.1 Modeling

3.1.1 Algorithm

The first step in transient contact calculation is to compute the static vertical contact (see Part 2). At the end of a global step of the algorithm (Fig.2.1), geometry and hardening state are to be updated. For the incremental vertical loading, the modified geometry and the hardening state are taken into consideration, and the load or the interference (rigid body displacement) is increased by its increment (see Fig.3.1).
For the rolling and sliding, after a global step, the geometry and the hardening state are shifted, and become the initial conditions for the new vertical contact (see Fig.3.2).
The way geometry and hardening state are updated is explain in the next section, when one body is considered elastic, while the counter body can be either elastic or elastic-plastic as soon as it has the same plastic properties (hardening law).

3.1.2 Update of the geometry, hardening and plastic strains

If one of the bodies is considered elastic, then at the end of the first contact calculation, one has the situation presented on the left hand side in Fig.3.3. For the next step, the residual displacement, the hardening state and the plastic strains are simply shifted from a value noted Δ and the new contact calculation can be processed, see right hand side in Fig.3.3. As a general comment, this "updating" is only possible with the assumption that both bodies are considered as half spaces, to be coherent with the SAM used and its limitations, see [Jac02] and [Bou05].
If both bodies are considered elastic-plastic, the pure rolling and the rolling plus sliding situations should be differentiated. For the pure rolling case, starting from the initial configuration given on the left hand side in Fig.3.4, the problem is very similar to the contact between an elastic body pressed against an elastic-plastic body, except that (i) the hardening state and the plastic strains are simply shifted for both bodies after each step; (ii) whe-

reas the residual displacement is doubled, as seen on the right hand side in Fig.3.4. The new contact calculation can then be processed.
For the (rolling plus) sliding contact the situation is more complicated. Starting from the initial configuration described on the left hand side in Fig.3.5, where the hardening state and the plastic strains are simply shifted, it is clear that the residual displacement history should be considered individually for each surface, as it can be seen on the right hand side in Fig.3.5.

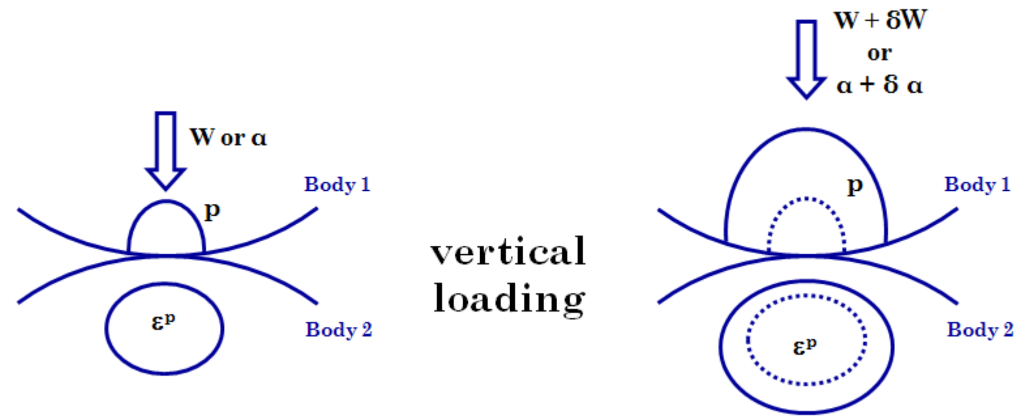

Fig.3.1 Updating of the geometry and the hardening state for incremental vertical loading

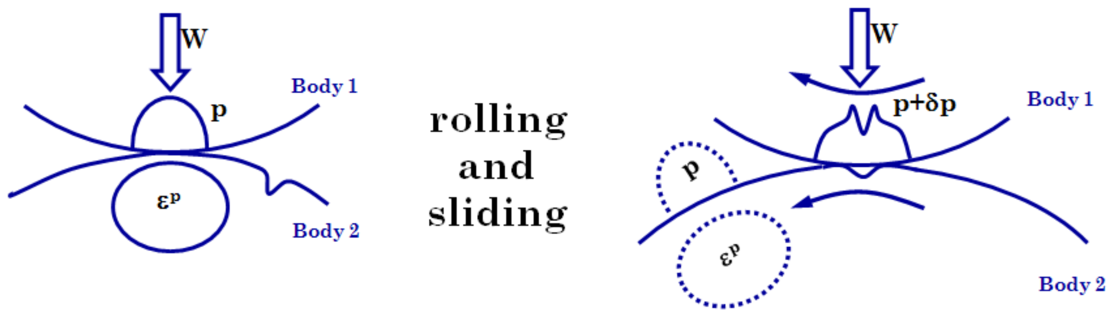

Fig.3.2 Updating of the geometry and the hardening state after vertical contact, for rolling and sliding loading

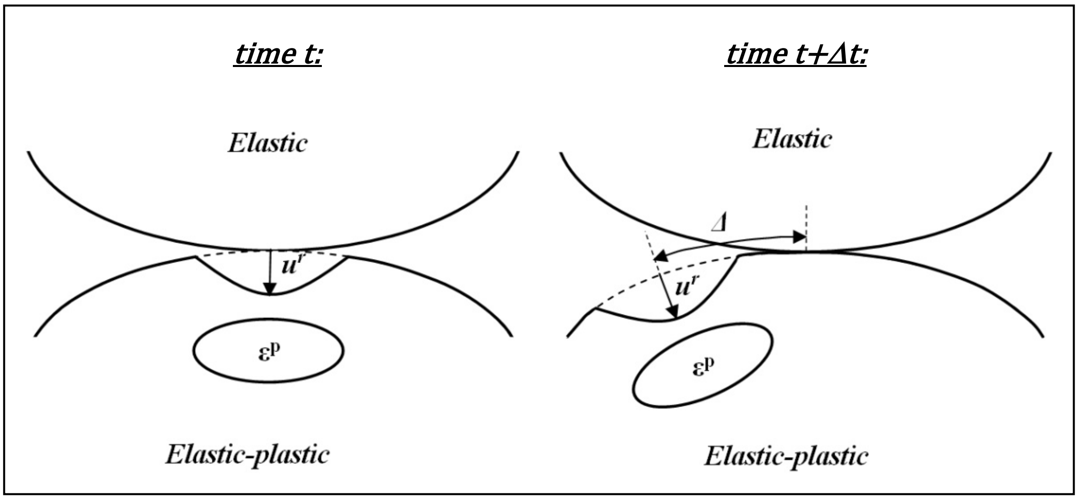

Fig.3.3 Updating at the end of the first loading step when one of the bodies is elastic

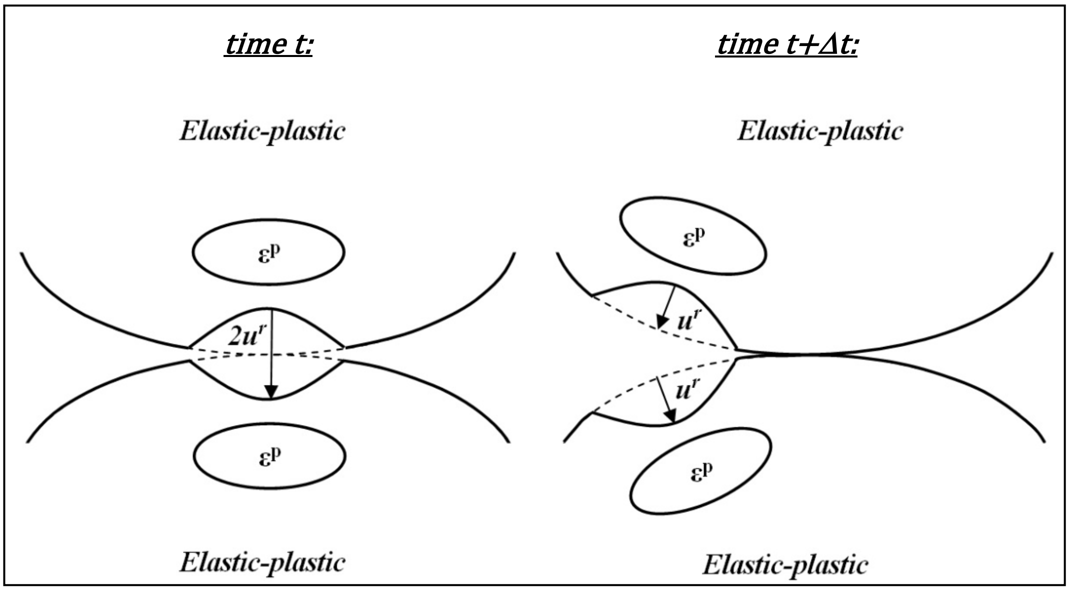

Fig.3.4 Updating at the end of the first loading step when both bodies are elastic-plastic. Case of pure rolling

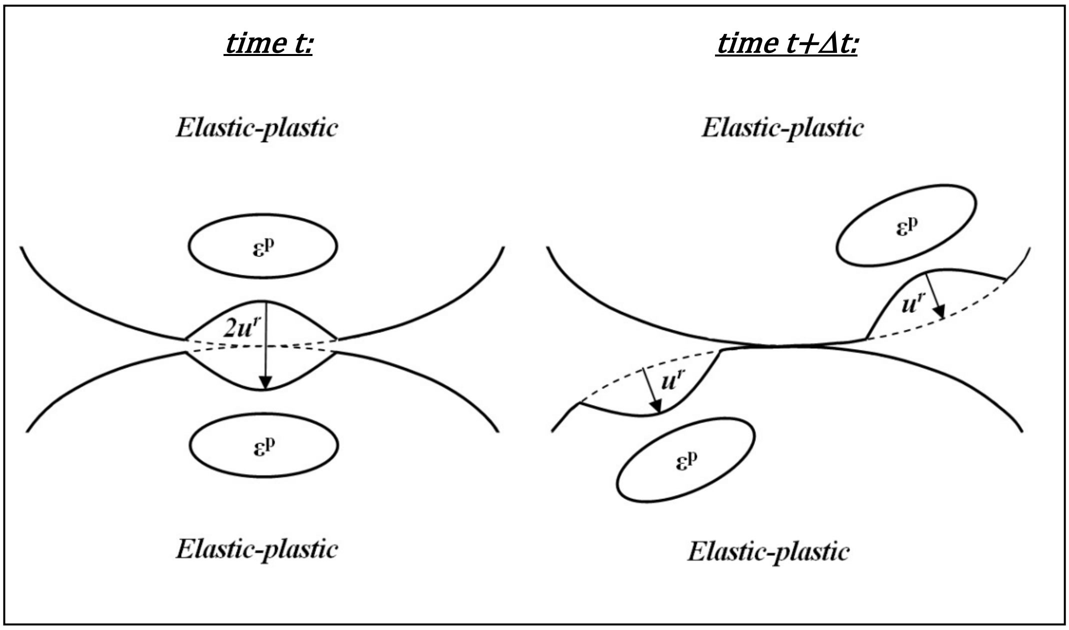

Fig.3.5 Updating at the end of the first loading step when both bodies are elastic-plastic. Case of rolling plus sliding contact.

3.2 Results

3.2.1 Rolling elastic-plastic contact

In this section, the rolling elastic-plastic contact is studied. First an experimental validation is presented for a thrust bearing. The effect of cycling is then investigated, as well as the effect of an ellipticity ratio, of the load, then some comparisons between the vertical and the rolling loading are made in terms of pressure, plastic strains and hardening law.

3.2.1.1 Experimental validations

In Jacq's PhD thesis [Jac01] a nitrated material has been studied, in order to test its fatigue life capacity during rolling contact with the presence of a surface defect (indent). In this section, the rolling of a ceramic ball on a flat made of steel is presented, in order to validate the computing code with an experimental test with a thrust bearing, shown in Fig.3.6.
The ball of diameter 9.525 mm is in ceramic, which is considered to behave elastically in the comparative simulation. Its Young's modulus is taken to be equal to 310 MPa, and Poisson ration is 0,29. The flat is made of steel, with a Young's modulus of 210 MPa, and a Poisson ration of 0,3. The Swift law is chosen for the hardening law, see Eq.(2.162). Since two different materials were tested, two set of parameters are considered. They are listed in Table 3.1.

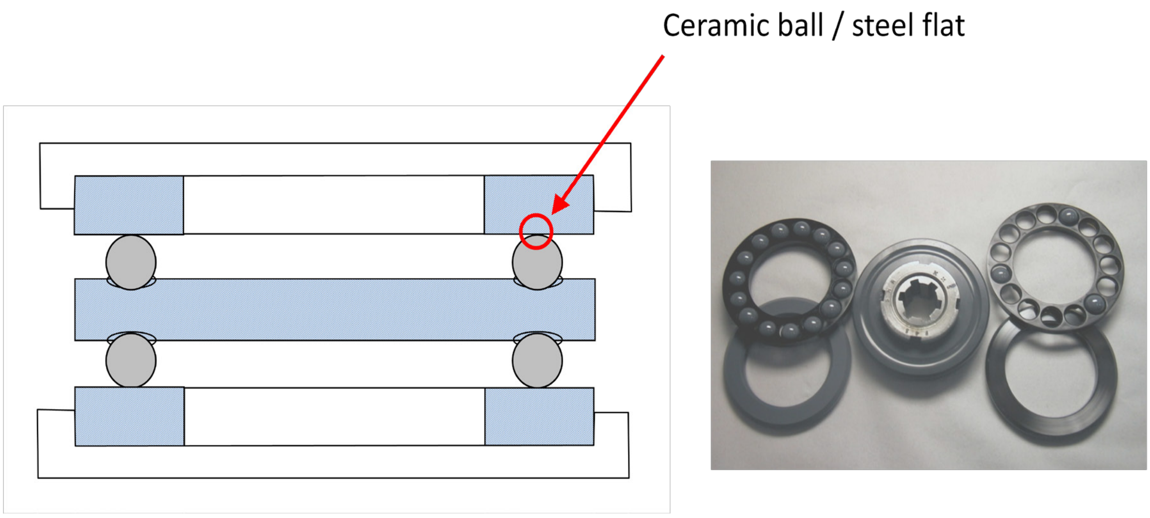

Fig.3.6 Tested thrust bearing. The contact between the ceramic ball and the steel flat is non-conformal

	B (MPa)	C (µdef)	n
M50	1280	4	0.095
AISI 52100	945	20	0.121

Table 3.1 Swift law parameters for the two tested materials

In the proposed experiment, three balls are set up, in order them not to roll on each other's path (see Fig.3.7). Then, applying a total load of 1380 N, each ball is loaded with 460 N, which corresponds to a Hertzian pressure of 4.2 GPa.

As shown in Fig.3.8 (transverse profiles for both tested materials) and Fig.3.9 (profile in the rolling direction for the second tested material), very good agreement is found between experimental data and numerical simulation.

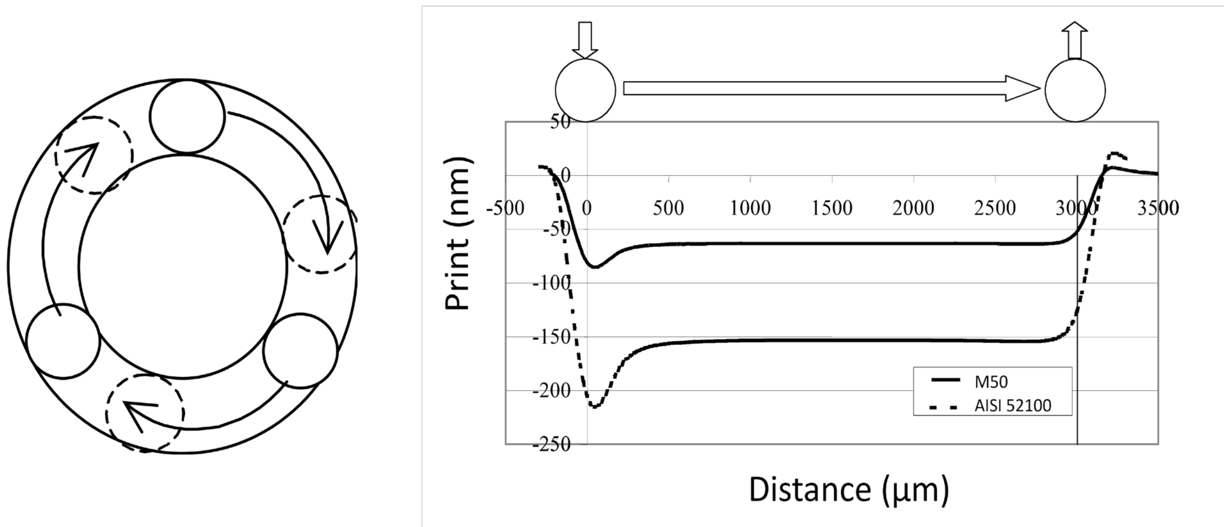

Fig.3.7 Modeling of the experiment using the computing code

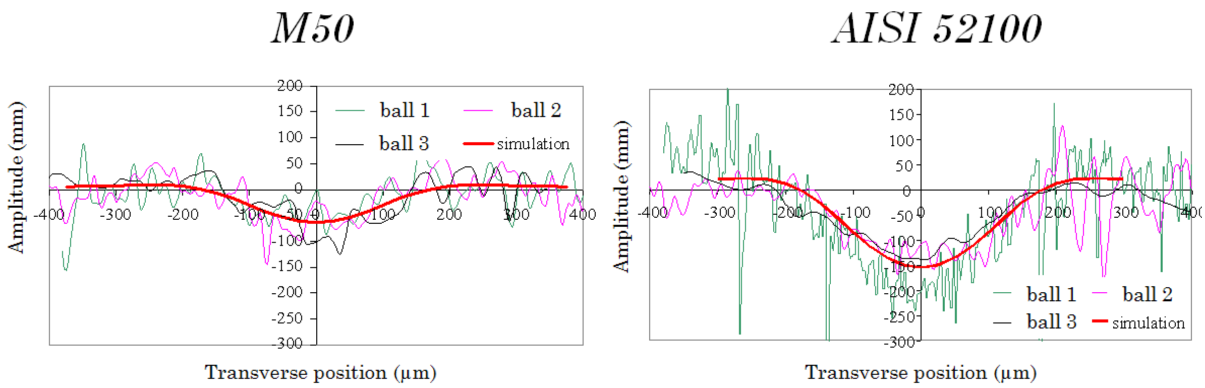

Fig.3.8 Resulting transverse profile, after rolling, for the three balls and the simulation

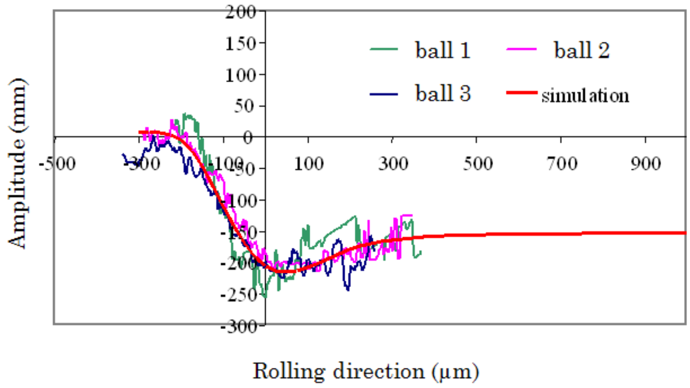

Fig.3.9 Resulting profile, after rolling, for the three balls and the simulation in the rolling direction

3.2.1.2 *Effect of cycling*

Let us now consider the effect of a cycling rolling load. To reach this aim, the same set of data as in the previous section is taken, considering the rolling of a ceramic ball on a flat made of steel. Again, the ceramic ball diameter is 9.525 mm and the steel plate is made of AISI 52100 bearing steel, but this time under a load of 5.7 GPa. The Young modulus and the Poisson ratio of the ceramic body are 310 GPa and 0.29, respectively, those of the steel plate are 210 GPa and 0.3. The contact radius for the reference simulation is $a =$

310 μm, and the mesh grid is here equal to 25 μm in both rolling and transverse directions. The parameters of the Swift law can be taken from Table 3.1.

The first step consists in determining the subsurface stress and strain states found under load or after unloading, as well as the shape of the permanent print found on the surface of the elastic-plastic flat.

Fig.3.10 shows the longitudinal profile (permanent) found after one loading cycle and after unloading with and without the rolling of the ball under contact pressure of 5.7 GPa (Hertz pressure i.e. elastic). The curve with square symbols corresponds to the axisymmetrical print found after unloading and without rolling. The curve with small dots presents the permanent print after a vertical loading, rolling of 4 mm from left to right maintaining the normal load constant, and unloading (vertical). Results are presented in a dimensionless form with the abscissa and ordinate normalized by the contact radius a.

It should be noted that the maximum depth is higher for the rolling load compare to the purely vertical loading/unloading. One may observe a decrease of the print depth after a transient period when the load is rolling, as previously observed by [Jac02]. This depth reaches an asymptotic value when rolling a few times the contact radius, which corresponds to a steady-state regime. Finally it could be observed a plastically deformed shoulder higher at the unloading position than at the initially loaded area.

A comparison of the surface displacement found at the center of the rolling track after unloading for the three first cycles and a rolling distance of 2 mm is shown in Fig.3.11 for the longitudinal profile and in Fig.3.12 for the transverse profile in the steady-state region. It can be observed that the permanent print reaches quickly a stabilized value after a very few cycles, i.e. 2 or 3 rolling loading cycles, which is due to the isotropic hardening model used in this study. The evolution between the first and second cycles is explained by the change of the surface conformity due to the plastic print which occurs mostly after one loading cycle.

An experimental profile in the stationary region is also given in Fig.3.12, and a very good agreement is found. Note that starting from Fig.3.12 all results presented in the transversal direction will be presented in the stationary region.

Fig.3.13 and Fig.3.14 show a cross-section view of the Von Mises stress field under load and after unloading, respectively, in a plane perpendicular to the rolling motion and in the steady-state region. The stress values, which are normalized by the elastic contact pressure P_{Hertz}, are given after two loading cycles. The loaded case (Fig.3.13) exhibits a maximum stress which is

lower than the elastic solution due to plasticity. More interesting is the distribution of the residual stress, see Fig.3.15. Three areas with high residual stress coexist, in fact three bands along the rolling direction, one at the Hertzian depth and the two others at the surface near the border of the contact but slightly inside the permanent print plotted in Fig.3.12. The residual stress distribution in the plane of symmetry ($y = 0$) is also given in Fig.3.15. It is not possible to know whether a region is in a tensile or compression state when using the Von Mises equivalent stress. It is why the hydrostatic stress also called the mean stress is now used to describe the residual stress. A positive value indicates that a region is in a tensile state, whilst a negative value corresponds to compression. It becomes clear from Fig.3.16 that the near surface area is in a tensile state after unloading, while subsurface plasticity induces compressive stresses at the Hertzian depth. This result is of prime interest for fatigue applications.
A cross-section view of the residual hydrostatic pressure is presented in Fig.3.16. Conversely to Fig.3.14 which corresponds to the Von Mises stress it is now observed a tensile zone lying on the surface, with two local maxima on both side of the rolling track. This peculiar feature is of prime interest for rolling contact fatigue since these tensile areas may favor the initiation and propagation of surface or near surface cracks due to surface inhomogeneities – such as embedded inclusions – or geometrical defects – such as grinding furrows or debris denting.
The distribution of the equivalent plastic strain in the plane $y = 0$ is given in Fig.3.17 for a rolling of 4 mm from the left to the right and after two loading cycles. One may notice a maximum value of approximately 0.9% at the Hertzian depth.

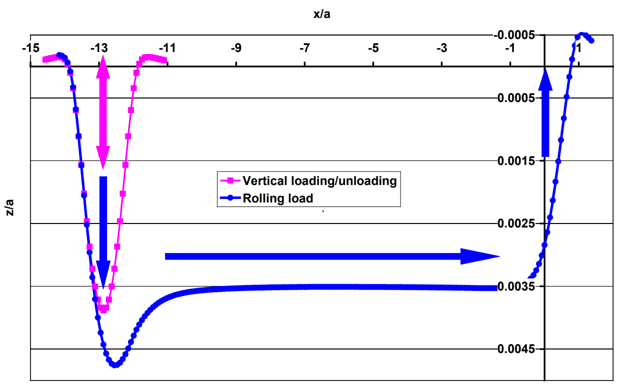

Fig.3.10 Comparison of a vertical loading/unloading with and without rolling (k = 1 – P_{Hertz} = 5.7 GPa – ceramic ball (elastic)/flat 52100 (elastic-plastic) surface, after a single cycle, rolling distance of 4 mm).

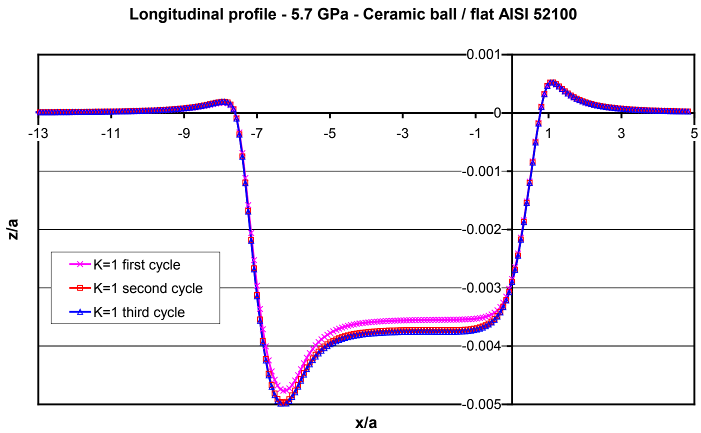

Fig.3.11 Surface displacement at the center of the rolling track after unloading (k = 1 – P_{Hertz} = 5.7 GPa – ceramic ball (elastic)/flat 52100 (elastic-plastic) surface, after 1, 2 and 3 cycles, rolling distance of 2 mm).

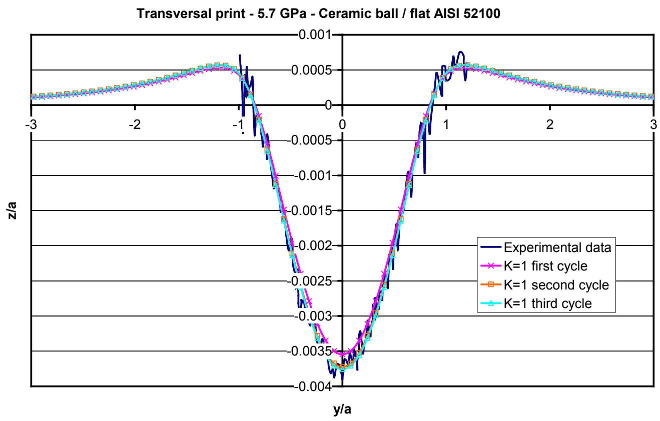

Fig.3.12 Transverse surface profile after unloading (k = 1 – P_{Hertz} = 5.7 GPa – ceramic ball (elastic)/flat 52100 (elastic-plastic) surface, after 1, 2 and 3 cycles).

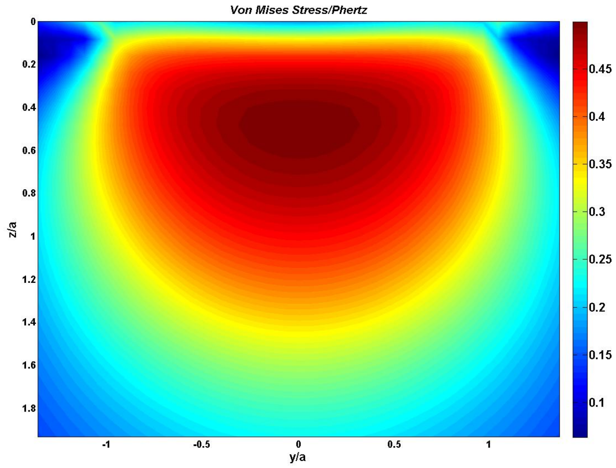

Fig.3.13 Cross-section view of the Von Mises stress under load in the steady-state region (k = 1 – P_{Hertz} = 5.7 GPa – ceramic ball (elastic)/flat 52100 (elastic-plastic) surface, after the second loading cycle).

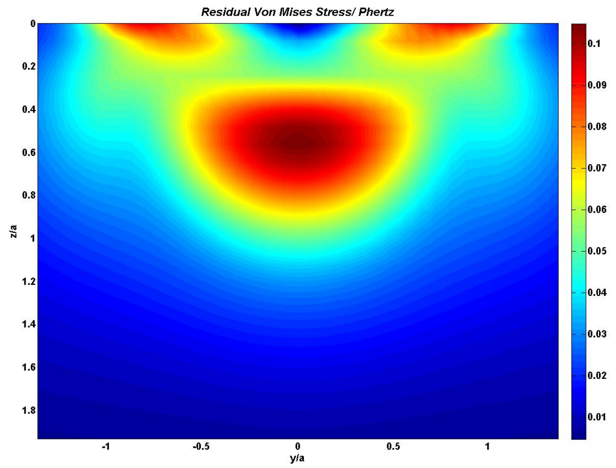

Fig.3.14 Cross-section view of the Von Mises stress after unloading (residual stress) in the steady-state region (k = 1 – P_{Hertz} = 5.7 GPa – ceramic ball (elastic)/flat 52100 (elastic-plastic) surface, after the second loading cycle).

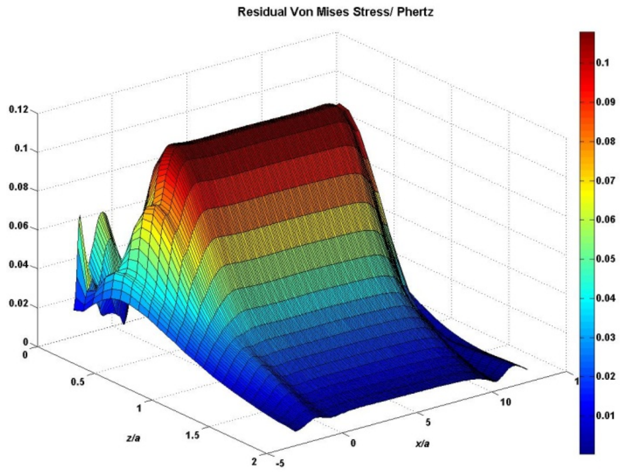

Fig.3.15 Distribution of the residual stress in the plane y=0 (k = 1 – P_{Hertz} = 5.7 GPa – ceramic ball (elastic)/flat 52100 (elastic-plastic) surface, after the second loading cycle).

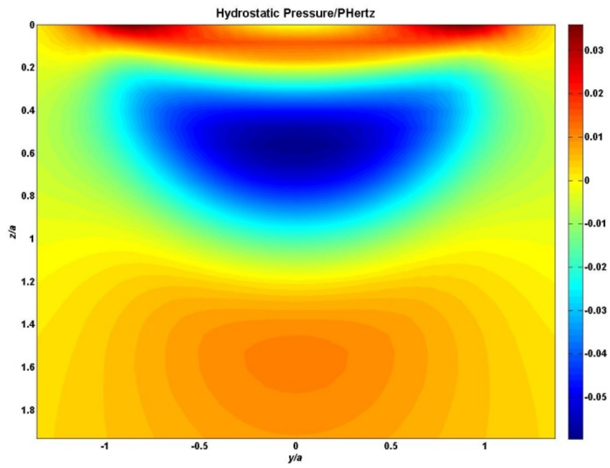

Fig.3.16 Cross-section view of the hydrostatic pressure after unloading (residual stress) in steady-state region (k = 1 – P_{Hertz} = 5.7 GPa – ceramic ball (elastic)/flat 52100 (elastic-plastic) surface, after the second loading cycle).

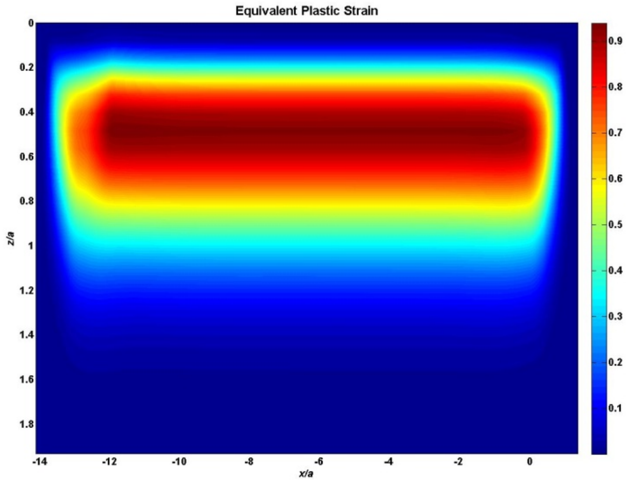

Fig.3.17 Isovalues of the equivalent plastic strain (in %) in the plane y=0 (k = 1 – P_{Hertz} = 5.7 GPa – ceramic ball (elastic)/flat 52100 (elastic-plastic) surface, after the second loading cycle).

3.2.1.3 Effect of ellipticity ratio

Some trends when the ellipticity ratio k increases up to 16 are now presented to give more realistic results for rolling bearing applications. As in ball bearings the elliptical contact is elongated in the direction perpendicular to the rolling movement. In all simulations the grid size is kept equal to 25 µm along the rolling direction, but is multiplied by the ellipticity ratio in the transversal direction (i.e. $\Delta y = k \times 25$ µm). The distance of rolling is 4 mm, i.e. 12.9 times the semi-minor axis of the contact, which is required to reach the steady-state regime for high ellipticity ratios.

As in the previous section all results will be given in a dimensionless form except for the equivalent plastic strain which is given in percent, i.e. the coordinates are normalized by the contact radius of the reference test ($a = 310$ µm), and the stresses by the Hertzian pressure (5.7 GPa). Again the cross-section views correspond to a transversal cut at an abscissa in the steady-state region i.e. far from the loading and unloading points.

The geometry of the elastic body leading to an elliptical contact of various ellipticity ratios is summarized in Table 3.2. It could be observed that the radius ratio $R_y/R_x = 77.88$ produces a semi-major axis of the contact ellipse

16 times greater than the semi-minor axis. Meantime the normal load should be multiplied by the ellipticity ratio to keep the Hertzian contact pressure constant. Note that the contact dimensions and normal load indicated in Table 1 correspond to a contact pressure of 5.7 GPa as elastic solution (Hertz) which indeed differs from the elastic-plastic solution.

k=c/a	Ry/Rx	Ry (mm)	c (mm)	W (N)
1	1	4.7625	0.310763	1152.9
2	2.97069	14.1479	0.621526	2305.8
4	8.82498	42.0290	1.243052	4611.6
8	26.21624	124.8549	2.486104	9223.2
16	77.88023	370.9046	4.972208	18446.4

Table 3.2 Effect of the ellipticity ratio k=c/a on the radius of the elastic body and subsequently on the normal load to kept the Hertzian contact pressure equals to 5.7 GPa.

Fig.3.18 and Fig.3.19 present a longitudinal and transversal view of the permanent print found after the first and the second cycles for different ellipticity ratios. It is interesting to note that, despite the same maximum contact pressure of 5.7 GPa, the print depth decreases when the ellipticity ratio increases (Fig.3.18) whereas its width increases (Fig.3.19). Another interesting feature is the formation of a material pile-up in front of the unloading point and on each side of the rolling track. For k=1 the maximum height is found on each side of the rolling track, the shoulder ahead of the track at the unloading position (Fig.3.18) being slightly lower than on the lateral sides. Conversely at higher ellipticity ratios one may observe that the height of the shoulder found in front of the rolling track increases significantly (Fig.3.19) whereas it decreases besides the rolling track. It should be also noticed that the longitudinal print found for k=16 is close to the line contact solution.
The effect of the ellipticity ratio on the steady-state contact pressure distribution is given in Fig.3.20. A comparison with the elastic solution shows a more pronounced decrease of the maximum elastic-plastic contact pressure when increasing the ellipticity ratio, until an asymptotic solution corresponding to the line contact solution. More surprising is the associated profile for the equivalent plastic strain, see Fig.3.21, which indicates a decrease of the maximum of the equivalent plastic strain found at the Hertzian depth when the ellipticity ratio is increasing. The depth at which this maximum is located is also increasing with k ratio which is in agreement with the elastic theory, i.e. $0.48 \times a$ for circular point contact and $0.8 \times a$ for line contact. Final-

ly the flattening of the contact pressure distribution when increasing the ellipticity ratio could be attributed to the extend of the plastic zone in depth, as seen in Fig.3.21 despite a lower plasticity level (denoted by the maximum value of the equivalent plastic strain).
Fig.3.22 to Fig.3.24 describe the stress profiles found below a point located in the center of rolling track and in the steady-state region. The Von Mises stress distribution is first given under load in Fig.3.22, then after unloading in Fig.3.23. One may observe in Fig.3.24 a decrease with the ellipticity ratio of the maximum stress found under loading, along with an increase of the depth at which the maximum value is found, in agreement with the trends for the equivalent plastic strain (Fig.3.21). The residual Von Mises stress plotted in Fig.3.23 shows a high level of residual stress, up to 10 percent of the Hertz pressure for k=1 i.e. 570 MPa. It could be also observe almost no difference between the stress state after the first and the second cycles. A convenient way to state whether a region is in tensile or compressive state is to plot the hydrostatic pressure, as in Fig.3.24. It becomes clear that the stress state within the depth is a succession of tensile, compressive and tensile regions i.e. compressive at the Hertzian depth and tensile elsewhere including at the surface. It should be noted that, coming back to Fig.3.16, the highest level of tensile stress found at the surface are located on each side of the rolling track and not in the plane of symmetry.

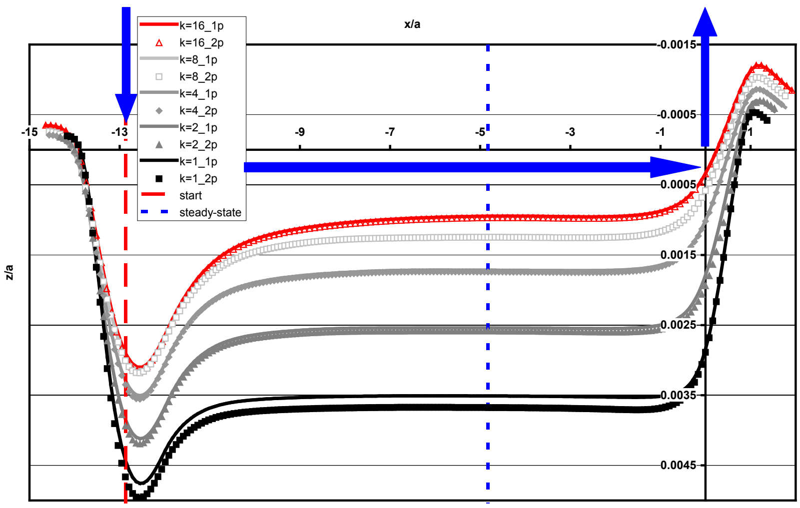

Fig.3.18 Surface displacement at the center of the rolling track after unloading for various ellipticity ratios and after 1 and 2 cycles. (P_{Hertz} = 5.7 GPa – ceramic ellipsoid (elastic)/flat 52100 (elastic-plastic) surface). Loading, rolling and unloading are represented by the thick arrows.

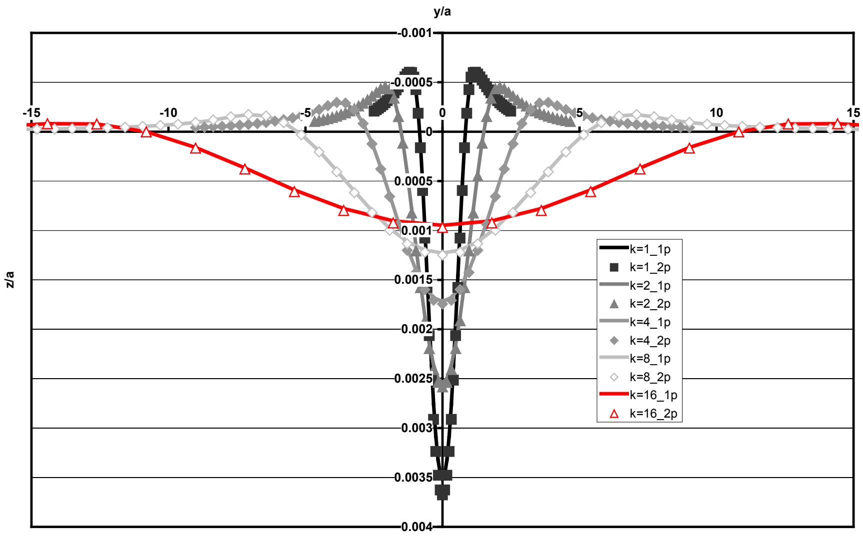

Fig.3.19 Transverse surface profile after unloading for various ellipticity ratios and after 1 and 2 cycles. Profiles taken in the steady-state region. (P_{Hertz} = 5.7 GPa – ceramic ellipsoid (elastic)/flat 52100 (elastic-plastic) surface).

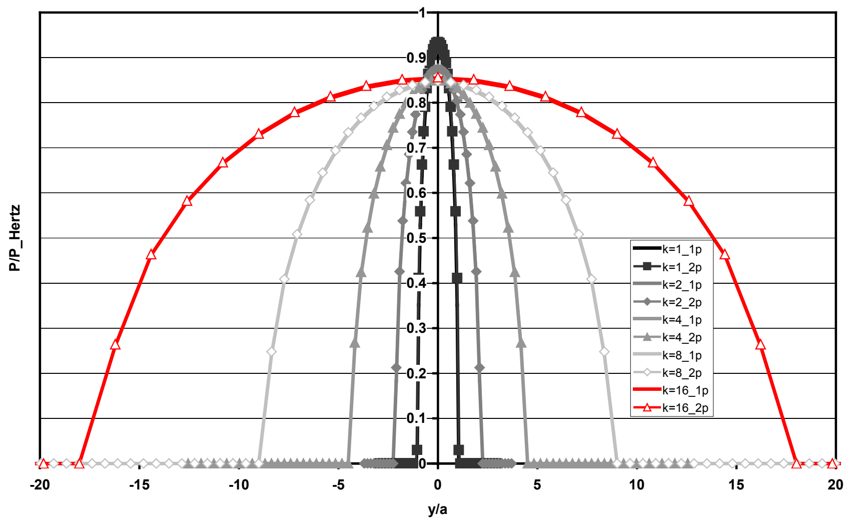

Fig.3.20 Contact pressure distribution found in the steady-state region for various ellipticity ratios and after the 2nd cycle. (P_{Hertz} = 5.7 GPa – ceramic ellipsoid (elastic)/flat 52100 (elastic-plastic) surface).

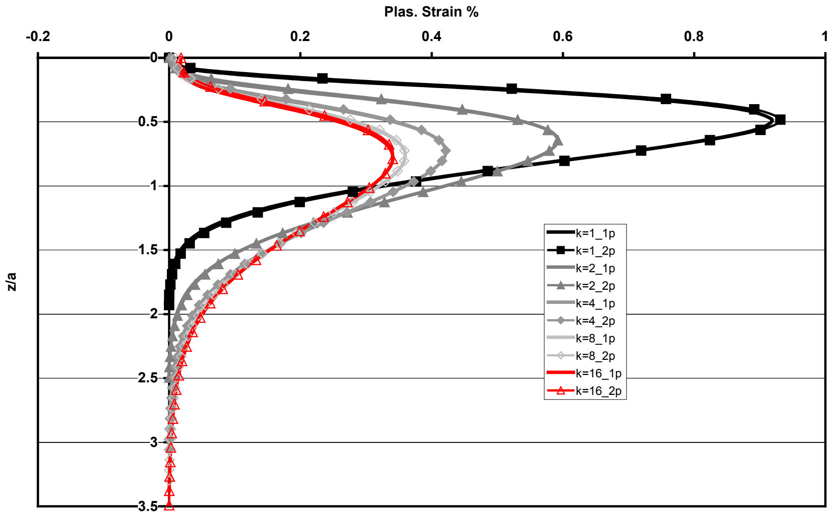

Fig.3.21 Profile of the equivalent plastic strain found in the center of the track and in the steady-state region for various ellipticity ratios and after 1 and 2 cycles. (P_{Hertz} = 5.7 GPa – ceramic ellipsoid (elastic)/flat 52100 (elastic-plastic) surface).

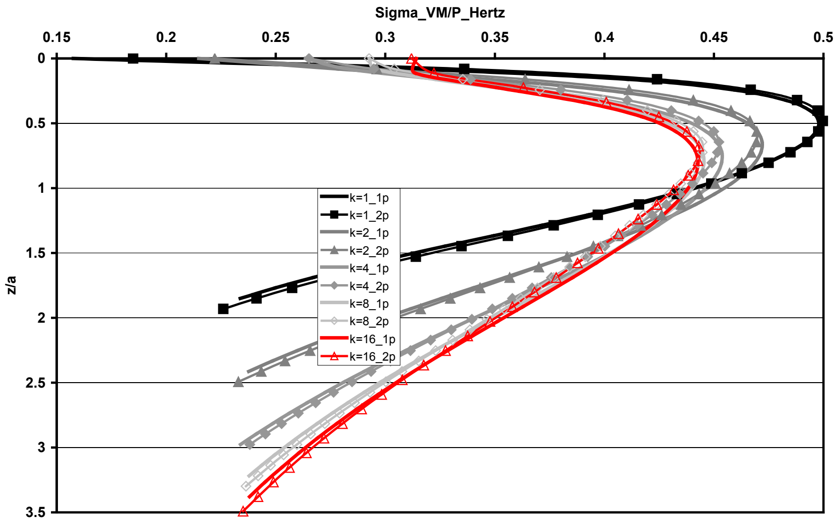

Fig.3.22 Profile of the Von Mises stress found under loading in the center of the track and in the steady-state region for various ellipticity ratios and after 1 and 2 cycles. (P_{Hertz} = 5.7 GPa – ceramic ellipsoid (elastic)/flat 52100 (elastic-plastic) surface).

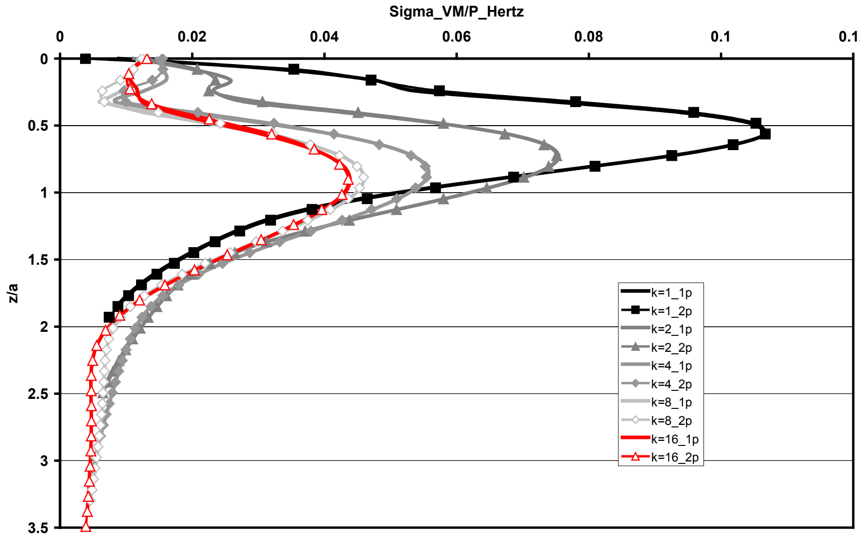

Fig.3.23 Profile of the residual Von Mises stress found after unloading in the center of the track and in the steady-state region for various ellipticity ratios and after 1 and 2 cycles. (P_{Hertz} = 5.7 GPa – ceramic ellipsoid (elastic)/flat 52100 (elastic-plastic) surface).

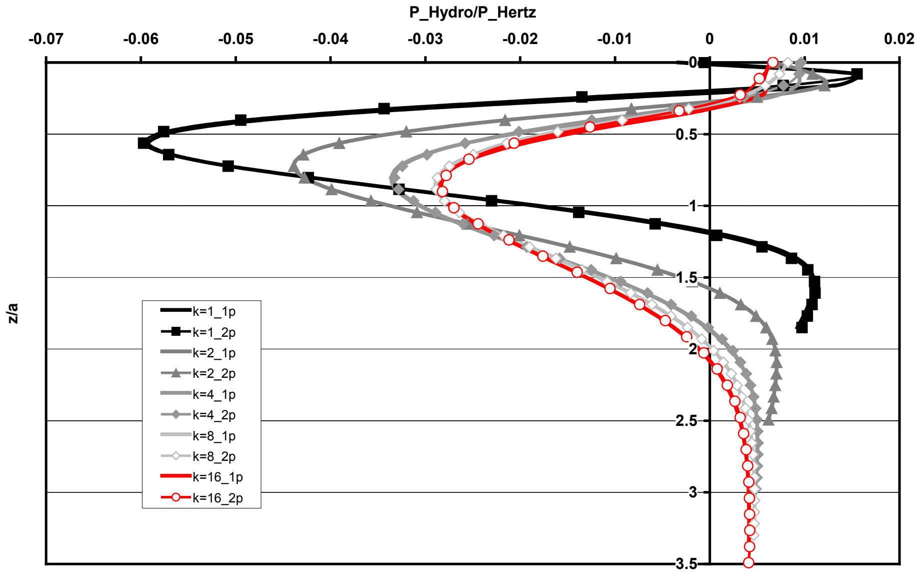

Fig.3.24 Hydrostatic pressure found after unloading in the center of the track and in the steady-state region for various ellipticity ratios and after 1 and 2 cycles. (P_{Hertz} = 5.7 GPa – ceramic ellipsoid (elastic)/flat 52100 (elastic-plastic) surface).

3.2.1.4 *Effect of normal load*

The effect of the maximum contact pressure – ranging from 4.2 to 8 GPa – is now investigated. The corresponding normal load is given in Table 3.3. In the present simulations the ellipticity ratio k has been chosen equal to 8 which is a close value of what is found in ball bearings. In this section results are presented with engineering values, i.e. distances in μm and stress in MPa, since both the contact ellipse and the maximum pressure are varying.

k=c/a	W (N)	Po (GPa)	a (μm)
8	3689.8	4.2	229.0
8	9223.2	5.7	310.8
8	13677.2	6.5	354.4
8	25499	8.0	436.2

Table 3.3 Value of the normal load vs. the Hertzian contact pressure for k=8.

All results presented in this section correspond to a profile along a vertical line from a surface point located in the center of the rolling track and in the steady-state region. The equivalent plastic strain profile is first given, see Fig.3.25, then the residual Von Mises stress (after unloading), Fig.3.26, and finally the hydrostatic pressure found after unloading, see Fig.3.27. It is clear from Fig.3.27 that the maximum strain found at 4.2 GPa, i.e. 0.05% is far below the conventional yield strain defined at 0.2%. Higher contact pressures result in a significant level of plasticity corresponding to 0.4, 0.8 and 2.1% of plastic strain at 5.7, 6.5 and 8 GPa, respectively. The depth at which these maximum are found is also increasing with the load level, as predicted by the conventional elastic theory. Note that the plastic volume increases significantly with the load. Here the Von Mises stress profile under loading is close to the elastic solution since the plastic strain remains lower than 2.1% at the highest (for 8 GPa). More interesting is the level of residual stress, either the Von Mises stress (Fig.3.26) or the hydrostatic pressure (Fig.3.27), which exhibits high level of stress, i.e. 40, 253, 445 and 935 MPa for the equivalent Von Mises stress at 4.2, 5.7, 6.5 and 8 GPa, respectively. Fig.3.27 indicates that the combination of a high ellipticity ratio (k=8) with a high contact pressure (6.5 GPa or higher) results in the disap-

pearance of the tensile zone found at the surface for circular point contact. It leads to only two zones, one in compression from the surface to a depth approximately two times the Hertzian depth, followed by a tensile zone at higher depth. This mean stress varies from -390 to 180 MPa at 8 GPa.
Finally Fig.3.28 presents the permanent print found in the center of the track along the rolling direction for different normal loads. Note that coordinates x and z are given in a dimensionless form, i.e. divided by the semi-minor axis a found at 4.2 GPa (i.e. 310 μm). Note that the maximum depth is found for the maximum load (8 GPa) and corresponds to 6.93 μm near the starting point and 2.96 μm in the stationary region.

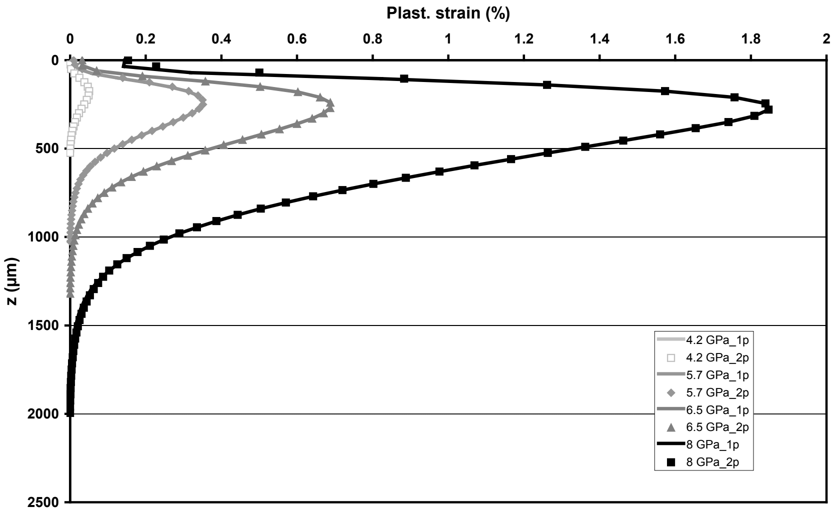

Fig.3.25 Profile of the equivalent plastic strain found in the center of the track and in the steady-state region for various normal loads and after 1 and 2 cycles. (k=8 – ceramic ellipsoid (elastic)/flat 52100 (elastic-plastic) surface).

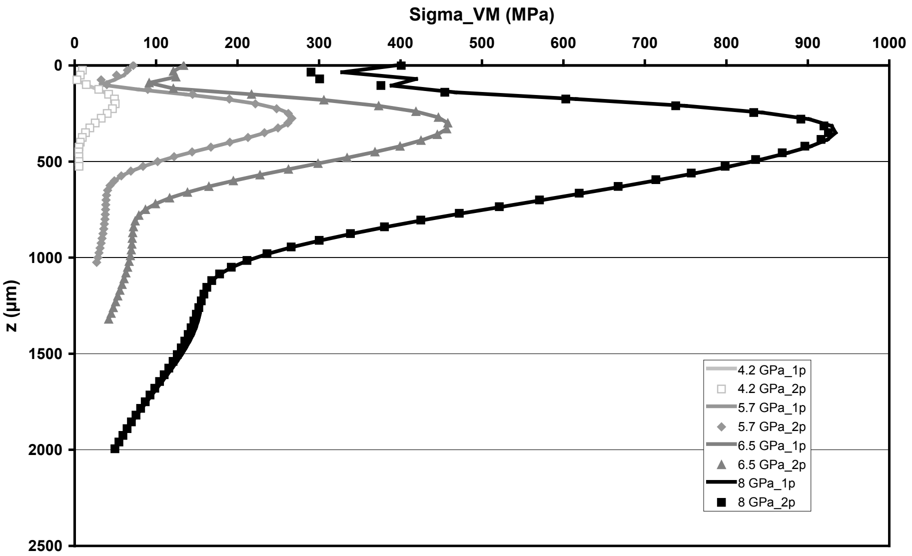

Fig.3.26 Profile of the Von Mises stress found after unloading in the center of the track and in the steady-state region for various normal loads
and after 1 and 2 cycles. (k=8 – ceramic ellipsoid (elastic)/flat 52100 (elastic-plastic) surface).

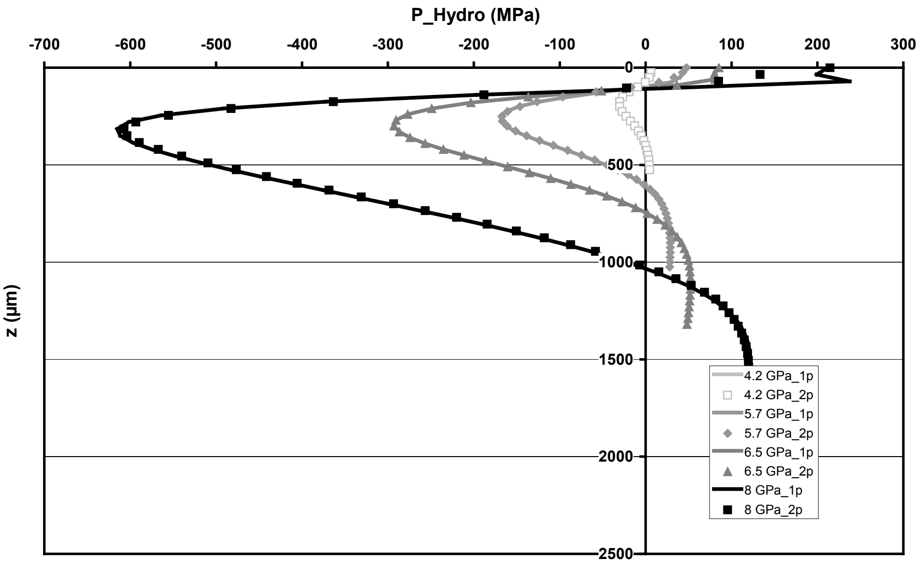

Fig.3.27 Profile of the hydrostatic pressure found after unloading in the center of the track and in the steady-state region for various normal loads
and after 1 and 2 cycles. (k=8 – ceramic ellipsoid (elastic)/flat 52100 (elastic-plastic) surface).

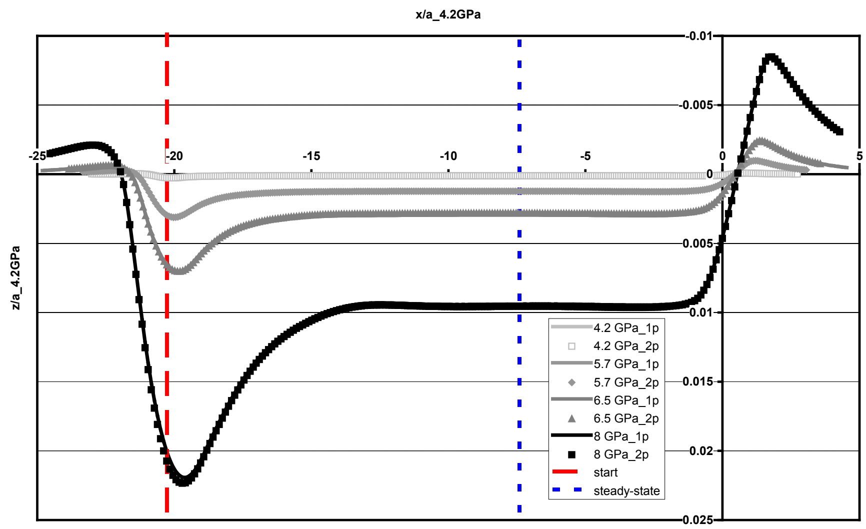

Fig.3.28 Displacement at the center of the rolling track after unloading for various normal loads and after 1 and 2 cycles. (k=8 – ceramic ellipsoid (elastic)/flat 52100 (elastic-plastic) surface).

3.2.2 Comparison between the vertical and the rolling loading

3.2.2.1 Effect of the ellipticity ratio and material behavior

An elliptical point contact has been investigated, for a stationary or a moving load, with at least one elastic-plastic body.
As it has been observed in sections 3.2.1.2 and 3.2.1.3, the chosen plastic model (isotropic hardening) permits to reach a stabilized solution after a few cycles only (only one cycle for vertical loading/unloading w/o rolling). The hardening law of the EP body is again described by the Swift's law, see Eq.(2.162), which presents the numerical advantage of being continuously derivable. Parameters describing the hardening of the AISI 52100 bearing steel are found in Table 3.1. Frictionless contact conditions are assumed

here. The load level investigated corresponds to an elastic contact pressure up to 8GPa, which keeps the material in the elastic shakedown regime
The indentation of an EP half space by a sphere and an ellipsoid (k=8) is analyzed, function of the load intensity, i.e. the Hertz pressure normalized by the uniaxial yield stress P_{Hertz}/σ_Y. The corresponding maximum contact pressure P_{max} and the equivalent plastic strain γ found at the Herztian depth are given in the left column of Fig.3.29, when the two bodies have similar EP behavior compared to the situation when one body behaves elastically whereas the counterface is EP. One may observe a pronounced reduction of the maximum contact pressure when considering two EP bodies compared to a purely elastic one against an EP one. The right column in Fig.3.29 presents results after 2 rolling loading cycles, taken in the steady-state region. Note that when rolling the ellipsoid is elongated in the direction transverse to the rolling direction. One may observe a significant increase of the maximum contact pressure and plastic strain compared to the stationary load.

The contact pressure and the plastic strain are then found lower when the 2 bodies are elastic-plastic, compared to the case when one remains elastic. Numerical results indicate also that, at a given load intensity, the maximum contact pressure and equivalent plastic strain are affected by the contact geometry and differ when the load is moving compared to the stationary situation.

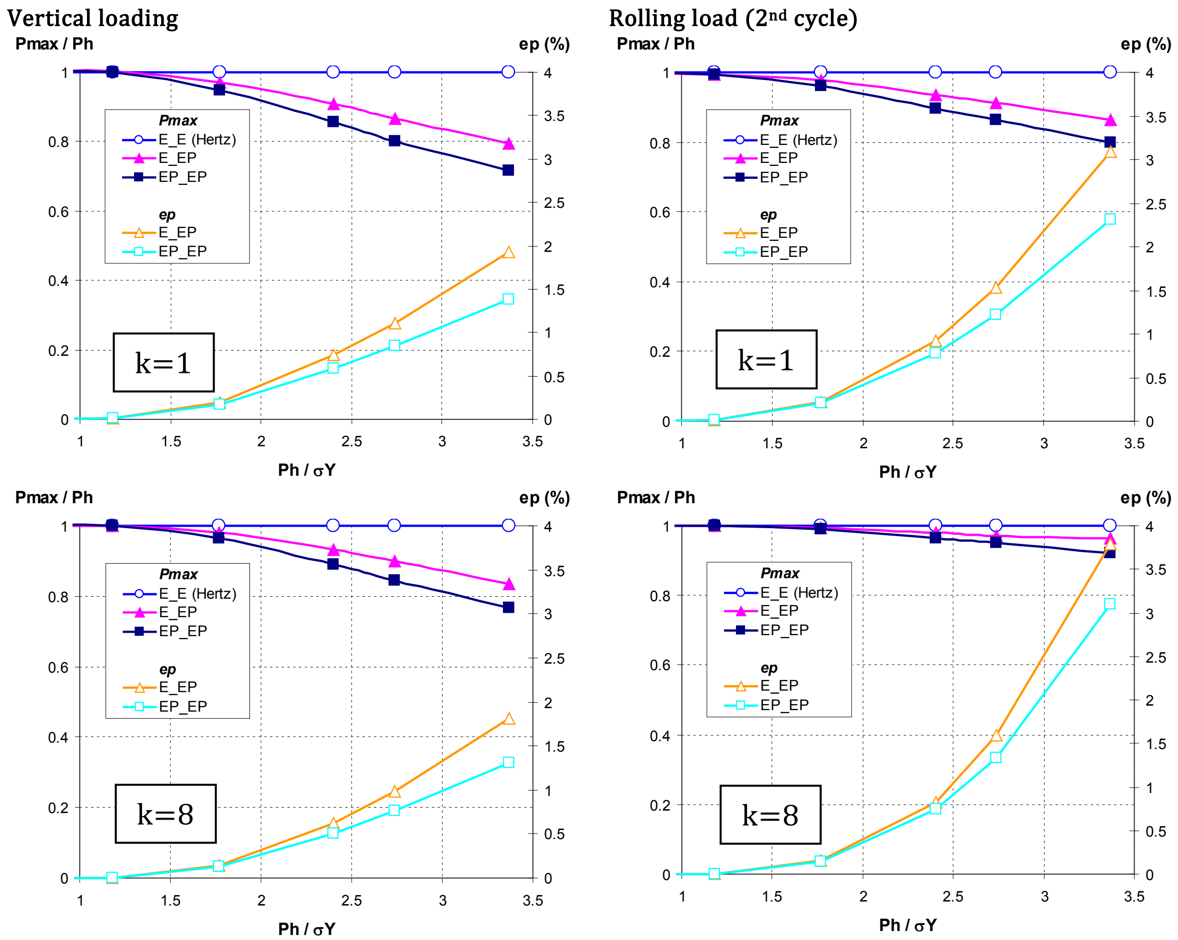

Fig.3.29 Maximum contact pressure P_{max} normalized by the elastic solution P_{Hertz} (Hertz pressure) and equivalent plastic strain e^p (%) vs. the load intensity P_h/σ_Y for a frictionless vertical loading (left column) and rolling load for the 2nd cycle (right). Acronyms E and EP mean Elastic and Elastic-Plastic behavior, respectively. The elastic solution (E_E) is the analytical solution of Hertz. Circular ($k = 1$) and elliptical ($k = 8$) point contact between two bodies made of 52100 bearing steel.

3.2.2.2 Effect of hardening law

The effect of different hardening laws is then studied, by setting the ratio of the tangent modulus to the Young's modulus ranging from 0 (perfect plasticity) to 0.8 (linear hardening), see Fig.3.30. Results in terms of pressure repartition are compared with the Hertzian case (elastic behaviour) for a contact between an elastic sphere (ceramic) and a steel flat (elastic-plastic) assuming an isotropic hardening. Fig.3.31 presents the results for a vertical loading simulating an indentation. When the bodies are rolled over and during the first cycle, it is possible to reach a stationary regime, after which the configuration remains identical. During this regime, it is noticed that the pressure repartition has a different shape and the maximum is greater than in the vertical case. Pressure repartition in the rolling direction is found to be non-symmetrical any longer, and the maximum is found on the side of the rolling direction, see Fig.3.32. Since the computation is three-dimensional, the pressure in the transverse direction is also shown in Fig.3.33. It is naturally noticed that the maximum pressure value is found at the centre of the contact in that direction, due to the symmetry of the problem.

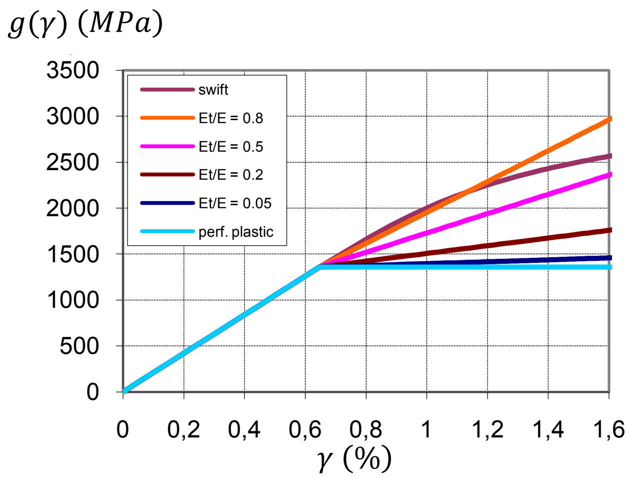

Fig.3.30 Hardening laws used. Evolution of the ratio E_t/E

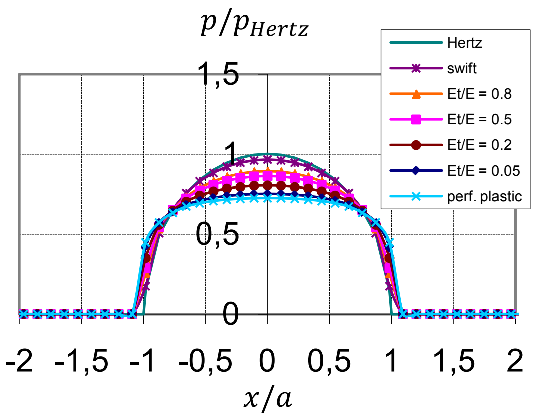

Fig.3.31 Pressure repartitions for the vertical loading

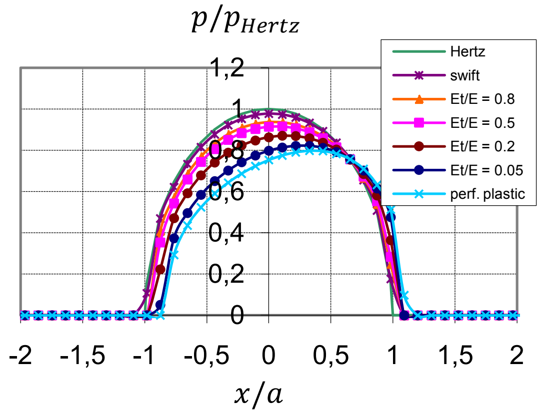

Fig.3.32 Pressure repartitions for the rolling loading – rolling direction

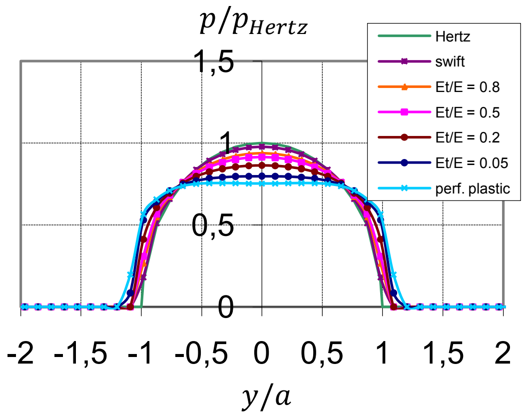

Fig.3.33 Pressure repartitions for the rolling loading – transverse direction

3.2.3 Transient thermal-elastic-plastic contact

With the developed computing code, it is possible to study a full transient thermo-elastic-plastic contact. Some simulations have been proceeded, in order to try to deal with grinding process, which is extremely important to model in machining processing. In all the presented simulations, the cutting tool diameter is 15mm and is considered adiabatic, while its material properties are $E = 210$ GPa for Young's modulus, $\nu = 0.3$ for Poisson ratio. It is considered to deform elastically, whereas the counter body, a steel flat is made of AISI 52100 material, with the same elastic properties, but considered to behave plastically following the swift law (see Eq.(2.162)) with parameter that can be found in Table 3.1. The applied load is 1500 N, which corresponds to a Hertzian pressure of 6.5 GPa, and a Hertzian contact radius of 332 μm.

Three cases are shown hereafter:

i) the transient continuous case in stationary regime, with a heat factor of 0.12m/s and a time of observation of 23ms (see Fig.3.34). The source is then static (nil relative speed), it can be for example a cutting tool rotating over its own axis, and this source is heating the counter body during 23ms

ii) the steady-state case in stationary regime, with again a heat factor of 0.12m/s but the time of observation is now set to infinity, i.e. the steady state is reached (see Fig.3.35)

iii) the transient instantaneous case with a moving source. Again the heat factor is set to 0.12m/s, but the source is now moving with an absolute speed of 0.95m/s, it can be a cutting tool which is displaced during the cutting procedure. Time of observation is set to 23m/s (see Fig.3.36)

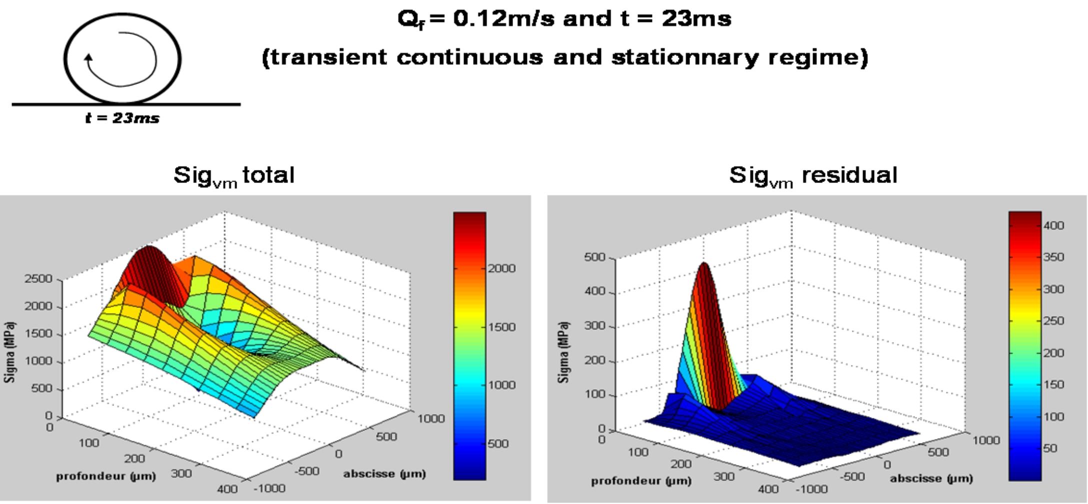

Fig.3.34 Transient continuous simulation. The source (cutting tool) is static

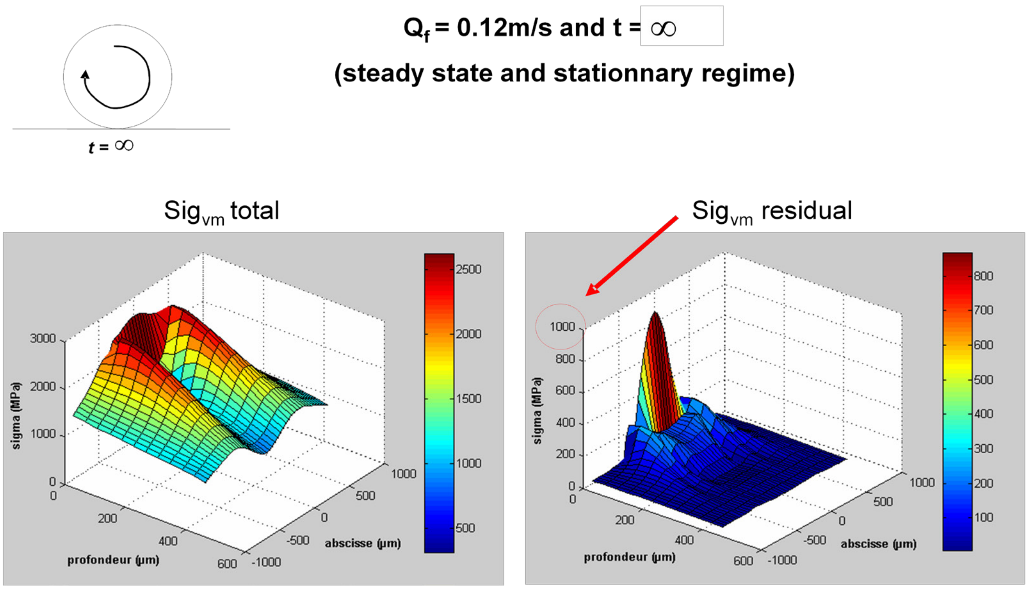

Fig.3.35 Steady-state simulation The source (cutting tool) is static

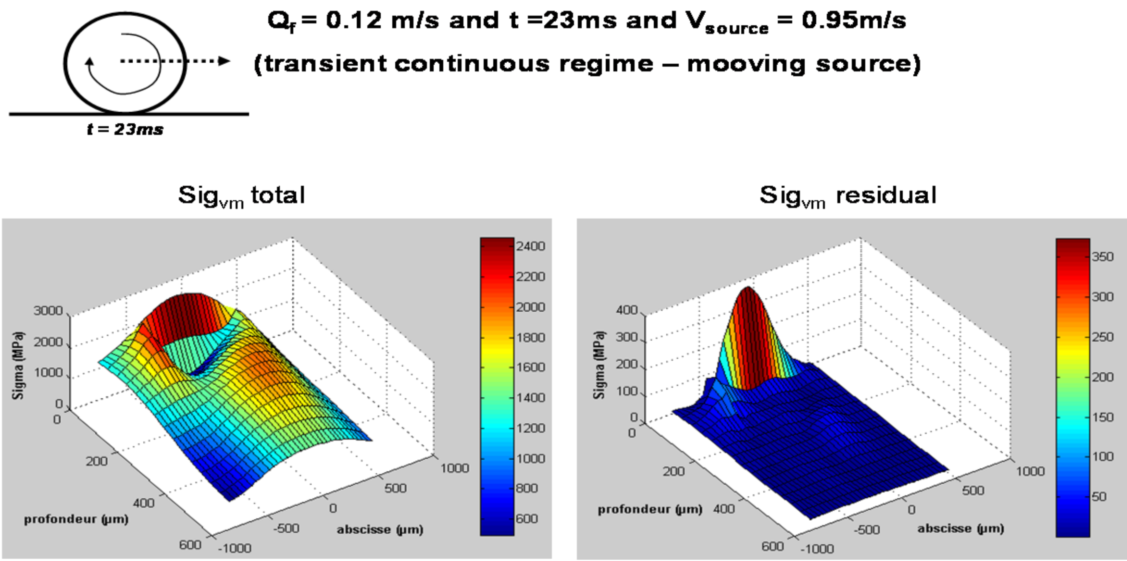

Fig.3.36 Transient instantaneous simulation. The source (cutting tool) is moving

Part 4
Development of a model for two elastic-plastic asperities tugging

In this part, the theory developed in previous sections is further improved in order to apply the computing code to the collision of two elastic-plastic asperities. The friction coefficient is neglected on purpose, in order to study the mechanical deformation of asperities only, during sliding process. First, the knowledge of the interference in the local reference has to be known, in order to compute the contact at each time step during motion. Then, the normal and the tangential forces are projected in the global reference in order to define an apparent friction coefficient. The way these are projected depends on the pile-up induced by permanent deformation of the surface. Then some results are given in the last section in terms of forces, net energy (energy loss during sliding process), friction coefficient, and residual displacements

4.1 Modeling

4.1.1 Sliding of two asperities

In the current incremental procedure, the normal contact is solved at every step. The geometry, the hardening state as well as the plastic strains are updated at the end of each step for each EP body. When the asperities are moving the geometry change includes the permanent deformation of the surface of the elastic-plastic bodies. Special care to the effects of sliding is given since it is a more complex problem than the pure rolling situation as discussed earlier (0).

The analysis of the contact between two asperities requires considering a relative velocity between the bearing surfaces. In addition when the tugging asperities bear only a small portion of the total load, it is clear that this transient contact will be better described by the dd-formulation (see section 2.2.4.1) than by the ld-formulation since both the subsequent localized normal and tangential loads will quickly change from zero to a maximum and then go back to zero (meaning no contact). A schematic view at the beginning of the collision is shown in Fig.4.1 when one of the asperities is being translated along the rolling/sliding direction relatively to the other one. For simplicity it is assumed that the center of the 2 colliding asperities in Fig.4.1 remains in the plane (XZ).

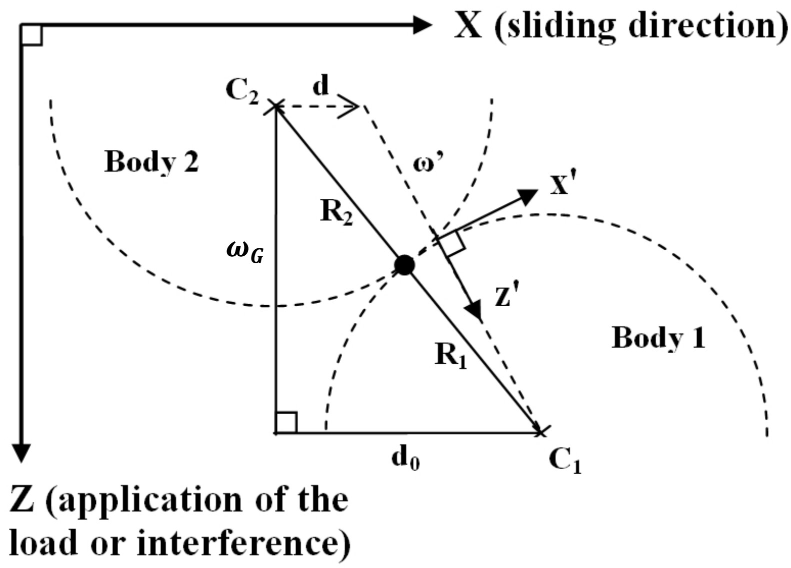

Fig.4.1 Schematic view of the tugging between two interfering asperities in rolling / sliding Definition of the Global (X,Z) and Local (x',z') refer.ences. Here the initial state when asperities start to tug each other is represented.

4.1.2 Calculation of the local interference

A global and a local references will be considered to model the transient contact during tugging, as shown Fig.4.1. The local reference (x', z') is linked to the plane of contact. A global interference is first applied in the global reference, by maintaining the global center separation, ω_G, along the Z-direction constant during tugging. Then one of the bodies is shifted of d in the perpendicular direction (X-direction). As a consequence, the local center separation, ω' along the z'-direction of the local reference will be different at every step of the computation.
The initial state is considered first. The global center separation ω_G is applied in Z-direction, and the two bodies are put in contact. If d_0 is the initial distance between the two centers C_1 and C_2 in X-direction, then the local center separation ω' in z'-direction can be expressed as a function of the global center separation ω_G, d_0 and d, the latter being the sliding distance in

X-direction, see Eq.(4.1), and d_0 the distance defined by Eq.(4.2). In the whole development, both radii R_1 and R_2 are equal to R_0.

$$\omega'^2 = {\omega_G}^2 + (d_0 - d)^2 \tag{4.1}$$

With:

$${d_0}^2 = (R_1 + R_2)^2 - {\omega_G}^2 = 2\,{R_0}^2 - {\omega_G}^2 \tag{4.2}$$

In this formulation, the fixed value is the shifting value Δ introduced in Fig.4.2, and corresponds to the same one than in Fig.3.3. As a consequence, it is required to express the sliding distance d as a function of Δ. At any time, if one of the bodies is displaced from a value δd, its surface makes an angle θ with the shifting direction, see Fig.4.2. It is then possible to write:

$$\delta d = 2\Delta \cdot \cos\theta \tag{4.3}$$

Considering the curvature of the bodies, a correction has to be made to the value δd. Denoting $\widehat{\Delta}$ the real shifted value, see Fig.4.3, and writing that:

$$\tan\alpha = \frac{\Delta}{\omega'_{i-1}/2} \tag{4.4}$$

ω'_{i-1} being the previous local center separation, δd can be corrected as follows:

$$\delta d = 2\widehat{\Delta} \cdot \cos\theta \tag{4.5}$$

With:

$$\widehat{\Delta} = (\omega'_{\mathrm{i-1}}/2) \cdot \alpha = (\omega'_{\mathrm{i-1}}/2) \cdot \tan^{-1}\left(\frac{\Delta}{\omega'_{i-1}/2}\right) \tag{4.6}$$

Then δd can be re-written as follows:

$$\delta d_{i-1} = \omega'_{\mathrm{i-1}} \cdot \tan^{-1}\left(\frac{\Delta}{\omega'_{i-1}/2}\right) \cdot \cos\theta_{i-1} \tag{4.7}$$

Now θ is determined, which is an unknown and varies with the sliding distance. Considering two consecutive states $i-1$ and i, see Fig.4.4, one can write:

$$\cos\theta_{i-1} = \frac{\omega_G}{\omega'_{i-1}} \tag{4.8}$$

Coupling Eq.(4.7) and Eq.(4.8), it yields:

$$\delta d_i = \omega_G \cdot \tan^{-1}\left(\frac{2\Delta}{\omega'_{i-1}}\right) \tag{4.9}$$

The last step in the determination of the sliding distance d is the summation of all the sliding distance increments, i.e.:

$$d_i = \sum_{k=1}^{i} \delta d_k \tag{4.10}$$

i being the current state. The explicit form of d_i is then:

$$d_i = \omega_G \cdot \sum_{k=0}^{i-1} \tan^{-1}\left(\frac{2\Delta}{\omega'_k}\right) \tag{4.11}$$

Finally, combining Eq.(4.1), Eq.(4.2) and Eq.(4.11), the local center separation can be re-written as follows, at every step of the computation:

$$\omega'_0 = (R_1 + R_2) = 2\,R_0 \tag{4.12}$$

$$i > 0: \quad \omega'_i = \left[{\omega_G}^2 + \left(\left[2\,{R_0}^2 - {\omega_G}^2\right]^{0.5} - \omega_G \cdot \sum_{k=0}^{i-1} \tan^{-1}\left(\frac{2\Delta}{\omega'_k}\right)\right)^2\right]^{0.5} \tag{4.13}$$

In order to relate the local center separation ω' to the interference (rigid body approach) ω used in the Semi-Analytical Code developed previously, one can write :

$$\omega_i = 2\,R_0 - \omega'_i \tag{4.14}$$

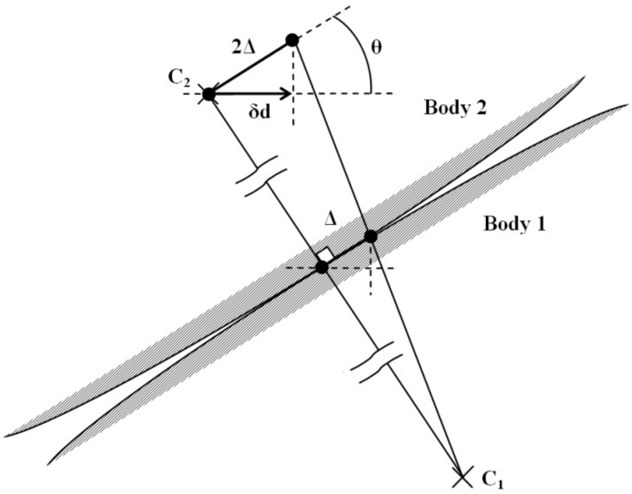

Fig.4.2 Displacement δd of body 2

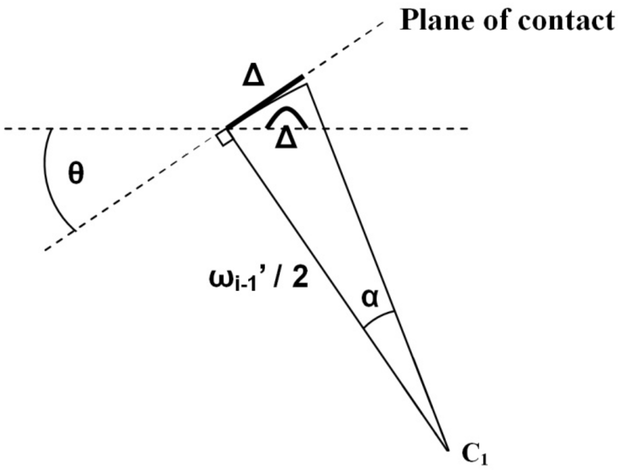

Fig.4.3 Correction of the term δd

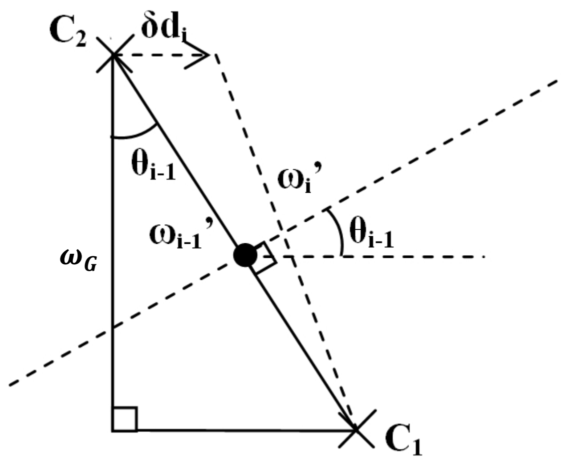

Fig.4.4 Representation of two consecutive states $i-1$ and i for the determination of θ_{i-1}

4.1.3 Forces calculation

The first part of this section deals with the force calculation that is projected in the global reference. Some correction term will be added in order to take into consideration what we refer as “pile-up” phenomenon. Finally, some results will be plotted concerning the tangential and normal forces found during the sliding phase, as well as the energy loss in the sliding contact, and the residual deformation after unloading at the end of the sliding process.

4.1.3.1 Normal and tangential forces (in the global reference)

At anytime during sliding, it is possible to calculate the pressure distribution resulting from the normal contact in the local reference. As a consequence, the tangential and the normal forces in the global reference can be calculated by integrating the pressures on the X and Y axes for the tangential forces, and on the Z-axis for the normal force, i.e.:

$$F_x = n \cdot a_x \cdot a_y \cdot \sum_{I_c} p \cdot \sin\theta \tag{4.15}$$

$$F_y = 0 \tag{4.16}$$

$$F_x = n \cdot a_x \cdot a_y \cdot \sum_{I_c} p \cdot \cos\theta \tag{4.17}$$

n being the number of nodes where the contact pressure is not nil, a_x and a_y the grid spacing in x' and y' direction respectively (local reference), and I_c the set of nodes where the pressure is not nil. As an example, Fig.4.5 shows how to obtain the projected forces at a point of the contact surface. Due to the symmetry of the problem, the projected force F_Y on the Y-axis is nil.

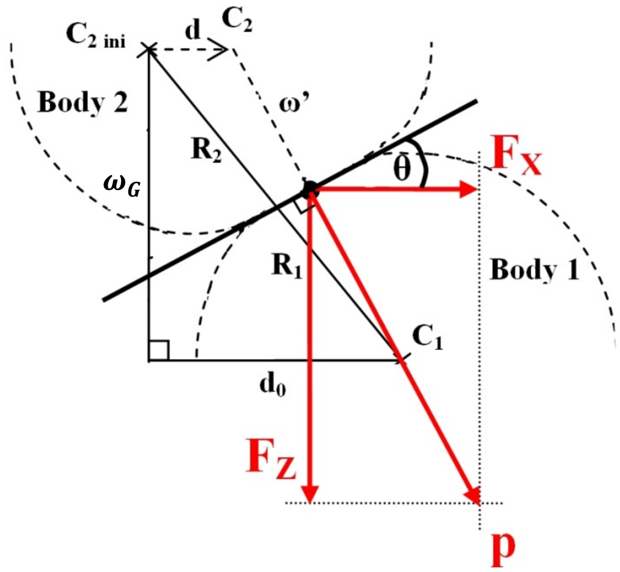

Fig.4.5 Projection in the global reference of the force at a point of the contact surface

4.1.3.2 Pile-up effect

The previous force calculation only takes into account the macro-scale projection. In order to include the effect of the pile-up, it is necessary to study the micro-scale projection. Fig.4.6 shows a magnified view at the point where the pressure p is applied. The residual displacement u^r has a slope that makes an angle θ_{px} with the x'-axis and θ_{py} with the y'-axis.
From this observation, Eq.(4.15), Eq.(4.16) and Eq.(4.17)can be corrected as follows:

$$F_x = n \cdot a_x \cdot a_y \cdot \sum_{I_c} p \cdot \sin\left(\theta - \theta_{px}\right) \tag{4.18}$$

$$F_y = n \cdot a_x \cdot a_y \cdot \sum_{I_c} p \cdot \sin\left(-\theta_{py}\right) \tag{4.19}$$

$$F_x = n \cdot a_x \cdot a_y \cdot \sum_{I_c} p \cdot \cos\left(\theta - \theta_{px}\right) \cdot \cos\left(\theta_{py}\right) \tag{4.20}$$

With:

$$\theta_{px} = \tan^{-1}\left(\frac{\partial u^r}{\partial x}\right) \tag{4.21}$$

And:

$$\theta_{py} = \tan^{-1}\left(\frac{\partial u^r}{\partial y}\right) \tag{4.22}$$

From Eq.(4.8), θ can be expressed as:

$$\theta = \cos^{-1}\left(\frac{\omega_G}{\omega_i'}\right) \cdot \mathrm{sign}(\omega_i' - \omega_{i-1}') \tag{4.23}$$

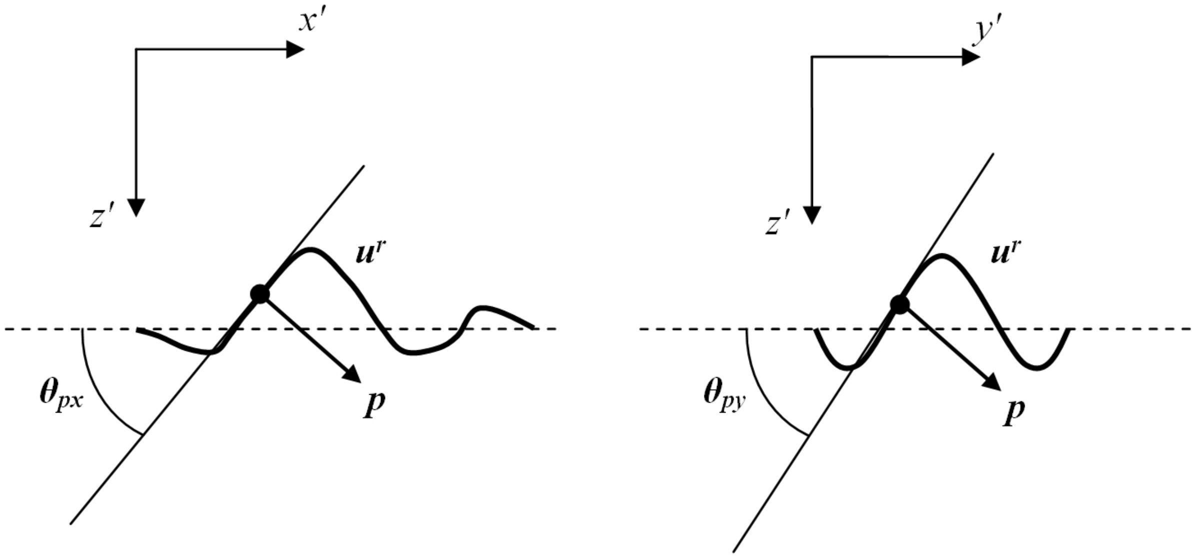

Fig.4.6 Effect of the pile-up due to the slope of the residual displacement

4.2 Simulations and results

The next simulations have been inspired from the work of Vijaywargiya and Green [Vij06] who modeled the sliding contact between two cylinders using a Finite Element model. For the current simulations, two spherical asperities will interact. The radius of the spheres can be taken arbitrarily, so $R_1 = R_2 = 1$ m has been chosen. The elastic properties are $E_1 = E_2 = 200$ GPa for the young moduli, and $\nu_1 = \nu_2 = 0.32$ for the Poisson ratios. The chosen hardening law holds for perfect plasticity with parameter $Y = 0.9115$ GPa for the yield stress.

In most of the results presented, values are normalized by the critical values defined by Green in [Gre05] corresponding to the onset of yielding when plasticity just starts occurring:

$$\omega_c = \left(\frac{\pi C S_y}{2E'}\right)^2 R \tag{4.24}$$

$$P_c = \frac{\left(\pi C S_y\right)^3}{6E'^2} R^2 \tag{4.25}$$

$$U_c = \frac{\left(\pi C S_y\right)^5}{60E'^4} R^3 \tag{4.26}$$

with ω_c the critical interference, which is different and more realistic than in Eq.(2.164), since now a new parameter C is considered, and is a function of Poisson ratio. P_c is the critical load and U_c the maximum potential energy stored during elastic deformation, equals to the work done. In these equations, parameter C is expressed in function of Poisson ratio [Gre05]:

$$C(\nu) = 1.30075 + 0.87825\nu + 0.54373\nu^2 \tag{4.27}$$

Hereafter are plotted the reaction forces during the first sliding pass. The forces are normalized by the critical force found in Eq.(4.25), here $P_c = 3.461.105$ N, and the abscissa along the sliding direction by the equivalent radius i.e. $R = 0.5$m. Fig.4.7 and Fig.4.8 give the tangential and the normal forces, respectively, when increasing the dimensionless interference ω/ω_c, i.e. the interference found in Eq.(4.14) normalized by the critical interference found in Eq.(4.24). FE simulation results [Moo07] are also plotted for comparison with the Semi-Analytical results. It can be seen in Fig.4.7 that for small interference values, the tangential force is anti-symmetric, and vanishes when the asperities are perfectly aligned, i.e. for $X/R = 0$. On the other hand, for large values of the interference, one can see that the curve is not anti-symmetric anymore. It means that most of the energy (area under the curve) is produced during loading, i.e. before the asperities are aligned, and just a small part of the energy is released during unloading, i.e. when the asperities are repulsing each other. Also, the value of the force when the asperities are aligned does not vanish anymore; this phenomenon is due to plastic deformation. Indeed, the residual displacement on the surface of the bodies induces some pile-up since the normal contact plane is not parallel to the sliding direction any longer.

The normal force plotted in Fig.4.8 is symmetric for low interference values. Then a slight asymmetry begins to appear when increasing the interference, however less pronounced than for the tangential force. Again, this phenomenon is due to plasticity, since due to the permanent deformation of the surface that takes place during the first loading cycle, the normal contact plane and the sliding direction are not parallel.

To give an idea of energy loss during the sliding process, Fig.4.9 shows the evolution of the net energy normalized by the critical energy found in Eq.(4.26), versus the dimensionless interference.
A load ratio is now defined as F_X/F_Z the ratio of the tangential force over the normal one. Results are plotted in Fig.4.10 versus the normalized sliding distance. It should be noted that the current simulation was made under the assumption of frictionless contact, therefore the load ratio is only related here to the ploughing or tugging phenomena. It can be seen that for small interference values this ratio is almost perfectly antisymmetric. An increase of the load ratio is found at the beginning of the tugging (left part of Fig.4.10) when increasing the interference. Conversely the F_X/F_Z ratio tends to reach an asymptotic value of 0.045 at the end of the contact (right part of the curves). In addition, it can be observed that this ratio is not nil anymore when the asperities are aligned, this offset increasing with the interference value. It is again assumed to be due to plastic deformation inducing pile-up.
Another interesting result is the evolution of the permanent deformation of the surface. Fig.4.11 shows the maximum value of the residual displacement after unloading normalized by the critical interference given in Eq.(4.24), as a function of the interference. It shows a very significant residual deformation of the surface, up to 25% of the interference.
Representative computation times corresponding to $w/w_c = 9$, for the mesh-size $dx = 3.85$mm, $dy = 7.7$mm, $dz = 1.925$mm (i.e., 33 x 13 x 31 = 13,299 points) in the plastic zone, and 25 time-step increments to describe the relative motion, took about 25 minutes on a 1.8 GHz Pentium M personal computer.
The simulation made in Fig.4.7 and Fig.4.8 with the FE software [Moo07] took about a week in order to get the same order of accuracy.

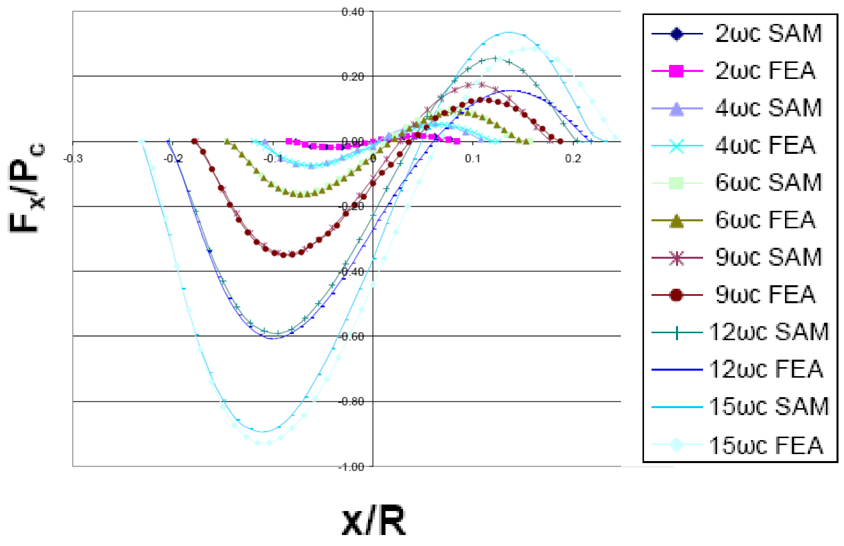

Fig.4.7 Dimensionless tangential force during sliding vs. dimensionless sliding direction. Comparisons with FE simulation

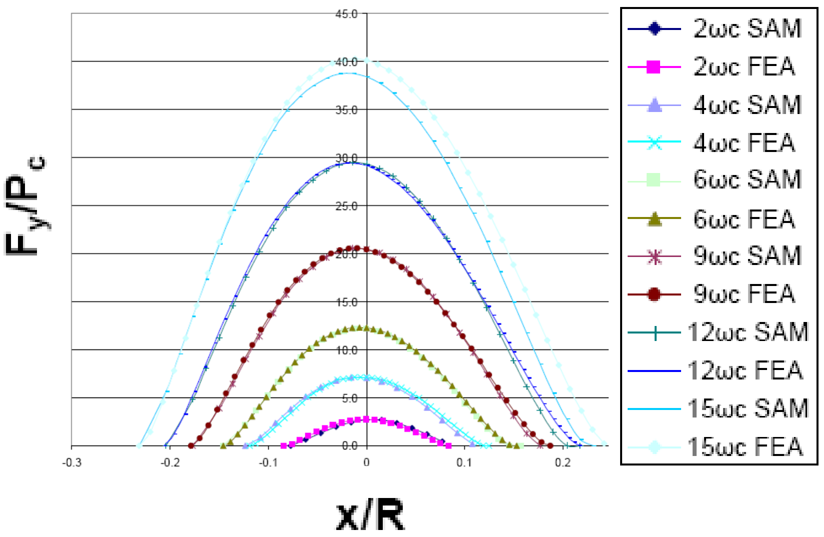

Fig.4.8 Dimensionless normal force during sliding vs. dimensionless sliding direction. Comparisons with FE simulation

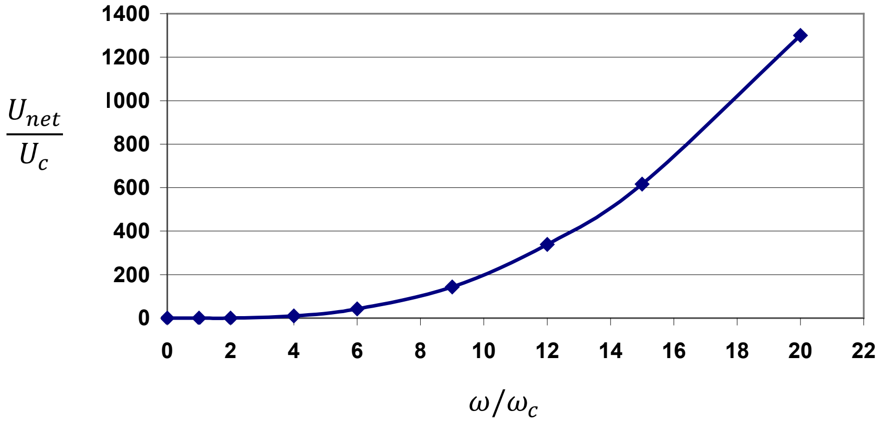

Fig.4.9 Dimensionless net energy vs. dimensionless interference

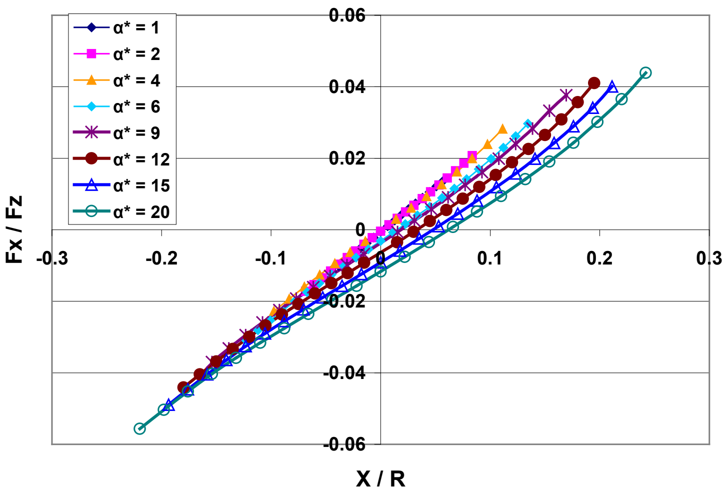

Fig.4.10 Load ratio during sliding vs. dimensionless sliding direction

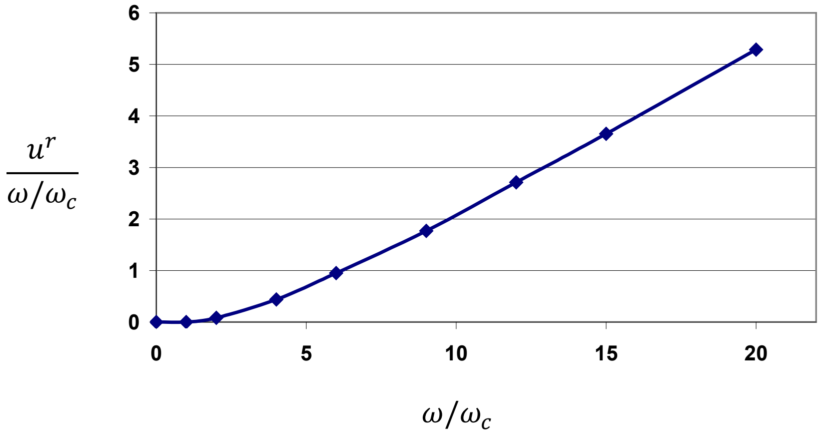

Fig.4.11 Dimensionless residual displacement vs. dimensionless interference

Part 5
Development of a model to study running-in and wear of two bodies in sliding contact

This last part is an application of the code to wear or running-in prediction. This is a way to show the powerful capacities of semi-analytical techniques, since the simulation of a cyclic contact, while removing material at each cycle takes a reasonable time. The origin of the model is first presented, and is followed by the adaptation of the computing code. Then numerical issues are discussed, for users or developers to be aware of the problem of material removing when a discretized body is in consideration. In order to illustrate the model, the wear of a flat surface, and the running-in of a rough surfaces are studied

5.1 Wear and running-in model

5.1.1 Origin of the modeling

The wear model is based on a strain criterion, corresponding to the (local) fracture of a polycrystalline material. Ludwik suggested in 1927 that, in addition to the easily observed stress-strain curve for flow, there exists a fracture stress versus strain curve that defines the fracture stress at every value of strain as shown schematically Fig.5.1, see [Pol66]. As the flow stress increases with strain, the flow and fracture curves eventually intersect and the material breaks. For bearing steels or most gear steels, which have relatively high yield stress, a tensile test leads to the fracture of the test specimen when a very low equivalent plastic strain is reached – typically in the order of the percent, see Fig.5.2 where a 16NiCrMo13 carbonized steel was tested, and where the critical equivalent plastic strain was found to be 0.2%. As discussed in the introduction it has been shown by [Oil05] that a (micro-)crack may occur at the boundary between the plastic deformed region (PDR) and the elastic surrounding region, as shown Fig.5.3. The PDR found here is formed at the contacting surface of two rough specimens during rolling/sliding contact test.

After unloading a plastic zone may appear at the surface of one of the contacting bodies, due to either high surface shear stress or due to the presence of surface defects (dents, roughness). The wear model is based on a strain criterion. It is assumed that the volume of material where the equivalent plastic strain found after unloading exceeds a threshold value, and when located at the surface, will detach from the surface after very few cycles, let say after a single cycle. It should be mentioned that the plastic strain fields found under load and after unloading are identical here since an isotropic hardening law is used. The numerical procedure consists then, after each elastic-plastic contact simulation, in i) determining the plastic volume that will detach, and ii) updating the geometry that will be used for the next geometry.

Note that this approach may also be applied to the running-in of rough surfaces.

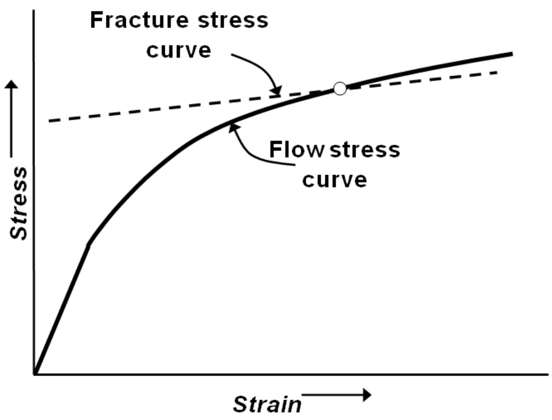

Fig.5.1 Proposal of Ludwik suggesting that fracture occurs at a point, F, where flow stress and fracture stress vs. strain curves intersect, from [Pol66].

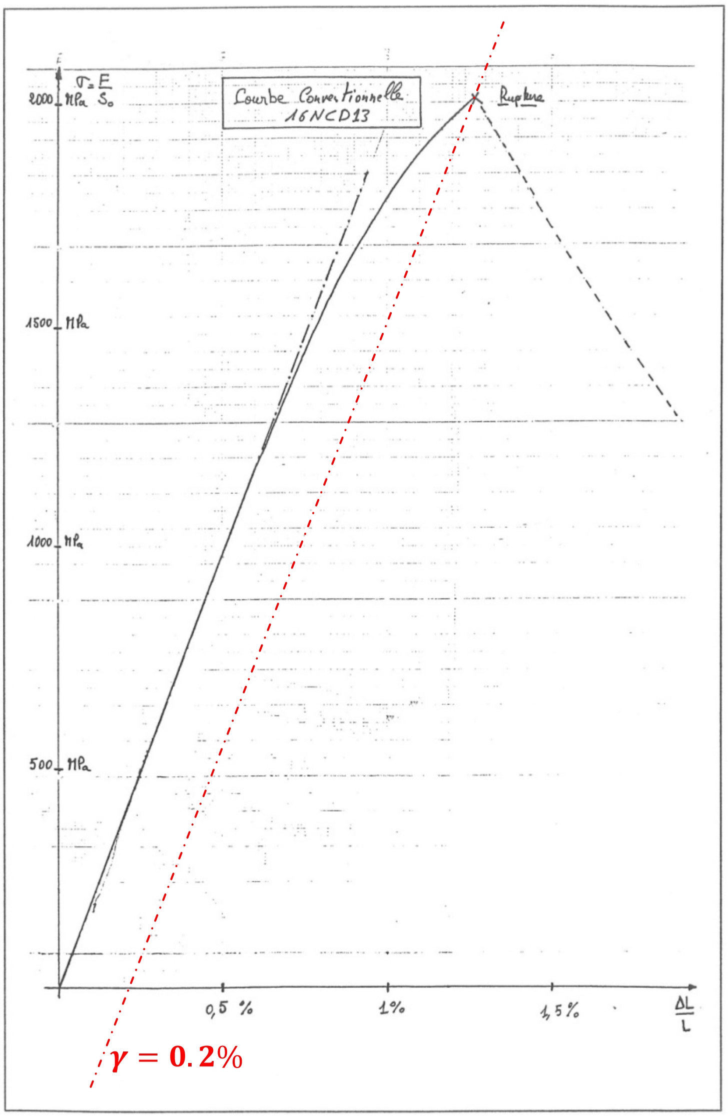

Fig.5.2 Traction test for 16NiCrMo13 carbonized steel. The carbon rate corresponds to the surface layer

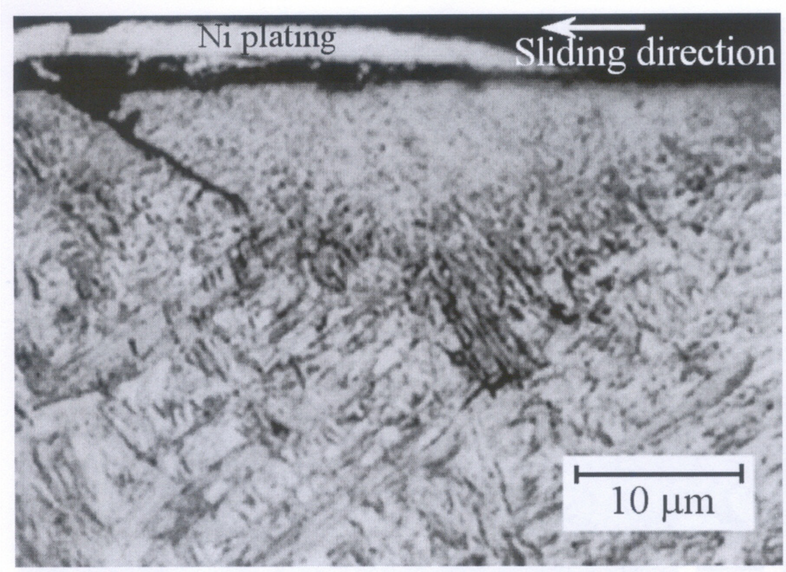

Fig.5.3 Micrograph showing Plastic Deformed Region (PDR) bordered by Dark Etching Region (DER) for a gear material after a nital etch, from [Oil05].

5.1.2 Algorithm

First, the vertical (see Part 2) or the rolling and sliding (0) contact needs to be computed, using the algorithm in Fig.2.1. Then at the end of calculation, the plastic zone is analyzed and the location of equivalent plastic strains exceeding the critical equivalent plastic strain is memorized, and removed from the worn body. Then the surface and the plastic state are updated in order to start the new iteration, until a desired number of iterations, or after running-in, when no plastic strain is appearing anymore.
The algorithm is presented in Fig.5.4.

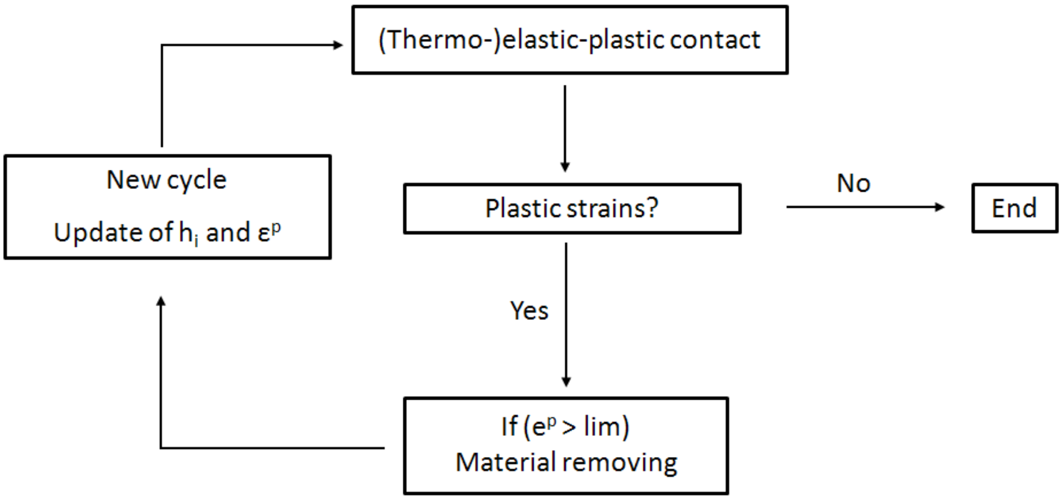

Fig.5.4 Algorithm for prediction of wear and running-in

5.1.3 Numerical issues

Some numerical problems can be encountered if special care is not made. First, since the body is discretized into cuboids, the geometry of the wear volume is not realistic and may lead to non-coherent results. A more precise zone needs to be located, see section 5.1.3.1.
Then, once the wear volume is removed, some border effects are present, and need to be annihilated, for the calculation to converge, see section 5.1.3.2.

5.1.3.1 In-depth interpolation

The first issue to be dealt with is the geometry of the wear volume. Indeed, since the body is discretized into cuboids, the profile is not regular (see red cuboids in Fig.5.5.
An interpolation of the equivalent plastic strain is made in function of the depth in order to get the exact location of the critical value, see Fig.5.6.

The interpolation used is the same as in Eq.(2.166) where x is equal to the critical equivalent strain (0.2% in Fig.5.3Fig.5.2), and where P_j^L are the Lagrange polynoms expressed in Eq.(2.167) where x_j are the values of the equivalent plastic strains, and y_j the values of the corresponding depths.

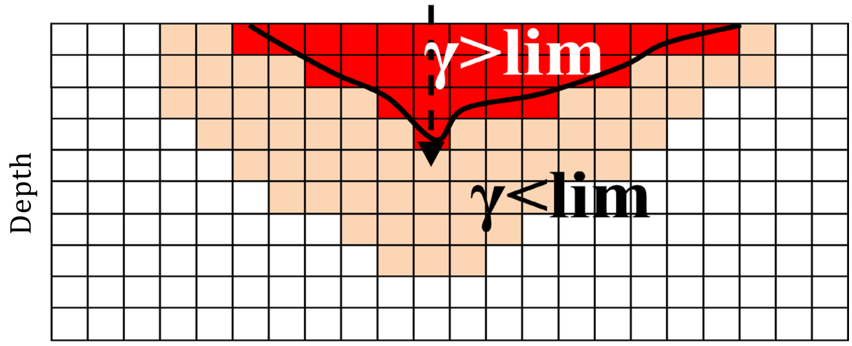

Fig.5.5 Zone where there are plastic strains (red + pink cuboids), and zone where equivalent plastic strain exceeds the critical value (touching the surface)

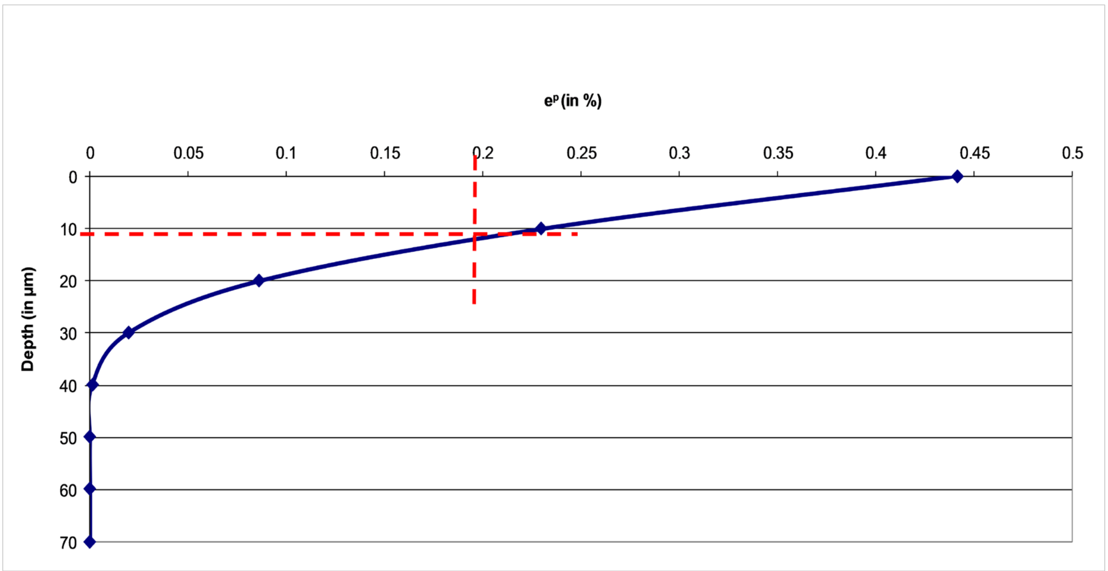

Fig.5.6 Interpolation of the equivalent plastic strain vs. the depth

Once the surface where equivalent plastic strains exceed the critical value is swept, and the exact location of the whole wear volume is found, the plastic strain tensor is updated for the remaining volume. To reach this, let us consider a point of the surface. The exact location of the wear depth is saved, and becomes the new point on the surface in order to be coherent with the semi-infinite bodies' hypothesis. Then, a new similar interpolation of all the points in depth is needed, in order to respect the re-mesh the volume, which needs to be regular.

5.1.3.2 Border smoothing

In the previous section, the interpolated wear profile has been computed, and allowed to get a smooth surface, instead of a discontinuous surface (due to the discretization). A new issue is now found at the border of the removed wear volume. Indeed, the discontinuity can induce huge wear rate at the next iteration, due to the peak of pressure yielding to huge plastic strain, see Fig.5.7.

To solve this problem, a Savitsky Golay filter [Pre92] in two-dimension is used, and allow the user of the computation code to manage the wear evolution, see Fig.5.8. For example, for a brittle material, a very few smoothed points will be used, to take into account the physical discontinuities at the border of the removed material, whereas modeling a more ductile material would need several smoothed points. This choice of calibrating these parameters (one in each dimension) is free to the user, in order to get closer to the corresponding experiments.

It has to be noted that after the smoothing process is realized, the wear volume has to be conserved, in order to be coherent with the reality. This is numerically identical to the process in Eqs.(2.124) and (2.125) in the contact algorithm. Basically, the wear volume is calculated before smoothing (see Eq.(5.1)) and after smoothing (see Eq.(5.2)). Then the wear displacement is computed in Eq.(5.3) and is added to the initial geometry as for the residual displacement, in order to get a modified initial geometry for the next contact iteration, see Eq. (2.96).

$$V^{wear} = a_x\, a_y \sum_{(i,j)\epsilon I_w} u_{ij}^{wear} \tag{5.1}$$

where a_x and a_y are the grid spacings in x and y-directions respectively, and I_w denotes the set of all grid nodes on the surface, that corresponds to the region where wear is calculated.

$$(V^{wear})_{smoothing} = a_x\, a_y \sum_{(i,j)\epsilon I_w} (u_{ij}^{wear})_{smoothing} \tag{5.2}$$

$$u_{ij}^{wear} \leftarrow \left(\frac{V^{wear}}{(V^{wear})_{smoothing}}\right) (u_{ij}^{wear})_{smoothing}, \qquad (i,j) \in I_w \tag{5.3}$$

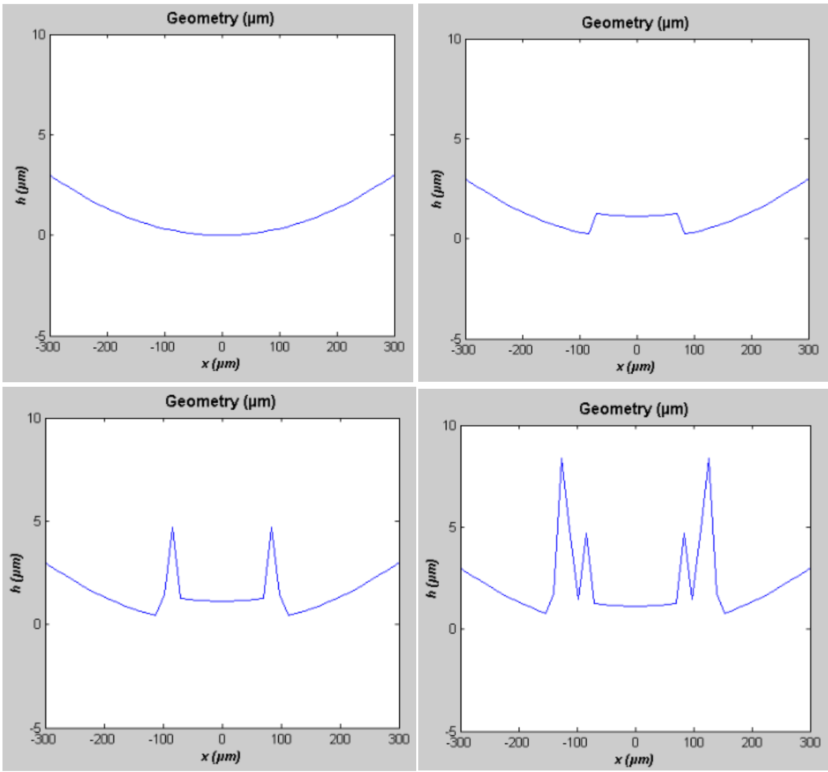

Fig.5.7 Border effects, and discontinuity of the new worn surface after successive iterations (from top to down, from left to right)

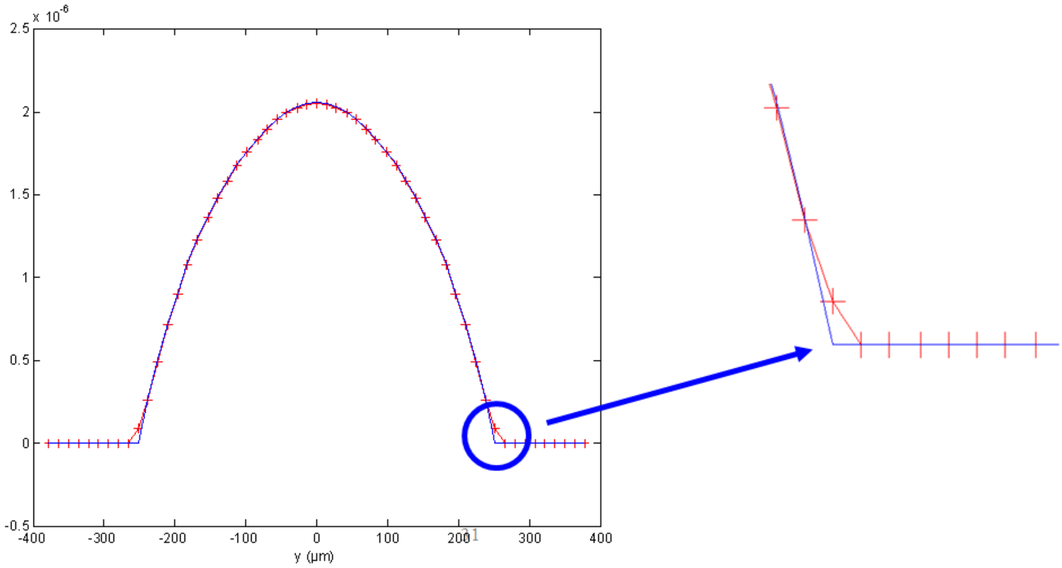

Fig.5.8 Border smoothing, using Savitsky Golay filter

5.2 Results

Two academic simulations are presented. The first one corresponds to the vertical loading of two surfaces initially smooth. The second simulation deals with an isotropic rough surface vertically loaded against a smooth one. For both simulations a tangential loading proportional to the normal load is applied (during loading-unloading both tangential and normal loading are here applied simultaneously). It is assumed that the linear relation between the tangential and the normal loads results in a uniform friction coefficient (Coulomb law). The contact between two ideally smooth surfaces illustrates the mechanism of wear at moderate contact pressure (just above the critical contact pressure) when the plastic zone is found at the surface, i.e. when the friction coefficient is above 0.3. The contact between a rough loaded against of smooth surface illustrates the mechanism of running-in for the same localized contact pressure as found at the top of asperities, which in fact is very similar to the smooth case except the scale. The smooth situation will result in a deterioration of the surface roughness (i.e. wear), whereas the rough situation will result in a flattening of the roughness pattern (i.e. running-in).

5.2.1 Wear of a flat surface

The bodies' radii are 15 mm, the Young's modulus is 210 GPa, the Poisson coefficient is 0.3, and the friction coefficient is chosen uniform, constant, and equal to 0.4. A Swift law (see Eq.(2.162)) is used with parameters $B = 1735$ MPa, $C = 16$ and $n = 0.067$. For each cycle the normal load is oscillating between 0 N and 2000 N. In this example, the mesh size is 30μm in the x-direction, and 6μm in the z-direction.
The pressure distribution and the equivalent Tresca stress are given for the first cycle and under loading in Fig.5.9a and Fig.5.9b. The corresponding hydrostatic pressure and equivalent plastic strain are given in Fig.5.9c and Fig.5.9d. The hydrostatic pressure (one third of the trace of the stress tensor) is here calculated after unloading.
The algorithm is based on the material removal corresponding to a plastic zone where the equivalent plastic strains are greater than a threshold value, arbitrarily chosen here equal to 0.2%, which is a realistic value for high carbon content steel. The numerical simulation shows that the surface is worn at a constant rate, and leads to a non-stabilized state. For example the resulting wear after 13 cycles is shown Fig.5.10.
The subsequent final stress and strain state is given Fig.5.11 in terms of contact pressure profile and equivalent Tresca stress for the loaded state, and hydrostatic pressure and equivalent plastic strains for the unloaded state.

5.2.2 Running-in of a rough surface

The macro-geometry and the material parameters are identical to the previous case. This time for each cycle the normal load is oscillating between 0 N and 30 N and the mesh size is 5 μm in the x- and y-directions and 0.5 μm in the z-direction. The roughness is modeled by a sine function of coordinates x and y, with amplitude A and wavelengths λ_x and λ_y in the x- and y-directions, respectively, Eq.(5.4):

$$r(x,y) = A \cdot \sin\left(\frac{2\pi x}{\lambda_x}\right) \cdot \sin\left(\frac{2\pi y}{\lambda_y}\right) \tag{5.4}$$

The initial surface, with a profile shown in Fig.5.12, presents an isotropic roughness pattern corresponding to the following parameters: $A = 0.5$ µm, $\lambda_x = \lambda_y = 50$ µm.

The pressure distribution and the equivalent Tresca stress are given for the first cycle and under loading in Fig.5.13a and Fig.5.13b. The corresponding hydrostatic pressure and equivalent plastic strain are given in Fig.5.13c and Fig.5.13d.

After seven iterations, the surface profile does not change any more, and results in the geometry given Fig.5.14. It means that no further plastic flow occurs with equivalent plastic strain remaining lower than the threshold value of 0.2%. The subsequent final stress and strain state is given Fig.5.15 in terms of contact pressure profile and equivalent Tresca stress for the loaded state, and hydrostatic pressure and equivalent plastic strains for the unloaded state (Fig.5.15a to Fig.5.15d, respectively). As a general remark it can be seen that the stress level decreases with cycles, resulting from the running-in of the surface roughness.

It should be mentioned that, although the contact load is very different for the two situations studied, it produces the same magnitude of contact pressure (localized for the rough surface) which at the end affects only the scale of the plastic zone. Indeed the relatively low load used for rough contact simulation would not result in any wear if the two surfaces are assumed smooth since the material behavior would remain purely elastic. Conversely applying for the rough simulation the same loading as the one used in the smooth case (i.e. relatively high in comparison to the yield flow) should lead very quickly to a contact situation close to the smooth case considering that asperities would be quickly flattened due to localized plasticity and subsequent wear.

The investigation presented here is limited to academic simulations. Results provided i) prove the performance of the semi-analytical approach and ii) illustrate the mechanism proposed to reproduce wear and running-in. Further work is now required to evaluate the effect of mesh size, hardening law, plastic strain threshold, operating conditions, and surface roughness on the wear rate and running-in process.

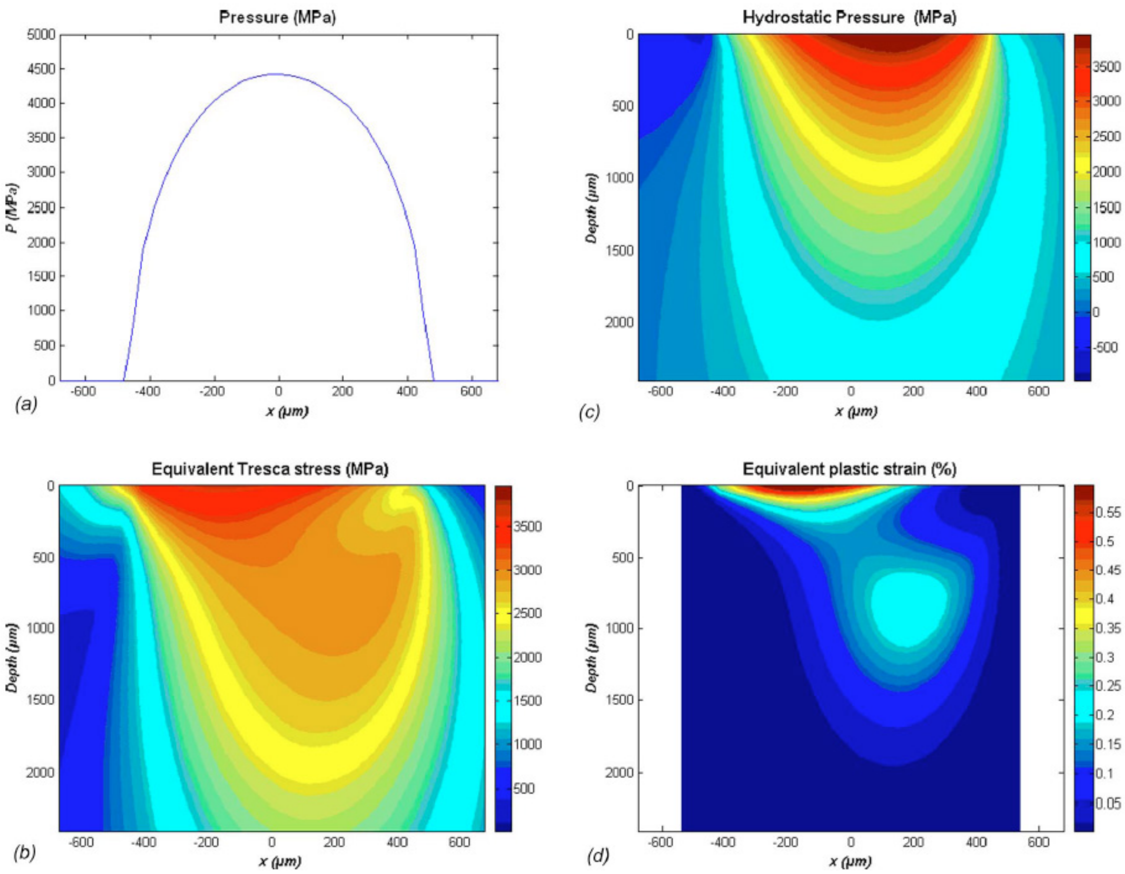

Fig.5.9 Contact between two initially smooth surfaces – first cycle – a) and b) under load, c) and d) after unloading
a) Contact pressure, b) equivalent Tresca stress, c) hydrostatic pressure, d) equivalent plastic strain

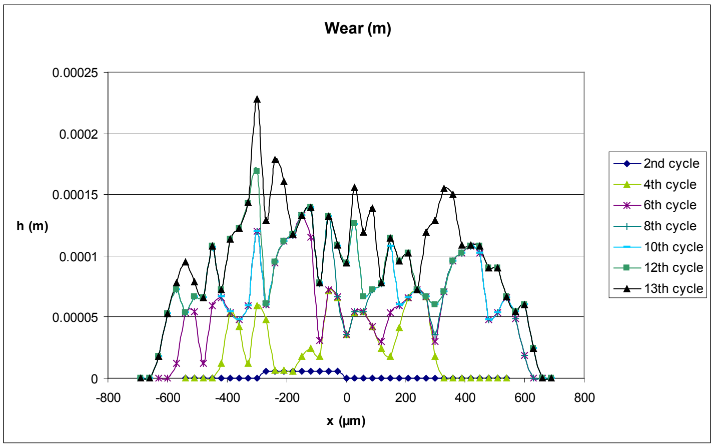

Fig.5.10 Contact between two initially smooth surfaces – Wear profile after cycling loading (up to 13 cycles)

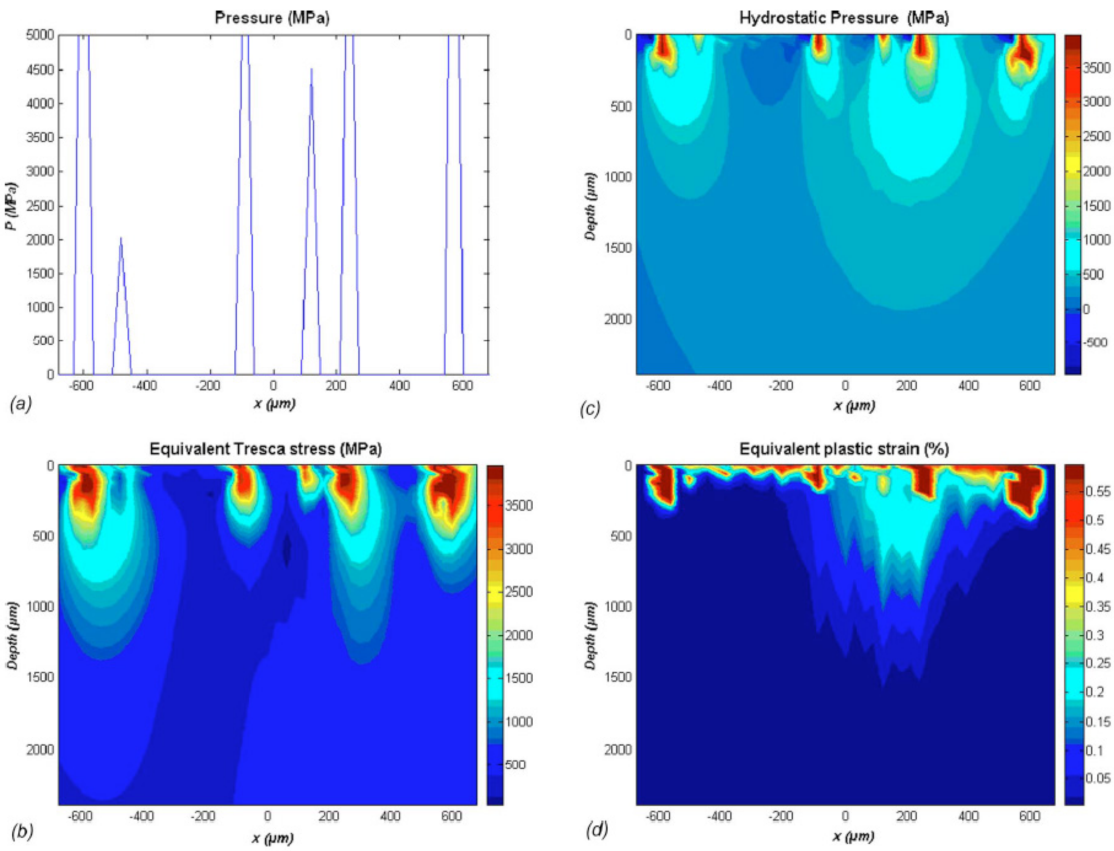

Fig.5.11 Contact between two initially smooth surfaces – state after 13 loading cycles – a) and b) under load, c) and d) after unloading
a) Contact pressure, b) equivalent Tresca stress, c) hydrostatic pressure, d) equivalent plastic strain

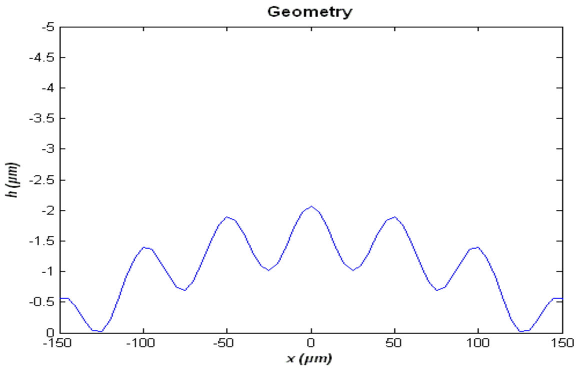

Fig.5.12   Initial profile of the isotropic rough surface

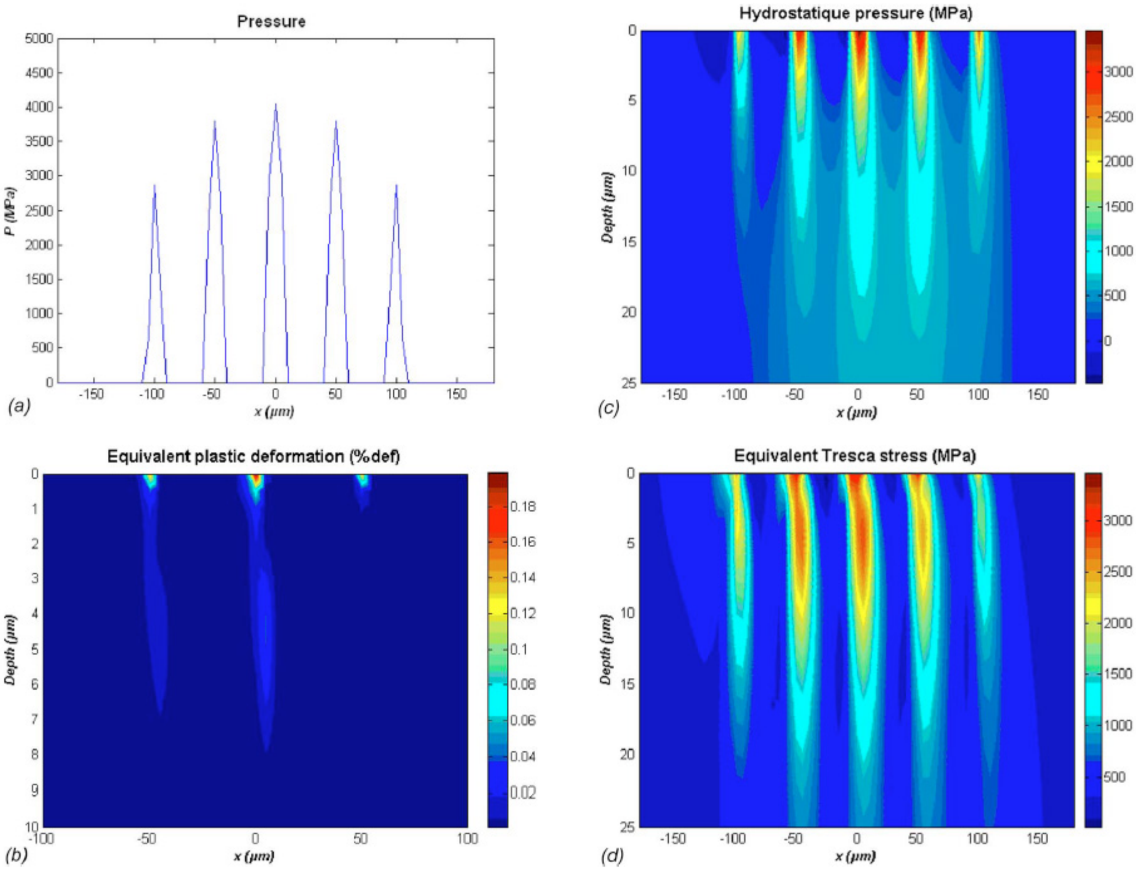

Fig.5.13   Contact between an initially isotropic rough surface and a smooth one – first cycle – a) and b) under load, c) and d) after unloading. a) Contact pressure, b) equivalent Tresca stress, c) hydrostatic pressure, d) equivalent plastic strain

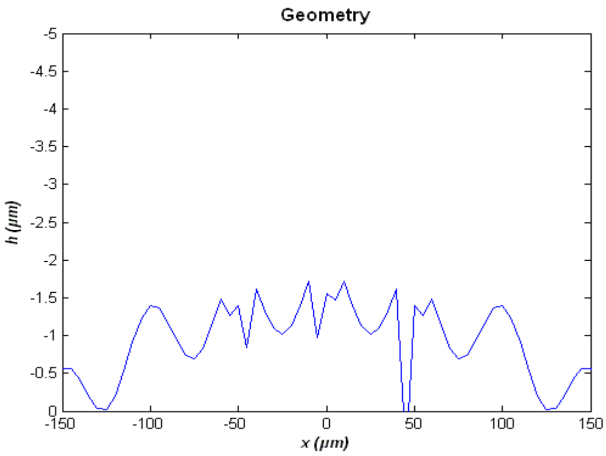

Fig.5.14 Contact between an initially isotropic rough surface and a smooth one – final surface (worn geometry), after cyclic loading

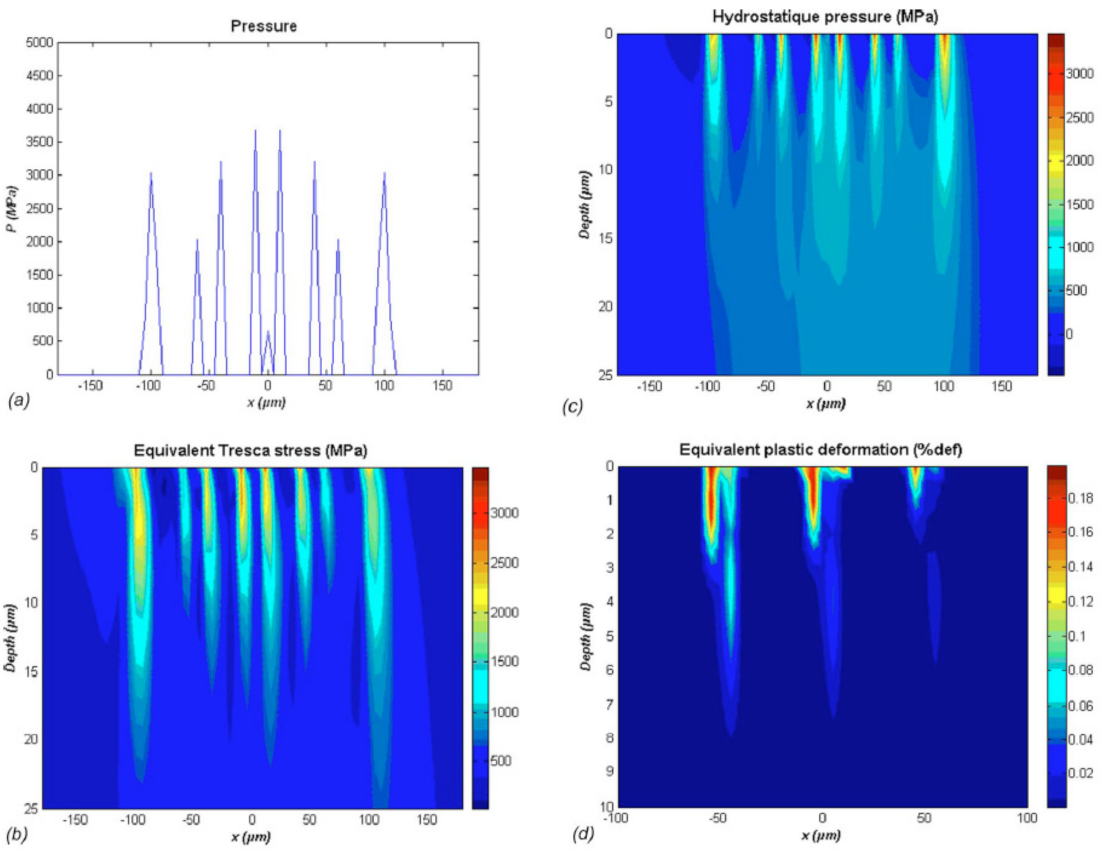

Fig.5.15 Contact between an initially isotropic rough surface and a smooth one – stabilized state after 7 cycles – a) and b) under load, c) and d) after unloading. a) Contact pressure, b) equivalent Tresca stress, c) hydrostatic pressure, d) equivalent plastic strain

Conclusions

Mechanical components of high level of reliability are usually designed to operate with low level of stress, ideally below the yield stress. A contact overload may however be encountered accidentally or be the result of a transient operation regime. In other components operating under severe or extreme conditions the yield stress is often exceeded during the normal running conditions.
Prior to study the effect of the material hardening on the fatigue life it is interesting to describe the effects of such an overload on the contact behavior and residual state

A semi-analytical and three-dimensional thermal-elastic-plastic model has been developed, taking into account both normal and tangential loading. The model is applicable for rolling and/or sliding contact problem, as far as small equivalent plastic strain hypothesis is respected. The contact solver which is based on the conjugate gradient and Fast Fourier Transform techniques allows to solve the transient thermal-elastic-plastic contact problem within a reasonable computing time even when a fine mesh is required, i.e. within a few minutes up to a few hours (for 10^6 grid points) on a PC computer, mostly depending on the number of cells inside the plastic zone. A return-mapping algorithm has also been successfully implemented in the thermal-elastic-plastic contact solver. It improves the contact code in terms of computing time and robustness. The proposed method is an alternative to the use of the FEM for example to study the effects of a geometrical surface defect on the fatigue of the contacting materials, including the case when a fine mesh is required as for the inclusion of roughness, and/or indents

The model has been validated by comparisons with experiments and 3D FEM results obtained with the commercial software Abaqus. These comparisons have shown a nice validation.

The formulation proposes to drive the computation by imposing either a load, or a normal rigid body displacement also called contact interference.
Some improvements have also been done in order to deal with two identical elastic-plastic bodies in contact. It has been shown a significant reduction of

the contact pressure compared to the situation when a purely elastic body is in contact with an elastic-plastic one

The stress and strain states after the vertical loading and after unloading of an elastic-plastic half-space by an elastic sphere have been investigated for a steady-state problem with combined normal and tangential loading and compared to the purely normal loading case. The results presented have shown a significant effect of the tangential loading not only on the magnitude and location of the maximum Von Mises stress found under loading, but also on the residual stresses and strains which remain after unloading. An interesting point is the existence of a residual tensile zone between the hertzian depth and the surface, which was identified by mean of the hydrostatic stress

Also, the presence of frictional heating in elastic-plastic contact has been studied. The contribution of both plasticity and dilation thermal strains has been identified. The results presented have shown a beneficial effect of the temperature field on the subsurface stress and residual stress states, when the heat factor remains below 0.075 m/s. This phenomenon is explained by the thermal dilation strains that act to relax the stress field in the zone located between the surface and the hertzian depth, moving the area where the equivalent von Mises stress is found maximum at a depth below the conventional hertzian depth. For a higher heat factor and after a transition zone, it has been found that plasticity is mainly due to thermal dilation strains.

In the rolling and sliding contact section, the elastic-plastic response of a half-space normally loaded by a rolling elastic sphere or ellipsoid has been investigated and results presented. The effect of the ellipticity ratio and contact pressure on the surface permanent deformation and subsurface stress and strain state has been analyzed.
For a circular point contact it has been shown that the permanent surface print is deeper for a rolling load than for a point experiencing a vertical loading and unloading. The steady-state regime is reached after a very few number of cycles when using an isotropic hardening model, typically 2 or 3. Moreover it is found a tensile zone lying on the surface of the elastic-plastic body on both side of the rolling track.
For elongated contact with a semi-major axis perpendicular to the rolling direction it is found a shallower but wider surface print and a lower level of residual stress and strain when increasing the ellipticity ratio while main-

taining constant the maximum Hertz pressure. This point should be carefully considered when extrapolating experimental fatigue life data obtained on any analytical ball on flat test apparatus to real rolling bearings. Less surprising is the effect of the contact pressure on the surface and subsurface stress and strain for an elastic-plastic contact with an ellipticity ratio of *8*. Residual stress and strain are found to increase with the normal load, up to 2.1% for the equivalent plastic strain and 935 MPa for the equivalent Von Mises stress for AISI 52100 bearing steel with a frictionless rolling load of 8 GPa

In order to complete the study, the tugging between two single asperities has then been investigated. Results have shown that plasticity produces an asymmetry of the normal and tangential loading during the transient contact. A load ratio due to ploughing has been estimated. Compared to Finite Element modeling, the developed code allows the user to compute a rolling and sliding contact in very short CPU times

In the last part, a new wear prediction model has been proposed. This formulation is based on material removal due to the formation of plastically deformed regions (PDR) at the surface of bodies in contact.
First results show two possible modes of wear progression, one corresponding to a continuous increase of the wear volume, the second corresponding to a running-in situation where the wear rate tends to zero.

Next developments will be to make some effort to identify the effect of temperature on the hardening law for real engineering applications.
Also, fretting problems are of primary interest for industry. The coupling between the tangential and normal effects is of high order, and is not accurately dealt for the moment with the present approach. Some research is currently in progress to correctly deal with full tangential problems.
Another application that is nowadays interesting for industry is the shot penning process. In order to use semi-analytical techniques for this aim, dynamic effects and body forces are to be included. This work is also in process, and should give interesting results.

The current work also provides the foundation to incorporate electrical-mechanical interaction between rough surfaces by progressively introducing the relevant physical phenomena.

Finally, semi-analytical techniques are of great interest for researchers since the theory is really complex, and engineers in industry see the powerful capacities of such approaches, when comparing computing times to identical Finite Element simulations, making possible to deal with cycling and complex contact problems.

Appendix

Appendix 1: Temperature Distribution, Transient Thermoelastic Stress and Displacement Fields in a Half-Space

In this section three different cases are treated: the transient-continuous case with a time-independent heat source and results analyzed at an arbitrary time, the steady-state case with a time-independent heat source and results analyzed at an infinite time, and the transient-instantaneous case with a time-dependent heat source and results analyzed at an arbitrary time.

Let us assume that the half-space subjected to frictional heating is uniformly moving (translating) with Péclet numbers $P_{e_j} = V_j\, l \,/\, \kappa$ (j =1 and 2), V_j being the velocities, l the characteristic length (size of calculation zone), and κ the thermal diffusivity.

The micromechanics-based approach presented in [Liu01a] is used to obtain the frequency response function (FRFs) of the thermoelastic field at any position of stationary or moving bodies, since solutions in the frequency domain are much more convenient to obtain, using Fourier transform.

Most of the derivations can be found in [Liu03] where two-dimensional Fourier transform are applied to the expressions of displacements and stresses. Corresponding thermoelastic field in the frequency domain can then be expressed as:

$$\tilde{\tilde{u}}_i = -\frac{i\,\omega_i}{4\,\pi}[\tilde{\tilde{\varphi}}^I + (3 - 4\,\nu - 2\,x_3\,w)\tilde{\tilde{\varphi}}^{II}], \qquad i = 1{,}2 \tag{A1.1}$$

$$\tilde{\tilde{u}}_3 = -\frac{1}{4\,\pi}\left[\tilde{\tilde{\varphi}}^I_{,3} + (3 - 4\,\nu + 2\,x_3\,w)\,w\,\tilde{\tilde{\varphi}}^{II}\right] \tag{A1.2}$$

$$\begin{aligned}\tilde{\tilde{\sigma}}_{11} = c_m \Big[&-4\,\pi\,\tilde{\tilde{T}} + \omega_1^2\,\tilde{\tilde{\varphi}}^I \\ &+ \{(3 - 4\,\nu)\,\omega_1^2 + 4\,\nu\,w^2 - 2\,x_3\,w\,\omega_1^2\}\,\tilde{\tilde{\varphi}}^{II}\Big]\end{aligned} \tag{A1.3}$$

$$\tilde{\tilde{\sigma}}_{22} = c_m \Big[-4\,\pi\,\tilde{\tilde{T}} + \omega_2^2\,\tilde{\tilde{\varphi}}^I + \{(3-4\,\nu)\,\omega_2^2 + 4\,\nu\,w^2 - 2\,x_3\,w\,\omega_2^2\}\,\tilde{\tilde{\varphi}}^{II}\Big] \quad (A1.4)$$

$$\tilde{\tilde{\sigma}}_{33} = c_m \Big[-4\,\pi\,\tilde{\tilde{T}} - \tilde{\tilde{\varphi}}^I_{,33} + (1+2\,x_3\,w)w^2\,\tilde{\tilde{\varphi}}^{II}\Big] \quad (A1.5)$$

$$\tilde{\tilde{\sigma}}_{12} = c_m[\tilde{\tilde{\varphi}}^I + (3-4\,\nu-2\,x_3\,w)\,\tilde{\tilde{\varphi}}^{II}]\omega_1\omega_2 \quad (A1.6)$$

$$\tilde{\tilde{\sigma}}_{13} = c_m\big[-\tilde{\tilde{\varphi}}^I_{,3} + (1-2\,x_3\,w)w\,\tilde{\tilde{\varphi}}^{II}\big]\,i\,\omega_1 \quad (A1.7)$$

$$\tilde{\tilde{\sigma}}_{23} = c_m\big[-\tilde{\tilde{\varphi}}^I_{,3} + (1-2\,x_3\,w)w\,\tilde{\tilde{\varphi}}^{II}\big]\,i\,\omega_2 \quad (A1.8)$$

Where " $\tilde{}$ " means a Fourier transform operation, φ^I is the Newtonian potential of a distribution of matter of density, T, and φ^{II} is the reflection transformation of φ^I.

$$c_m = \frac{\mu(1+\nu)}{2\pi(1-\nu)} \quad (A1.9)$$

is a material constant, ω_1 and ω_2 are the angular frequencies in the frequency domain.

$$w = \sqrt{\omega_1^2 + \omega_2^2} \quad (A1.10)$$

is defined as a radius in the frequency domain, and

$$w' = \sqrt{w^2 + i\left(\omega_1\,P_{e_1} + \omega_2\,P_{e_2}\right)} = \sqrt{w^2 - a_\omega} \quad (A1.11)$$

is an effective radius in the frequency domain.

$$a_\omega = -i\left(\omega_1\,P_{e_1} + \omega_2\,P_{e_2}\right) \quad (A1.12)$$

is introduced to simplify the following expressions.

In Eqs.(A1.1) to (A1.8) the double Fourier transform is with respect to the surface, x_1 and x_2 while x_3, the depth is explicitely shown. Expressions in the frequency domain for the temperature field, the two potentials, and derivates of φ^I are necessary in Eqs.(A1.1) to (A1.8) and are given next, for the three cases of considerations, where Péclet numbers (or velocities) are constant.

Before, six additional functions f_+, f_-, g_+, g_-, h, and I need to be defined for the transient-continuous case. In the following, a variable $x_t = \kappa t/l^2$ is introduced, and is linked to the observation time t:

$$f_\pm = \exp(\pm w x_3)\,\mathrm{erfc}\left(w\sqrt{x_t} \pm \frac{x_3}{2\sqrt{x_t}}\right) \tag{A1.13}$$

$$g_\pm = \exp(\pm w' x_3)\,\mathrm{erfc}\left(\pm w'\sqrt{x_t} + \frac{x_3}{2\sqrt{x_t}}\right) \tag{A1.14}$$

$$h = 2\sqrt{\frac{x_t}{\pi}}\exp\left(\frac{-w^2\, x_t - x_3^2}{4\, x_t}\right)\mathrm{erfc}\left(w\sqrt{x_t} \pm \frac{x_3}{2\sqrt{x_t}}\right) \tag{A1.15}$$

$$I(w, x_3, a_\omega, x_t) = \int (f_+ + f_-)\exp(a_\omega\, x_t)\, dx$$
$$= \begin{cases} \dfrac{1}{a_\omega}\left[(f_+ + f_-)\exp(a_\omega\, x_t) + \dfrac{w}{w'}(-g_+ + g_-)\right], & w \neq 0, a_\omega \neq 0 \\ f_-\left(x_t + \dfrac{w x_3 - 1}{2w^2}\right) + f_+\left(x_t - \dfrac{w x_3 + 1}{2w^2}\right) - \dfrac{h}{w}, & w \neq 0, a_\omega = 0 \\ 2x \quad , & w = 0, a_\omega = 0 \end{cases} \tag{A1.16}$$

Transient-continuous case

For the transient-continuous case, Eqs.(A1.1) to (A1.8) are recovered using the followings:

$$\frac{\tilde{\tilde{T}}}{\tilde{\tilde{q}}} = \begin{cases} (g_- - g_+)/(2w'), & w' \neq 0 \\ \left[2\exp\left(-\dfrac{x_3^2}{4t}\right)\sqrt{x_t}/\sqrt{\pi} - x_3\,\mathrm{erfc}\left(\dfrac{x_3}{2\sqrt{x_t}}\right)\right], & w' = 0 \end{cases} \tag{A1.17}$$

$$\tilde{\tilde{\varphi}}^I = \frac{2\pi}{w}\tilde{\tilde{q}}[I(w, x_3, a_\omega, x_t) - I(w, x_3, a_\omega, 0)] - \tilde{\tilde{\varphi}}^{II} \tag{A1.18}$$

$$\tilde{\tilde{\varphi}}^{II} = \frac{\pi}{w}\tilde{\tilde{q}}\exp(-wx_3)[I(w,0,a_\omega,x_t) - I(w,0,a_\omega,O)] \qquad \text{(A1.19)}$$

$I_{,3}(w,x_3,a_\omega,x_t) =$

$$\begin{cases} w[\exp(a_\omega x_t)(f_+ - f_-) - g_- - g_+]/a_\omega, & w \neq 0, a_\omega \neq 0 \\ f_+\left(wx_t + \dfrac{x_3}{2}\right) - f_-\left(wx_t - \dfrac{x_3}{2}\right), & w \neq 0, a_\omega = 0 \end{cases} \qquad \text{(A1.20)}$$

$I_{,33} =$

$$\begin{cases} w[\,w\exp(a_\omega x_t)(f_+ + f_-) + w'(g_- - g_+)]/a_\omega\,, & w \neq 0, a_\omega \neq 0 \\ f_+\left(w^2 x_t + \dfrac{wx_3 + 1}{2}\right) + f_-\left(w^2 x_t - \dfrac{wx_3 - 1}{2}\right) - wh, & w \neq 0, a_\omega = 0 \end{cases} \qquad \text{(A1.21)}$$

Both $I_{,3}$ and $I_{,33}$ are zero when $w = 0$ and $a_\omega = 0$.

Steady-state case

For the steady-state case, formulas from the transient-continuous case are utilized, setting time to infinity. Eqs.(A1.1) to (A1.8) are then recovered using the followings:

$$\tilde{\tilde{T}} = \tilde{\tilde{q}}\exp(-x_3 w')/w' \qquad \text{(A1.22)}$$

$$\tilde{\tilde{\varphi}}^{I} = \begin{cases} \dfrac{4\pi\tilde{\tilde{q}}}{a_\omega w\,w'}[w\exp(-x_3 w') - w'\exp(-wx_3)] - \tilde{\tilde{\varphi}}^{II}, & a_\omega \neq 0 \\ \pi\tilde{\tilde{q}}\exp(-wx_3)(2wx_3 + 1)/w^3, & a_\omega = 0 \end{cases} \qquad \text{(A1.23)}$$

$$\tilde{\tilde{\varphi}}^{II} = \pi\tilde{\tilde{q}}\exp(-wx_3)\frac{2}{ww'(w + w')} \qquad \text{(A1.24)}$$

$$\tilde{\tilde{\varphi}}^{I}_{,3} = \begin{cases} 4\pi\tilde{\tilde{q}}\,[-\exp(-x_3 w') + \exp(-wx_3)]/a_\omega + w\tilde{\tilde{\varphi}}^{II}, & a_\omega \neq 0 \\ \pi\tilde{\tilde{q}}\exp(-wx_3)(1 - 2wx_3)/w^2, & a_\omega = 0 \end{cases} \qquad \text{(A1.25)}$$

$$\tilde{\tilde{\varphi}}^{I}_{,33} = \begin{cases} 4\pi\tilde{\tilde{q}}\ [w'\exp(-x_3 w') - w\exp(-wx_3)]/a_\omega - w^2\tilde{\tilde{\varphi}}^{II},\ a_\omega \neq 0 \\ \pi\tilde{\tilde{q}}\exp(-wx_3)(2wx_3 - 3)/w\ , \qquad a_\omega = 0 \end{cases} \tag{A1.26}$$

Transient-instantaneous case

For the transient-instantaneous case, the heat source is a function of time. Then, a third Fourier transform is conducted in the global formulas, see [Liu03]. Eqs.(A1.1) to (A1.8) are identical, after changing all the "$\approx$" by "$\approxeq$" and then recovered using the followings:

$$\tilde{\tilde{\tilde{T}}} = \tilde{\tilde{\tilde{q}}}\exp(-x_3\omega_0)/\omega_0 \tag{A1.27}$$

$$\begin{aligned} \tilde{\tilde{\tilde{\varphi}}}^{I} &= \int_0^\infty \tilde{\tilde{\tilde{q}}}\frac{2\pi}{w}\exp(-w|x_3 - \xi_3|)\frac{\exp(-\xi_3\omega_0)}{\omega_0}d\xi_3 \\ &= \frac{2\pi\tilde{\tilde{\tilde{q}}}}{w\omega_0}\left[\frac{\exp(-x_3\omega_0) - \exp(-x_3 w)}{w - \omega_0} - \frac{\exp(-x_3\omega_0)}{w + \omega_O}\right] \\ &= \frac{2\pi\tilde{\tilde{\tilde{q}}}}{w\omega_0(\omega_0^2 - w^2)}[(\omega_0 + w)\exp(-x_3 w) - 2w\exp(-x_3\omega_0)] \end{aligned} \tag{A1.28}$$

$$\tilde{\tilde{\tilde{\varphi}}}^{II} = 2\pi\exp(-wx_3)\tilde{\tilde{\tilde{q}}}\frac{1}{w\omega_0(w + \omega_0)} \tag{A1.29}$$

Where:

$$\omega_0 = \sqrt{i\omega_t + w^2 - a_\omega} \tag{A1.30}$$

And ω_t is the counterpart of time in the frequency domain.

Convolution product

Since all the formulas for the temperature, displacements and stresses are expressed as a convolution product between a Green function and the heat source q, the convolution theorem is utilized (see 2.2.4.2), but Frequency Response Functions (FRF) are used directly, instead of computing the Fast Fourier Transform of the influence coefficients. But important care need to be made while using FRF, see [Liu00b,Liu01b,Liu03].

In order to obtain the FRF, Eqs.(A1.1) to (A1.8) are computed by setting a unity Fourier transformed heat source. Once the FRF are discretized, the inverse Fast Fourier Transform is (carefully) conducted after multiplication with the Fast Fourier Transform of the real heat source, in order to obtain the desired value.

Appendix 2: Residual Stress Field in a Half-Space

Superposition method

A way to calculate the residual stress tensor is the superposition of three solutions Fig.A2.1. Solution 1 corresponds to the solution in an infinite space in presence of a cuboid of constant plastic strain. Solution 2 corresponds to the solution in an infinite space in the presence of a mirror cuboid of constant plastic strain, such as plastic deformations ε_{13}^{p} and ε_{23}^{p} are set opposites from those of the main element. The superposition of the two solutions leaves the median plane free of tangential stresses. Finally, Solution 3 corresponds to a half-space on which is applied the field of normal stress obtained on the median plane from Solutions 1 and 2 which is the double of each solution taken separately. At the end, the desired solution of a half-space in the presence of a cuboid of constant plastic strains with a free surface is obtained. Solutions 1 and 2 are expressed in a mark bound to the center of the cuboid of plastic strain by $\left(\sigma_{ij}^{r}\right)_{1\ or\ 2} = B_{ijkl} \cdot \varepsilon_{kl}^{p}$. Solution 3 is expressed in a mark whose origin is placed on the surface by $\left(\sigma_{ij}^{r}\right)_{3} = P_{ijkl} \cdot \varepsilon_{kl}^{p}$.

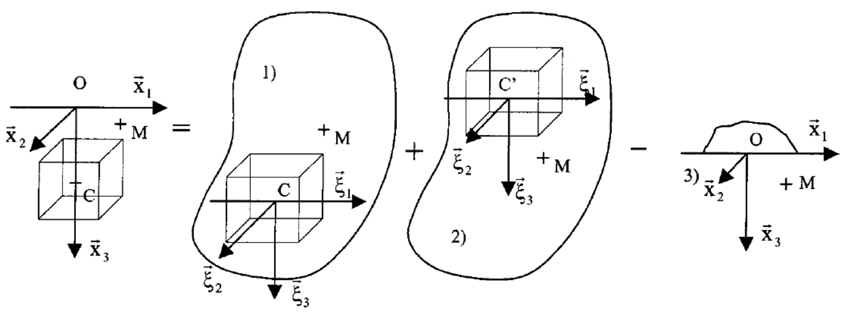

Fig.A2.1 Superposition of solutions

The final solution is expressed by

$$\sigma_{ij}^{r} = B_{ijkl}(x_1, x_2, x_3, -h) \cdot \varepsilon_{kl}^{p} + B_{ijkl}(x_1, x_2, x_3, +h) \cdot \varepsilon_{kl}^{p} + P_{ijkl}(x_1, x_2, x_3, h) \cdot \varepsilon_{kl}^{p} = A_{ijkl}(x_1, x_2, x_3, h) \cdot \varepsilon_{kl}^{p} \quad \text{(A2.1)}$$

The way to obtain tensors B and P is fully explained in [Jac02,Jac01]

Direct method

Chiu's superposition method is an indirect way to find the elastic field in a half-space with eigenstrains. In [Liu05], a direct way is adopted and the Mindlin and Cheng's halfspace results [Min50] or more general results reported by Yu and Sanday [Yu91] for joint half-spaces are utilized.
In [Liu05], a set of formulas for influence coefficients in terms of derivatives of four key integrals is presented and is used to express the elastic field caused by arbitrary distribution of eigenstrains in a half-space.
The described method uses the Discrete Correlation and Fast Fourier Transform (DCR-FFT) and the Discrete Convolution and Fast Fourier Transform (DC-FFT) and seems to be much more efficient than the one developed in the previous section.

Bibliography

[Ada00] G. G. Adams and M. Nosonovsky, "Contact Modeling - Forces," *Tribol. Int.*, vol. 33, pp. 431-442, 2000.

[All05] J. Allwood, "Survey and Performance Assessment of Solution Methods for Elastic Rough Contact Models," *ASME J. Tribol.*, vol. 127, pp. 10-23, 2005.

[Ant04] E. Antaluca, D. Nélias, and S. Cretu, "A Three- Dimensional Model for Elastic- Plastic Contact with Tangential Loading - Application to a Dented Surface," *Proc. of the 2004 STLE/ASME Tribology Conference*, no. TRIB2004- 64331, 2004.

[Bar72] J. R. Barber, "Distorsion of the Semi- Infinite Solid due to Transient Surface Heating," *Int. J. Mech. Sciences*, vol. 14, pp. 377-393, 1972.

[Bar00] J. R. Barber and M. Ciavarella, "Contact Mechanics," *Int. J. Solids Struct.*, vol. 37, pp. 29-43, 2000.

[Bhu01] B. Bhushan, "Modern Tribology Handbook I & II," 2001.

[Blo37] H. Blok, "Theoretical Study of Temperature Rise at Surfaces of Actual Contact Under Oiliness Lubricating Conditions," *Proc. General Discussion on Lubrication and Lubricants, London, 2, Institution of Mechanical Engineers*, pp. 222-235, 1937.

[Bou05] V. Boucly, D. Nélias, S. Liu, Q. J. Wang, and L. M. Keer, "Contact Analyses for Bodies with Frictional Heating and Plastic Behavior," *ASME J. Tribol.*, vol. 127, pp. 236-244, 2005.

[Bra90] A. Brandt and A. A. Lubrecht, "Multilevel Matrix Multiplication and Fast Solution of Integral Equation," *J. Comp. Phys.*, vol. 90, pp. 348-370, 1990.

[Cha87] W. R. Chang, I. Etsion, and D. B. Bogy, "An Elastic- Plastic Model for the Contact of Rough Surfaces," *ASME J. Tribol.*, vol. 109, pp. 257-263, 1987.

[Chi77] Y. P. Chiu, "On the Stress Field Due to Initial Strains in a Cuboid Surrounded by an Infinite Elastic Space," *ASME J. Appl. Mech.*, vol. 44, pp. 587-590, 1977.

[Chi78] Y. P. Chiu, "On the Stress Field and Surface deformation in a Half-Space with a Cuboidal Zone in Wich Initial Strains are Uniform," *ASME J. Appl. Mech.*, vol. 45, pp. 302-306, 1978.

[Coo65] J. W. Cooley and T. J.W., "An Algorithm for the Machine Calculation of Complex Fourier Series," *Mathematics of Computation*, vol. 19, pp. 297-301, 1965.

[ElG99] H. El Ghazal, "Etude des propriétés microstructurales et mécaniques des aciers 16NiCrMo13 cémenté et 32CrMoV13 nitruré- Application à la prévision de leur limite d'endurance en fatigue de roulement," Ph. D. Thesis, INSA Lyon, France, 1999.

[Fes57] H. Fessler and E. Ollerton, "Contact Stresses in Toroids Under Radial Loads," *Brit. J. Appl. Phys.*, vol. 8, pp. 387-393, 1957.

[Fot96] P. A. Fotiu and S. Nemat- Nasser, "A Universal integration Algorithm for Rate- Dependant Elastoplasticity," *Comput. Struct.*, vol. 59, pp. 1173-1184, 1996.

[Gal05] L. Gallego, D. Nélias, and C. Jacq, "A Comprehensive Elastic- Plastic Model to Predict Wear and to define the Optimum Geometry of Fretting Surfaces," *Proceedings of the 2005 World Tribology Congress III*, no. WTC2005- 63451, 2005.

[Gao00] J. Q. Gao, S. C. Lee, and X. L. Ai, "An FFT-Based Transient Flash Temperature Model for General Three-Dimensional Rough Surface Contacts," *ASME J. Tribol.*, vol. 122, p. 519–523, 2000.

[Gla80] G. M. L. Gladwell, "Contact Problems in the Classical Theory of Elasticity," 1980.

[Gos90] T. Goshima and L. M. Keer, "Thermoelastic Contact Between a Rolling Rigid Indenter and a Damaged Elastic Body," *ASME J. Tribol.*, vol. 112, pp. 382-391, 1990.

[Gre05] I. Green, "Poisson Ration Effects and Critical Values in Spherical and Cylindrical Hertzian Contacts," *Int. J. Appl. Mech. and Eng.*, vol. 10, pp. 451-462, 2005.

[Her82] H. Hertz, "On the Contact of Elastic Solids," *J. Reine Angew. Math.*, vol. 92, pp. 156-171, 1882.

[Hil93] D. A. Hills, D. Nowell, and A. Sackfield, "Mechanics of Elastic Contacts," 1993.

[Hua85] J. H. Huang and F. D. Ju, "Thermomechanical Cracking Due to Moving Frictional Loads," *Wear*, vol. 102, p. 81–104, 1985.

[Hu99] Y. Z. Hu, G. C. Barber, and D. Zhu, "Numerical Analysis for the Elastic Contact of Real Rough Surfaces," *Tribol. Trans.*, vol. 42, no. 3, pp. 443-452, 1999.

[Hu00] Y. Z. Hu and D. Zhu, "A Full Numerical Solution to the Mixed Lubrication in Point Contacts," *ASME J. Tribol.*, vol. 122, pp. 1-9, 2000.

[Jac05] R. Jackson, I. Chupoisin, and I. Green, "A Finite Element Study of the Residual Stress and Deformation in Hemispherical Contacts," *ASME J. Tribol.*, vol. 127, pp. 484-493, 2005.

[Jac01] C. Jacq, "Limite d'endurance et durée de vie en fatigue de roulement du 32CrMoV13 nitruré en présence d'indentations," PhD. Thesis, INSA, Lyon, 2001.

[Jac03] C. Jacq, G. Lormand, D. Nélias, D. Girodin, and A. Vincent, "On the Influence of Residual Stresses in Determining the Micro- Yield Stress Profile in a Nitrided Steel by Nano- Indentation," *Materials Science and Engineering A*, vol. 342, pp. 311-319, 2003.

[Jac02] C. Jacq, D. Nélias, G. Lormand, and D. Girodin, "Development of a Three- Dimensional Semi- Analytical Elastic- Plastic Contact Code," *ASME J. Tribol.*, vol. 124, pp. 653-667, 2002.

[Jae42] J. C. Jaeger, "Moving Sources of Heat and the Temperature at Sliding Contacts," *Proc. R. Soc. New South Wales*, vol. 76, p. 203–224, 1942.

[Jia99] X. Jiang, D. Y. HUA, H. S. Cheng, X. Ai, and S. C. Lee, "A Mixed Elastohydrodynamic Lubrication Model with Asperity Contact," *ASME J. Tribol.*, vol. 121, pp. 481-491, 1999.

[Joh85] K. L. Johnson, *Contact mechanics*, 1999th ed. London: Cambridge University Press, 1985.

[Ju88] F. D. Ju and J. C. Liu, "Effect of Peclet Number in Thermo-Mechanical Cracking Due to High-Speed Friction Load," *ASME J. Tribol.*, p. 217–221, 1988.

[Ju96] Y. Ju and T. N. Farris, "Spectral Analysis of Two-Dimensional Contact Problems," *ASME J. Tribol.*, vol. 118, pp. 320-328, 1996.

[Kad06] Y. Kadin, Y. Kligerman, and I. Etsion, "Multiple Loading- Unloading of an Elastic- Plastic Spherical Contact," *International Journal of Solids and Structures*, vol. 43, pp. 7119-7127, 2006.

[Kal90] J. J. Kalker, *Three dimensional Elastic Bodies in Rolling Contact*. Dordrecht: Kluwer Academic Publishers, 1990.

[Ken84] F. E. Kennedy, "Thermal and Thermomechanical Effects in Dry Sliding," *Wear*, vol. 100, pp. 453-476, 1984.

[Ken85] F. E. Kennedy, "Thermomechanical Effects in Sliding Systems," *Elsevier Sequoia S. A., New York*, 1985.

[Kog02] L. Kogut and I. Etsion, "Elastic- Plastic Contact Analysis of a Sphere and a Rigid Flat," *ASME J. Appl. Mech.*, vol. 69, pp. 657-662, 2002.

[Kog03] L. Kogut and I. Etsion, "A Semi- Analytical Solution for the Sliding Inception of a Spherical Contact," *ASME J. Tribol.*, vol. 125, pp. 499-506, 2003.

[Kul91] S. M. Kulkarni, C. A. Rubin, and G. T. Hahn, "Elasto-Plastic Coupled Temperature-Displacement Finite Element Analysis of Two-dimensional Rolling-Sliding Contact with a Translating Heat Source"," *ASME J. Tribol.*, p. 93–101, 1991.

[Lam98] P. Lamagnère, et al., "A Physically Based Model for Endurance Limit of Bearing Steels," *ASME J. Tribol.*, vol. 120, pp. 421-426, 1998.

[Lee92] S. C. Lee and H. S. Cheng, "On the Relation of Load to Average Gap in the Contact Between Surfaces With Longitudinal Roughness," *Tribol. Trans.*, vol. 35, no. 3, pp. 523-529, 1992.

[Lin73] F. F. Ling, *Surface Mechanics*. New York: Wiley, 1973.

[Liu00a] G. Liu and Q. Wang, "Thermoelastic Asperity Contacts, Frictional Shear, and Parameter Correlations," *ASME J. Tribol.*, vol. 122, p. 300–307, 2000.

[Liu99] G. Liu, Q. J. Wang, and C. Lin, "A Survey of Current Models for Simulating the Contact between Rough Surfaces," *Tribol. Trans.*, vol. 42, pp. 581-591, 1999.

[Liu01a] S. B. Liu, M. Rogers, Q. Wang, and L. Keer, "A Fast and Effective Method For Transient Thermoelastic Displacement Analyses," *ASME J. Tribol.*, vol. 123, pp. 479-485, 2001.

[Liu03] S. Liu and Q. Wang, "Transient Thermoelastic stress Fields in a Half-Space," *ASME J. Tribol.*, vol. 125, pp. 33-43, 2003.

[Liu05] S. Liu and Q. Wang, "Elastic Fields due to Eigenstrains in a Half-Space," *ASME J. Appl. Mech.*, vol. 72, pp. 871-878, 2005.

[Liu01b] S. Liu and Q. J. Wang, "A Three- Dimensional Thermomechanical Model of Contact between Non- Conforming Rough Surfaces," *ASME J. Tribol.*, vol. 123, pp. 17-26, 2001.

[Liu00b] S. Liu, Q. Wang, and G. Liu, "A versatile Method of Discrete Convolution and FFT (DC- FFT) for Contact Analyses," *Wear*, vol. 243, pp. 101-111, 2000.

[Lub91] A. A. Lubrecht and E. Loannides, "A Fast Solution of the Dry Contact Problem and the Associated Sub- Surface Stress Field, Using Multilevel Techniques," *ASME J. Tribol.*, vol. 113, pp. 128-133, 1991.

[Lu94] C. T. Lu and M. D. Bryant, "Evaluation of Subsurface Stresses in a

Thermal Mound with Application to Wear," *Wear*, vol. 177, pp. 15-24, 1994.

[Mer78] R. J. Mercier, S. Malkin, and J. C. Mollendorf, "Thermal Stresses from a Moving Band Source of Heat on the Surface of a Semi-infinite Solid," *ASME J. Eng. Ind.*, vol. 100, p. 43–48, 1978.

[Min50] R. D. Mindlin and D. H. Cheng, "Nuclei of Strain in the Semi-Infinite Solid," *J. Appl. Phys.*, vol. 21, p. 926–930, 1950.

[Moo07] J. Moody, "A Finite Element Analysis of Elastic-Plastic Sliding of Hemispherical Contacts," *M.S. Thesis, Georgia Institute of Technology, Atlanta, GA.*, 2007.

[Mow67] V. C. Mow and H. S. Cheng, "Thermal Stresses in an Elastic Half-Space Associated with an Arbitrary Distributed Moving Heat Source," *J. Appl. Math. Phys. (ZAMP)*, vol. 18, pp. 500-507, 1967.

[Nel97] D. Nélias, "Etude expérimentale et théorique du micro- grippage dans les contacts élastohydrodynamiques," *revue Générale de Thermique*, vol. 36 (1), pp. 26-39, 1997.

[Nel07] D. Nélias, E. Antaluca, V. Boucly, and S. Cretu, "A 3D Semi-Analytical Model for Elastic- Plastic Sliding Contacts," *ASME J. Tribol.*, 2007.

[Nel06] D. Nélias, V. Boucly, and M. Brunet, "Elastic- Plastic contact between Rough Surfaces: Proposal for a Wear or Running- in Model," *ASME J. Tribol.*, vol. 128, pp. 236-244, 2006.

[Nel99] D. Nélias, et al., "Role of Inclusions, Surface Roughness and Operating Conditions on Rrolling Contact Fatigue," *ASME J. Tribol.*, vol. 121, pp. 240-251, 1999.

[Nel05] D. Nélias, C. Jacq, G. Lormand, G. Dudragne, and A. Vincent, "A New Methodology to Evaluate the Rolling Contact Fatigue Performance of Bearing Steels with Surface Dents - Application to 32CrMoV13 (Nitrided) and M50 Steels," *ASME J. Tribol.*, vol. 127, pp. 611-622, 2005.

[Nit00] I. Nitta and K. Kato, "Theory of Contact and Friction," *Japanese J. Tribol.*, vol. 45, pp. 507-512, 2000.

[Nog97] T. Nogi and T. Kato, "Influence of a Hard Surface Layer on the Limit of Elastic Contact - Part I: Analysis using e Real Surface Model," *ASME J. Tribol.*, vol. 119, pp. 493-500, 1997.

[Oil05] A. Oila, B. A. Shaw, C. J. Aylotts, and S. J. Bull, "Matensite decay in Micropitted Gears," *J. Eng. Tribol. (Part J)*, vol. 219, pp. 77-83, 2005.

[Pol66] N. H. Polakowski and E. J. Ripling, *Strength and Structure of Engineering Materials*, E. Cliffs, Ed. New Jersey: Prentice- Hall Inc., 1966.

[Pol00a] I. A. Polonsky and L. M. Keer, "A Fast and Accurate Method for Numerical Analysis of Elastic Layered Contacts," *ASME J. Tribol.*, vol. 122, pp. 30-35, 2000.

[Pol00b] I. A. Polonsky and L. M. Keer, "Fast Methods for Solving Rough Contact Problems: a Comparative Study," *ASME J. Tribol.*, vol. 122, pp. 36-41, 2000.

[Pol99] I. A. Polonsky and L. M. Keer, "A New Numerical Method for Solving rough Contact Problems Based on the Multi- Level Multi- Summation and Conjugate Gradient Techniques," *Wear*, vol. 231, pp. 206-219, 1999.

[Pre92] W. H. Press, S. A. Teukolsky, V. W. T., and B. P. Flannery, *Numerical Recipes in Fortran 77 - The Art of Scientific Computing*. Cambridge University Press, 1992, vol. 1.

[Qiu98] L. Qiu and H. S. Cheng, "Temperature Rise Simulation of Three-Dimensional Rough Surfaces in Mixed Lubricated Contact," *ASME J. Tribol.*, vol. 120, pp. 310-318, 1998.

[Sac83a] A. Sackfield and D. A. Hills, "Some Useful Results in the Classical Hertz Contact Problem," *J. Strain Anal.*, vol. 18, pp. 101-108, 1983.

[Sac83b] A. Sackfield and D. A. Hills, "A Note on the Hertz Contact Problem: Correlation of Standard Formulae," *J. Strain Anal.*, vol. 18, pp. 195-201, 1983.

[Seo79] K. Seo and T. Mura, "The Elastic Field in a Half Space Due to Ellipsoidal Inclusions with Uniform Dilatational Eigenstrains," *ASME J. Appl. Mech*, vol. 46, pp. 578-572, 1979.

[Shi00] F. Shi and R. F. Salant, "A Mixed Soft Elastohydrodynamic Lubrication Model with Interasperity Cavitation and Surface Shear Deformation," *ASME J. Tribol.*, vol. 122, pp. 308-316, 2000.

[Sin69] R. C. Singleton, "An Algorithm for Computing the Mixed Radix Fast Fourier Transform," *IEEE Transactions on Audio and Electroacoustics*, vol. AU17, no. 2, pp. 93-103, 1969.

[Smi53] J. O. Smith and C. K. Liu, "Stresses due to tangential and normal loads on an elastic solid," *ASME J. Appl. Mech.*, vol. 20, pp. 157-166, 1953.

[Ste00] L. S. Stephens, L. Yan, and E. I. Meletis, "Finite element analysis of the initial yielding behaviour of a hard coating/substrate system with functionally graded interface under indentation and friction," *ASME J. Tribol.*, vol. 122, pp. 381-387, 2000.

[Tal78] T. E. Tallian, Y. P. Chiu, and E. V. Amerongen, "Prediction of Traction and Microgeometry Effects on rolling Contact Fatigue Life," *ASME J. Lubr. Tech.*, vol. 100, pp. 156-166, 1978.

[Tho30] H. R. Thomas and V. A. Hoersch, "Stresses due to the pressure of one elastic solid on another," *Univ. of Illinois Engng. Exptal. Station Bulletin*, vol. 212, 1930.

[Tia94] X. Tian and F. E. Kennedy, "Maximum and Average Flash Temperature in Sliding Contacts," *ASME J. Tribol.*, vol. 116, pp. 167-173, 1994.

[Tin89] B. Y. Ting and W. O. Winner, "Frictional-Induced Thermal Influences in Elastic Contact Between Spherical Asperities," *ASME J. Tribol.*, vol. 111, pp. 315-322, 1989.

[Tse82] M. L. Tseng and R. A. Burton, "Thermal Stress in a Two-dimensional (Plane Stress) Half-space for a Moving Heat Input," *Wear*, vol. 79, p. 1–9, 1982.

[Ver85] F. Vergne, "Calcul des Déplacements et des Contraintes Dans un Demi-Espace Elastique Chargé en Surface par des Actions Distribuées Normales ou Tangentielles Quelconques," Master's Thesis, INSA, Lyon, 1985.

[Vij06] R. Vijaywargiya and I. Green, "A Finite Element Study of the Deformation, Forces, Stress Formation, and Energy Losses in Sliding Cylindrical Contacts," *Int. J. Non Linear Mech.*, vol. 42, pp. 914-927, 2006.

[Vin06] A. Vincent, D. Nélias, C. Jacq, Y. Robin, and G. Dudragne, "Comparison of Fatigue Performances of 32CrMoV13 and M50 Steels in Presence of Surface Indents," *Journal of ASTM Iternational*, vol. 3 (2), pp. 1-9, 2006.

[Wan05] F. Wang and L. M. Keer, "Numerical Simulation for Three Dimensional Elastic- Plastic Contact with Hardening Behavior," *ASME J. Tribol.*, vol. 127, pp. 494-502, 2005.

[Wan99] Q. Wang and G. Liu, "A Thermoelastic Asperity Contact Model Considering Steady-State Heat Transfer," *STLE Tribol. Trans.*, vol. 42, no. 4, pp. 763-770, 1999.

[Yu91] H. Y. Yu and S. C. Sanday, "Elastic Fields in Joined Half-Spaces Due to Nuclei of Strain," *Proc. R. Soc. London, Ser. A*, vol. 434 (1892), p. 503–519, 1991.

FOLIO ADMINISTRATIF

THESE SOUTENUE DEVANT L'INSTITUT NATIONAL DES SCIENCES APPLIQUEES DE LYON

NOM : BOUCLY DATE de SOUTENANCE : 23 septembre 2008
(avec précision du nom de jeune fille, le cas échéant)

Prénoms : Vincent

TITRE : Semi-Analytical Modeling of the Transient Thermal-Elastic-Plastic Contact and its Application to Asperity Collision, Wear and Running-in of Surfaces

NATURE : Doctorat Numéro d'ordre : 2008-ISAL-0065

Ecole doctorale : MEGA de Lyon

Spécialité : Mécanique

RESUME :

Le champ de contraintes au sein des composants de machines est un indicateur important de défaillance due au contact. Comme les contraintes thermiques provoquées par l'échauffement dû au frottement à l'interface ainsi que la plasticité sont significatifs pour les applications réelles, il est critique de prédire le champ de contraintes total. Dans ce travail, une analyse transitoire et tridimensionnelle est réalisée, en prenant en considération le comportement plastique au sein des corps en contact, ainsi que l'échauffement à l'interface. Un algorithme rapide et robuste est proposé pour la résolution du contact vertical, roulant et glissant. Cet algorithme est une alternative à la méthode des Eléments Finis car il donne des résultats précis et robustes en des temps de calcul plus courts, de plusieurs ordres de grandeur. Pour atteindre ce but, des solutions analytiques sont utilisées, appelées coefficients d'influence, et sont utilisées pour le calcul des déplacements, du champ de température, et des tenseurs des déformations et des contraintes. Dans cette formulation, des schémas numériques particuliers sont adoptés afin d'accélérer les temps de calculs. Le problème de contact, qui est une des procédures les plus couteuses, est obtenu en utilisant une méthode basée sur le principe de variation et accéléré au moyen de l'algorithme de convolution discrète et transformée de Fourier rapide ainsi que l'algorithme de gradient conjugué. Aussi, le return-mapping avec prédicteur élastique et correcteur plastique et un critère de von Mises est utilisé pour la boucle plastique. Le modèle est applicable à l'étude du contact roulant et glissant, tant que l'hypothèse des petites perturbations est respectée, et le frottement est reproduit par une loi de Coulomb, comme à l'habitude pour les contacts glissants. La première partie de ce travail décrit l'algorithme utilisé pour formuler le contact vertical, qui peut être traité en imposant soit une charge, soit un déplacement. La manière de traiter le roulement et le glissement de deux corps en contact consiste à résoudre le contact thermo-élasto-plastique à chaque pas de temps en mettant à jour les géométries ainsi que l'écrouissage le long de la direction de roulement. Des simulations sont présentées pour différents cas académiques allant du cas élastique au cas cas thermo-élasto-plastique. Des données expérimentales valident également la théorie et la procédure numérique. Aussi une analyse numérique du contact roulant entre un corps elliptique élastique et un massif élasto-plastique est présentée ainsi que l'influence de différentes lois d'écrouissages. L'application à la collision entre deux aspérités sphériques en glissement simple est développée. La manière de projeter les forces dans le repère global est soulignée, considérant la projection macroscopique due à l'angle entre le plan de contact et la direction de glissement, et la projection microscopique due au bourrelet induit par la déformation permanente des corps en déplacement relatif. Un coefficient de frottement apparent est introduit et les résultats sont présentés en termes d'efforts, de déplacements, et d'énergie dissipée dans le contact. Finalement un modèle pour la prédiction de l'usure et du rodage basé sur l'enlèvement de matière durant un chargement cyclique est proposé. Les résultats sont présentés dans un premier temps pour une surface lisse puis dans un second temps pour une surface rugueuse

MOTS-CLES : Contact, Thermo-Elasto-Plasticité, Usure, Rodage, Aspérités

Laboratoire (s) de recherche : Laboratoire de Mécanique des Contacts et des Solides (LaMCoS), UMR5514 CNRS INSA Lyon

Directeurs de thèse: Daniel Nélias, Michel Brunet

Président de jury :

Composition du jury : Habibou Maitournam, Christian Gauthier, Timothy C. Ovaert, Alain Cimetière, Emmanuelle Rouhaud, Juan-Antonio Ruiz Sabariego, Michel Brunet, Daniel Nélias